Master's thesis

NTNU
Norwegian University of Science and Technology
Faculty of Engineering
Department of Marine Technology

Maiten Kase Corona

Tensegrity-Based Semi-Submersible Support Structure for a Floating Offshore Wind Turbine

Master's thesis in Marine Technology
Supervisor: Svein Sævik
Co-supervisor: Erin Bachynski
June 2022

NTNU
Kunnskap for en bedre verden

Maiten Kase Corona

Tensegrity-Based Semi-Submersible Support Structure for a Floating Offshore Wind Turbine

Master's thesis in Marine Technology
Supervisor: Svein Sævik
Co-supervisor: Erin Bachynski
June 2022

Norwegian University of Science and Technology
Faculty of Engineering
Department of Marine Technology

NTNU
Norwegian University of
Science and Technology

NTNU
Norwegian University of
Science and Technology

Department of Marine Technology

Master's Thesis

Tensegrity-Based Semi-Submersible Support Structure for a Floating Offshore Wind Turbine

Author:
Corona, Maiten Kase

Supervisor: Sævik, Svein
Co-Supervisor: Bachynski, Erin

June, 2022

Summary

For increasing water depths, floating wind turbines (FWTs) may be the most cost effective solution in order to exploit the potential of offshore wind energy. The need for more sustainable energy sources is increasing, and offshore wind show several advantages over onshore. According to several studies, the potential for harvesting offshore wind energy at deep water sites where floating structures are the preferred solution, is huge. However, for FWTs to compete with other energy sources, it must be cost-competitive, which is still not the case. Since electricity is a commodity, being competitive mostly means being cost competitive for the user, which for FWTs is a challenge considering the many well-established available electrical power sources. Developing new foundation concepts to reduce the material use is hence a step in the right direction of minimizing the cost, as traditional designs of FWTs result in a steel or concrete mass more than half of the total structural mass due to conservative substructure design (Gaertner et al. 2020; Silva de Souza et al. 2021; Xue 2016).

The aim of this thesis is to investigate an alternative design approach to a semi-submersible foundation concept. The goal is then to obtain a mass reduction of minimum 25% compared to the design used as reference; the semi-submersible Wind Floater concept developed by Dr.techn. Olav Olsen. It is designed to support the Technical University of Denmark (DTU) 10 MW horizontal axis wind turbine (WT) (Bak et al. 2013) in 130 m water depth. In the modified design, the centered column carrying the WT is located at the geometrical center, and the buoyancy elements consist of six outer columns arranged radially outward from the tower. They are connected to each other and to the shaft through a tensegrity system, which is a system of pretensioned wires and compressive beams. With this new design, the goal is to arrive at an economically competitive concept.

A model was developed in the software SIMO-RIFLEX-AeroDyn in order to investigate the behaviour of the modified semi-submersible foundation, as well as verify the spreadsheet-based calculations conducted. Also, a physical 3D printed model of the concept was made at the laboratory of the Department of Marine Technology. After the spreadsheet-based design process, it was found that a reduction of 65.7% in mass was possible to achieve compared to the foundation concept developed by Dr.techn. Olav Olsen, which potentially will reduce the cost of the structure significantly, as well as its environmental footprint.

Four different environmental load cases were applied on the tensegrity-based semi-

submersible WT concept in SIMO-RIFLEX-AeroDyn in order to assess the ultimate limit state (ULS) capacity of the concept. TurbSim turbulent wind was applied in order to simulate the wind, which was run for below-rated, rated, above-rated and an extreme condition applying a wind with 50 years recurrence period in parked condition. Also a wave with 50 years recurrence period was combined with the latter, and the load case revealed to be the one causing the largest responses in the tensegrity system. Different sensitivity analyses were performed with this base load case in order to look at the behaviour of the tensegrity system to different modifications, and the axial forces and relative displacements of the foundation were studied, using Matlab as the post-processing tool. It was found, based on the analyses conducted in this work, that a tensegrity system is feasible to use on a WT foundation, even though the accidental limit state (ALS) and fatigue limit state (FLS) of the concept has not been assessed in this work, neither has different failure modes such as fretting fatigue or slamming. However, the purpose of this work was to investigate if pretensioned guy wires and compressive beams, forming a tensegrity system, could be used in the foundation of a FWT. The sensitivity analyses showed that the best solution in order to reduce the forces on the pretensioned guy wires in the tensegrity system, was to increase their cross-sectional areas.

Sammendrag

I dyptliggende havområder er muligens flytende vindturbiner den mest kostnadseffektive løsningen for å utnytte potensialet til offshore vindenergi. Behovet for mer bærekraftige energikilder øker, og offshore vind viser flere fordeler over landbasert. Ifølge flere studier, så er potensialet for å utnytte offshore vindenergi der vanndybden er stor og hvor flytende strukturer er den foretrukne løsningen, enorm. Men for at energi produsert av flytende vindturbiner skal kunne konkurrere med andre energikilder, må de være kostnadsmessig konkurransedyktige, noe som fortsatt ikke er tilfellet. Siden elektrisitet er en handelsvare, må de være konkurransedyktige for brukeren, som er vanskelig å oppnå tatt i betraktning de mange veletablerte elektriske energikildene som finnes på markedet. Å utvikle nye fundamenter for å redusere materialbruken er derfor et skritt i riktig retning for å redusere kostnadene, da stål- eller betongmassen til tradisjonelle design av flytende vindturbiner utgjør mer enn halvparten av den totale strukturmassen grunnet konservativt fundamentdesign (Gaertner et al. 2020; Silva de Souza et al. 2021; Xue 2016).

Målet for denne masteroppgaven er å undersøke et alternativt designkonsept for et flytende halvt nedsenkbart fundament, og dermed oppnå en massereduksjon på minst 25% sammenlignet med designet som har blitt brukt som referanse; det halvt nedsenkbare vindturbinkonseptet utviklet av Dr.techn. Olav Olsen. Det er designet for DTU sin 10 MW vindturbin med horisontal akse (Bak et al. 2013) i 130 m vanndybde. I det modifiserte designet er den sentrale kolonnen som bærer vindturbinen plassert i det geometriske senteret, med oppdriftselementer bestående av seks ytre kolonner plassert radialt ut fra tårnet. De er forbundet til hverandre og til den sentrale kolonnen gjennom et ”tensegrity” system, som er et system av forspente vaiere og kompressive bjelker. Målet med dette nye fundamentdesignet er å oppnå et økonomisk konkurransedyktig konsept.

En modell av strukturen har blitt utviklet i programvaren SIMO-RIFLEX-AeroDyn for å kunne analysere oppførselen til det modifiserte halvt nedsenkbare fundamentet, i tillegg til å kunne verifisere utregningene utført i et regneark. I tillegg har en fysisk 3D modell av konseptet blitt printet ved laboratoriet til Institutt for Marin Teknikk. Utregningene utført i regnearket viste at en reduksjon på 65.7% i masse var mulig å oppnå sammenlignet med fundamentet utviklet av Dr.techn. Olav Olsen. Dette kan potensielt redusere kostnadene og miljøavtrykket til strukturen betraktelig.

Fire forskjellige miljølaster ble påført det ”tensegrity” baserte halvt nedsenkbare vindturbinkonseptet i SIMO-RIFLEX-AeroDyn for å undersøke bruddgrensetilstanden

(ULS) til fundamentet. TurbSim turbulent vind ble brukt for å simulere vinden, med analyser utført for en underratet vindkondisjon, en ratet vindkondisjon, en overratet vindkondisjon, og en ekstrem vindkondisjon med 50 års returperiode og parkert turbin. En bølge med 50 års returperiode ble kombinert med den sistnevnte, og det viste seg at det var denne miljøkondisjonen som forårsaket de største responsene i "tensegrity" systemet. Forskjellige sensitivitetsanalyser ble utført med denne lastkondisjonen for å kunne se på oppførselen til "tensegrity" systemet mot ulike modifikasjoner, og de aksielle kreftene og relative forskyvningene av fundamentet ble undersøkt, med bruk av Matlab som post-prosesseringsverktøy. Det ble konkludert med, basert på analysene gjennomført i dette arbeidet, at et "tensegrity" system er mulig å bruke i fundamentet på en vindturbin, selv om hverken ulykkesgrensetilstanden (ALS) eller utmattingsgrensetilstanden (FLS) har blitt undersøkt i dette arbeidet. Det har heller ikke uønskede hendelser som fretting eller slamming blitt. Men, målet med dette arbeidet var å undersøke om forspente vaiere og kompressive bjelker, formet til et "tensegrity" system, var realistisk å bruke i et flytende vindturbinfundament. Sensitivitetsanalysene viste at den beste løsningen for å redusere kreftene på de forspente vaierene i "tensegrity" systemet, var å øke tverrsnittsarealet deres.

Preface

This master's thesis is written during the spring semester 2022. It is submitted as the final thesis for the five-years Master of Science (M.Sc.) degree at the Norwegian University of Science and Technology (NTNU). The work has been performed at the Department of Marine Technology (IMT) at NTNU under the supervision of Professor Svein Sævik (NTNU) and co-supervisor Erin Bachynski (NTNU). The outline for the project was formed in collaboration with them. The report counts for 100% of the final grade in *TMR4930 - Marine Technology, Master's Thesis*, and is written in its entirety by Maiten Kase Corona.

The motivation of the work is to optimize the semi-submersible substructure of the OO-Star Wind Floater, a concept developed by Dr.techn. Olav Olsen, in order to reduce the material use and thereby the cost and environmental footprint. The work is based on the project thesis written during the fall semester 2021. Parts of this master's thesis are taken from this project, in particular Sections 2 and 3. The title of the master's thesis was changed in accordance with the supervisors during the spring semester.

From the two module courses the fall semester of 2021, *TMR01 - Dynamic analysis of Marine Structures* and *TMR03 - Integrated Dynamic Analysis of Wind Turbines*, valuable knowledge has been gained about general dynamic analysis of marine structures and analysis of wind turbines, which has been a great inspiration for the design of this project. The theoretical knowledge gained has been valuable for the understanding and application of the performed analyses.

I would like to thank my two supervisors, Professor Svein Sævik and Professor Erin Bachynski at NTNU, for providing me with good references and guiding me throughout the semester. I am grateful for the knowledge they have shared with me, both about floating wind turbines and dynamic analysis of marine structures. Also, the discussions and feedback received have been to great help. From mid-February 2022, Erin Bachynski went into maternity leave, leaving Svein Sævik as the supervisor.

Maiten Kase Corona
Trondheim, June 7th, 2022

NTNU Trondheim
Norwegian University of Science and Technology *Faculty of Engineering*
Department of Marine Technology

MASTER THESIS WORK SPRING 2022
for

Stud. Tech. Maiten Corona

Cost-efficient support structure for a Floating Offshore Wind Turbine (FOWT)
Kostnadseffektiv bærekonstruksjon for flytende havvindturbiner

Traditional designs of FOWTs result in a steel/concrete mass usually around 65-90% of the total structural mass. This is a result of conservative substructure design principles, originating from the oil and gas industry, where both profit margins and failure consequences differ significantly from the offshore wind industry. To enhance the FOWT technology, a significant mass reduction is thus needed. Reducing the mass reduces the use of resources and improves the climate footprint as floating substructures are built of steel and concrete, having high CO2 emissions in production. The primary idea here is to investigate an alternative design approach where the support structure buoyancy elements are connected to the shaft by a system of pretensioned wires and compressive beams that respond to the hydrodynamic and wind forces in a more compliant way than traditional stiff designs, aiming at obtaining a 25% mass reduction. The master thesis work is to be carried out as a continuation of the project performed during Fall 2021 and is to be carried out as follows:

1. On an if needed bases perform supplementary literature review into wave and wind statistical description (spectra), wind power models, the concept of tensegrity structures, methods for static and dynamic analysis of floating wind turbine structures, mechanical properties of guy wires with respect to damping, fatigue and ultimate strength, relevant guidelines and standards.
2. Continue the work on establishing the tensegrity-based wind turbine concept with focus on identifying primary structural parameters, i.e. member stiffness properties length and geometry (on the basis of the OO Star concept) to ensure robustness with respect to ULS.
3. Establish concept based on static analyses and evaluating the needed member capacities.
4. Establish a SIMA model of the chosen concept.
5. Perform eigenvalue analysis and compare with the base case concept eigenvalues and modes.
6. Perform analyses to document the ULS and FLS performance of the structure.
7. Conclusions and recommendations for further work

The work scope may prove to be larger than initially anticipated. Subject to approval from the supervisors, topics may be deleted from the list above or reduced in extent.

In the master thesis report, the candidate shall present her personal contribution to the resolution of problems within the scope of the master thesis work

Theories and conclusions should be based on mathematical derivations and/or logic reasoning identifying the various steps in the deduction.

The candidate should utilise the existing possibilities for obtaining relevant literature.

Master thesis report format
The master thesis report should be organised in a rational manner to give a clear exposition of results, assessments, and conclusions. The text should be brief and to the point, with a clear language. Telegraphic language should be avoided.

The report shall contain the following elements: A text defining the scope, preface, list of contents, summary, main body of thesis, conclusions with recommendations for further work, list of symbols and acronyms, references and (optional) appendices. All figures, tables and equations shall be numerated.

The supervisors may require that the candidate, in an early stage of the work, presents a written plan for the completion of the work.

The original contribution of the candidate and material taken from other sources shall be clearly defined. Work from other sources shall be properly referenced using an acknowledged referencing system.

The report shall be submitted in electronic format (.pdf):
- Signed by the candidate
- The text defining the scope shall be included (this document)
- Drawings and/or computer models that are not suited to be part of the report in terms of appendices shall be provided on separate (.zip) files.

Ownership
NTNU has according to the present rules the ownership of the master thesis reports. Any use of the report has to be approved by NTNU (or external partner when this applies). The department has the right to use the report as if the work was carried out by a NTNU employee, if nothing else has been agreed in advance.

Thesis supervisors:

Prof. Svein Sævik, NTNU, svein.savik@ntnu.no
Prof. Erin Bachynski-Polić, erin.bachynski@ntnu.no

Deadline: As decided on the web

NTNU
Norwegian University of Science and Technology

Faculty of Engineering
Department of Marine Technology

Trondheim, January, 2022

Svein Sævik

Erin Bachynski-Polić

Candidate – date and signature:

7/6 - 2022

Maiken K. Corona

Table of Contents

List of Figures

List of Tables

Nomenclature

Abbreviations

ALS accidental limit state.

BEM Blade Element Momentum.

CFD computational fluid dynamics.

COG center of gravity.

DLC design load case.

DOF degree of freedom.

DTU Technical University of Denmark.

ESS extreme sea state.

FE finite element.

FLS fatigue limit state.

FOWT floating offshore wind turbine.

FWT floating wind turbine.

GDW Generalized Dynamic Wake.

JONSWAP Joint North Sea Wave Project.

MSL mean sea level.

NTM normal turbulence model.

NTNU Norwegian University of Science and Technology.

OWT offshore wind turbine.

PM Pierson-Moskowitz.

RNA rotor nacelle assembly.

SS sea state.

SSS severe sea state.

ULS ultimate limit state.

WT wind turbine.

Parametric Semi-Submersible Design Variables

D_b	Diameter of beams
D_{oc}	Diameter of outer columns
h_{oc}	Height of outer columns
L_b	Length of beams
r_{tc}	Distance between the centered and outer columns
T_{oc}	Draft of outer columns
T_{cc}	Draft of centered column

Mathematical Model and Response Variables

$\mathbf{A}$	Added mass matrix (6x6)
A	Area
A_{WP}	Waterplane area
$A_{jk}(\omega)$	Frequency-dependent added mass matrix entry
A_j	Wave component amplitude
$\mathbf{B}$	Damping matrix (6x6)
$B_{jk}(\omega)$	Frequency-dependent damping matrix entry
$\boldsymbol{B_{Rayleigh}}$	Structural damping matrix
$\mathbf{C}$	Hydrostatic stiffness matrix (6x6)
C_a	Added mass coefficient
C_D	Drag coefficient
C_{jk}	Stiffness matrix entry
D	Diameter
$\mathbf{F}$	Force matrix (6x1)
$F_{T,rated}$	Wind turbine rated thrust force
G	Shear modulus
g	Acceleration due to gravity
$H(\omega)$	Complex frequency-response function
H_{MSL}	Hub height above MSL
H_s	Significant wave height
I	Turbulence intensity
I_{WP}	Waterplane area moment of inertia
k	Wavenumber
$\mathbf{M}$	Mass matrix (6x6)
M_{jk}	Mass matrix entry
$\vec{R}^{ext}$	External loads
$\vec{R}^{int}$	Internal reaction forces
$S(\omega)$	Wave spectrum
t	Time

T_p	Peak wave period
$\bar{U}$	Mean wind speed
U	Wind speed
$\bar{U}_{ref}$	Mean wind speed at reference height z_{ref}
z_{ref}	Reference height
β	Frequency ratio
β_{nb}	Newmark-Beta integration parameter
γ	Newmark-Beta integration parameter
$\boldsymbol{\eta}$, $\dot{\boldsymbol{\eta}}$, $\ddot{\boldsymbol{\eta}}$	Body displacement, velocity and acceleration matrix (6x1)
η_k, $\dot{\eta}_k$, $\ddot{\eta}_k$	Body displacement, velocity and acceleration, k = 1,..., 6
λ	Damping ratio
ρ	Sea water density
ρ_s	Steel density
ρ_{cc}	Centered column steel density
σ_a	Allowable stress
σ_u	Wind speed standard deviation
ϕ	Eigenvector
ω	Wave frequency
ω_0	Natural frequency
∇	Volume displacement

1 Introduction

Energy consumption in the world has increased the last decades due to the rate of growth in world gross domestic product which is the main driver of energy demand. With an expected electricity demand increase of 2.6% per year during 2004 - 2030, global energy-related carbon-dioxide emissions are expected to have an increase of 1.7% per year during the same period (International Energy Agency 2006). The world's energy supply is increasingly being provided by renewable energy sources, among which wind energy is taking an increasingly important role. With no roads limiting floating offshore wind turbine (FOWT) transportation, one can use larger turbines providing higher energy amounts compared to onshore wind turbines, as well as liberate large onland areas. In addition, offshore wind blows more strongly as well as more consistently compared to onshore.

On the other side, FOWTs are less accessible compared to land-based wind turbines, making maintenance and installation more complicated, as well as being exposed to additional external loads such as hydrodynamic forces from waves and sea currents. Due to this, their platform geometry is important, which will be analysed in this thesis. Several FWT substructure concepts are today conservatively designed, resulting from practices in the oil and gas industry, giving an approximate 60% - 90% steel or concrete mass of the total structure (Gaertner et al. 2020; Silva de Souza et al. 2021; Xue 2016). However, the differences in both profit and failure consequences in the oil industry compared to the WT industry are great, making it possible to reduce the material use in the substructure and thereby the environmental footprint and costs. For the time being, FOWTs are dependent on subsidies, which is an important reason to look at cost reductions in their design. The OO-Star semi-submersible floating substructure is the one modified in this work in order to achieve this, designed by Dr.techn. Olav Olsen AS.

The goal of this master's thesis is to develop a WT foundation concept based on a tensegrity system. A great advantage with such a system is that the elements are only axially loaded; no bending and shear forces are present. Due to this, the concept can apply less material, lowering the weight of the construction. However, only having to withstand forces in axial direction can be challenging with regards to the large bending moment caused by the WT. Also fatigue due to corrosion on the cable elements below the mean sea level (MSL) can be a large challenge for such a concept, as well as building and maintaining the foundation, as it is a structure of many components. However, the purpose of this work is to investigate under which conditions such a dynamic system can function, and if a tensegrity system is

realistic at all, leaving these challenges outside the scope of this work.

1.1 Background

The concept of FWT systems was introduced for the first time in the 1970s by professor Heronemus at the University of Massachusetts at Amherst (University of Massachusetts Amherst 2022). Close to 40 years later, FWTs are a reality.

In 2009, Statoil installed the first grid-connected FWT in Norway called Hywind, with a 2.3 MW Siemens WT (Equinor 2022a). Two years later, another concept called Wind-Float developed by Principle Power was installed off the Portuguese coast, with a 2 MW Vestas WT (4C Offshore 2022). In 2017, Equinor launched the world's first floating wind park in full scale called Hywind Scotland, which has a total power of 30 MW (Equinor 2022b). Many other exciting concepts are being developed and tested around the world today. An overview of these can be found in reports by the Renewables Consulting Group (Renewables Consulting Group 2021).

1.2 Concept Classification

Since offshore wind turbines (OWTs) have a large top mass and a large thrust force acting at a great height above the sea surface, the stability of a floating platform is challenging. Solutions to this fall into three different strategies based on the way they stabilize in pitch/roll (Det Norske Veritas 2013; Dominique Roddier 2011):

- Gravity-based, having the center of gravity under the center of buoyancy. Concept: spar platform.
- Waterplane area based, having a wide free surface area to achieve a large moment of inertia. Concepts: barge and semi-submersible platform.
- External constrain based, having large external mooring forces to keep the platform stable. Concept: tension-legged platform.

The different concepts are introduced in the following (Det Norske Veritas 2013; Dominique Roddier 2011):

Spar is a gravity stabilized structure which requires a large draft. This concept usually have good stability and small heave motions. However, the necessary hull draft hinder the use of spar platforms in less than 100 m water depth.

Semi-submersible is a waterplane area moment of inertia stabilized structure. The main concern with this concept is that they may experience large heave motions in waves.

Tension-legged platforms uses tendons to provide stability, which also limits the motion of the platform. The challenge with such a concept lies in the natural frequency similarities and the potential of structural coupling between the wind turbine and the tendons. In addition, significant sea bed preparation before installation is required.

1.3 Potential

Offshore wind had in 2018 a total installed capacity of 23 GW, providing 0.3% of global electricity supply. In October 2019 however, the International Energy Agency (IEA) published a report stating that offshore wind has a potential of generating at least 420 000 TWh per year, which is more than 18 times the global electricity demand (IEA 2019). Of this, as much as 80% come from sites located in deep waters above 60 meters where FWTs are considered the best solution (Cruz and Atcheson 2016). Also, the IEA predicts that with the current policies, the offshore wind business will expand with 13% per year and reach a $1 trillion business within 2040.

According to a study performed by 16 leading companies in the offshore wind sector (Athanasia and Genachte 2013), floating designs are necessary in order to unlock the offshore market potential in deeper water regions such as the Atlantic, the Mediterranean and the North Sea waters, as indicated in Figure 1.1. Compared to bottom-fixed solutions installed in deep waters, floating offshore designs are expected to have lower design and installation costs. In addition, floating offshore designs are expected to produce more energy, being able to accommodate bigger wind turbines in order to lower the final cost per MWh (Huera-Huarte 2013).

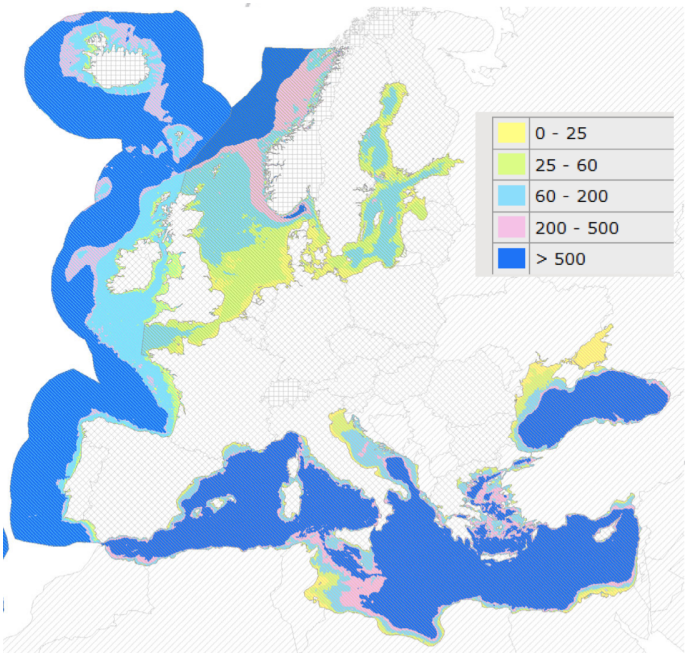

Figure 1.1: European bathymetry map (Orecca 2022)

However, the design process for OWT substructure concepts is complicated as relevant environmental conditions must be defined for each concept individually (Müller et al. 2017). This is due to the novel state of the FOWT technology, and with the lack of experience, it is important to carefully select design conditions for the system in order to provide a conservative yet cost effective design.

1.4 Scope

The semi-submersible FWT hull concept has proven to be competitive among existing designs. Its well-known mooring system as well as its low draft makes it highly applicable. The scope of this work is to optimize the OO-Star semi-submersible design developed by Dr.techn. Olav Olsen in order to make it more economically competitive and reduce its overall mass as well as its environmental footprint. In the analysis, the same 10 MW wind turbine as Dr.techn. Olav Olsen designed for the original hull structure, will be applied.

The aim of this thesis is to study the theoretical feasibility of supporting a 10 MW WT by a tensegrity-type semi-submersible platform. The thesis includes two parts; design and analysis. However, the two parts will overlap during the thesis.

1.5 Structure of the Report

The report is divided into sections, starting with introducing the topic and the scope of the thesis in Section 1. In Section 2, the theory used for the calculations as well as important theoretical background is presented, followed by introducing the procedure of analysing a FWT structure in Section 3. Further, in Section 4, the two semi-submersible concepts will be presented, both the one developed by Dr.techn. Olav Olsen as well as the modified concept investigated in this report. In Section 5, the method and result of the spreadsheet-based parametric design is presented, before the process of modelling the concept in SIMO-RIFLEX-AeroDyn is explained in Section 6. In Section 7, the procedure of the ULS analyses and sensitivity studies conducted will be explained, followed by their results and discussion in Section 8. Lastly, the conclusion and recommendations for further work are given in Section 9.

2 General Theoretical Background

This section will describe the relevant theory for the calculation of the modified foundation, as well as important concepts in order to understand the procedure on how to reach the final dimensions. This includes understanding the concept of a tensegrity system, as well as theory behind environmental conditions such as wind and waves. First, properties of a tensegrity system will be explained as well as the concept of a bicycle wheel. Secondly, the environmental loads acting on a FWT will be described. Then, damping and different failure modes which are relevant in this work is presented, before the theory of heave plates is discussed.

2.1 Tensegrity System

In order to reduce the material use of the OO-Star WT semi-submersible foundation, a system of tensegrity elements will be applied. Tensegrity structures have specific advantages that make them convenient for use in engineering structures. A tensegrity system consists of compressive and tensile parts, and in order for a system to be designated as a tensegrity system, there are a set of requirements that need to be fulfilled (Whittier 2002).

It is important to distinguish between the internal forces and the external forces acting on the compressive parts by the tensile parts. Obviously, there exist a set of external forces that could stabilize any configuration of compressive parts, but the definition of a tensegrity configuration depends only on the existence of a set of tensile parts that could stabilize the configuration when no external forces are acting. In the absence of external forces, the compressive parts must have torqueless connections and must be stabilized by a set of tensile members connected between the compressive parts.

The compressive beams are not compliant, although there may be some axial compliance, meaning that they do not have flexible mechanisms. Hence, there are no elastic bodies in bending, only elastic axially loaded strings which are the tensile wires. Material bending is thus not present in this model, giving the advantage of increased accuracy of the system statics and dynamics, as bending models are more inaccurate compared to models of axially loaded structural members (Skelton and Oliveira 2009). This feature does not only simplify the equations of motion, but the models will be more accurate compared to models of bodies being subjected to bending moments.

In addition to improved models, some mass reduction can be obtained if the load directions of each body is predetermined. Loading each bar in only one direction (axially), one can take advantage of materials that handle loads in this pre-specified direction, using considerably less mass compared to a body having to withstand loads in several directions. Hence, preferably one should assure that the members in a tensegrity system are unidirectionally loaded.

Another advantageous property of tensegrity systems is that stiffness greatly depends on clever choices of geometry rather than increasing pre-stress and mass. Hence, tensegrity structures can be of very light weight in comparison to other design choices. Also, tensegrity structures are form finding, meaning that for a structure with flexible tension members, if one cable is shortened, the structure will automatically deploy, i.e. deform from its collapsed state to the stable tensegrity position.

One important downside with tensegrity structures is that they always exhibit an infinitesimal flex and must therefore be pre-stressed to resist deformation in the direction of the flex (Pellegrino and Calladine 1986). Tensegrity systems also tend to be susceptible to vibration due to the infinitesimal flex, and if this is of concern in the tensegrity structure, it must be considered. However, one of the greatest disadvantages with these configurations is that they are limited to specific geometries. Their nodal positions cannot be specified arbitrarily. This limits tensegrity structures to certain positions.

2.2 The Principle of a Bicycle Wheel

The spokes on a bicycle wheel distribute the load throughout the wheel while holding the rim circular. The spokes are in tension, suspending the rim around the hub (Glaskin 2015). The spokes on an unloaded wheel are given a pretension, allowing the spokes to carry the load without buckling, always remaining in tension. This is important since a spoke is incapable of supporting a significant amount of compressive load due to its slenderness (length to diameter ratio), making it prone to buckling (Mínguez and Vogwell 2008). This leads to the requirement that the magnitude of the pretensioned load must be sufficient to always keep a spoke in tension.

2.3 SpiderFLOAT

SpiderFLOAT is an innovative support structure concept developed by the National Renewable Energy Laboratory (NREL) (NREL 2019). It is a floating substructure designed for a 10 MW reference WT. Similar to the tensegrity concept studied in this work, the SpiderFLOAT substructure concept is a system of beams and tension-only members. SpiderFLOAT has minimum bending on the members due to low fixity level of the joints (Damiani and Franchi 2021). The concept also aims at mass minimization, driving down the cost of deepwater wind energy, as is the goal of the present work. The SpiderFLOAT applies reinforced concrete, while the buoyancy cans at the ends of the three legs attached to the centered column (Tetteh et al. 2022) as seen in Figure 2.1 are comprised of glass-fiber reinforced plastic.

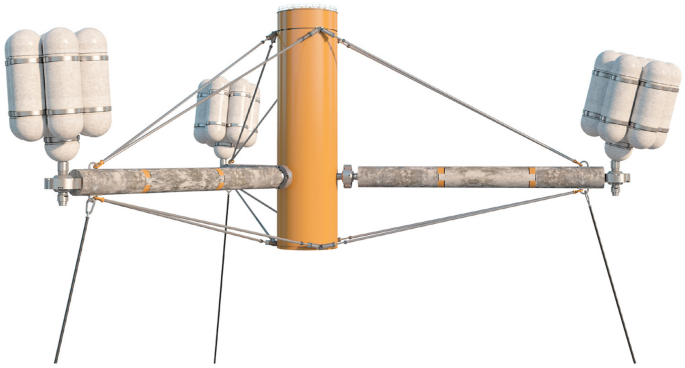

Figure 2.1: Floating Offshore Wind Turbine Foundation SpiderFLOAT (Bauer n.d.)

The slanted cables in the figure attached to the centered column have controllable length, and are under large tensional load (Stockhouse et al. 2021). The SpiderFLOAT has a radius of 35 m from the center of the shaft to the leg tip (Dinius et al. 2022), and has a total mass, including the tower and the turbine, of 4 243 t.

2.4 Wind

The short-term description of wind speed U(x,y,z) in a single point, can be expressed as the sum of a constant deterministic wind speed $\bar{U}$ which does not vary in time, and a stochastic term u(x,y,z,t) which varies in time. The stochastic term can be described with a spectrum which will be explained in Section 2.4.3. The mean wind speed however, can be represented by two typical models; the power profile and the log profile which will be described in Section 2.4.5. These are spatial variations in the wind which also will be the subject in Section 2.4.4. But first, an important property of wind that should be considered when looking at the forces acting on a

WT will be considered, which is the wind turbulence.

2.4.1 Wind Turbulence

Wind turbulence significantly influences the response of a wind turbine as well as its fatigue loads. With increasingly larger turbine sizes, they are being installed and operated at greater heights and hence further into the atmospheric boundary layer, having significantly different turbulence characteristics compared to closer to the ground. When the towers become taller, also the rotors become larger and more flexible, resulting in vibratory energy flux which is likely to influence the creation of fatigue damage. Turbulent fluxes may not be uniform across large turbine rotor disks (Kelley 2011). Neither may the temporal and spatial distribution of the wind field, nor the wind shear (Nybø et al. 2020), which are concepts that will be explained in the sections below.

The turbulence intensity I is given as the ratio between the standard deviation of the wind speed σ_u and the mean wind speed $\bar{U}_{ref}$ at a reference height z_{ref},

$$I = \frac{\sigma_u}{\bar{U}_{ref}}, \tag{2.1}$$

and tends to be largest for low wind speeds (Manwell et al. 2010). How the wind turbulence can be simulated will be explained in the following section.

2.4.2 TurbSim

In order to produce the wind data and simulate the inflow turbulence in the wind, the stochastic, full-field, turbulent-wind simulator TurbSim can be used (Jonkman 2016). It is developed by the US Department of Energy's National Renewable Energy Laboratory (NREL). The simulator uses a statistical model in order to numerically simulate time series of three-component wind speed vectors at points in a vertical rectangular two-dimensional grid, covering the whole area of the rotor. It mimics the statistical characteristics of atmospheric turbulence. The FWT moves through the sections where the turbulent wind is defined by advancing the resulting turbulence box through space at the mean wind velocity. It is assumed that the wind turbine's wake moves downstream faster than the turbine, such that the WT does not encounter its own wake as it moves. This is a reasonable assumption; typical surge motions are sufficiently slow to not affect the wake dynamics significantly (de Vaal et al. 2014).

2.4.3 Wind Spectra

The stochastic term of the wind speed can be described by a spectrum. The wind spectrum provides information about the power spectral density, i.e. how the wind in one point varies with frequency. Most energy is concentrated in the low-frequency region where turbulent energy is created, mainly induced by the turbulence intensity (Li et al. 2019). This is also the most relevant region for OWT response (Godvik 2016). At high frequency range, the response is not as sensitive to the turbulence intensity, which represents how strong the wind varies with time.

The most commonly used wind spectrum for atmospheric wind is the Kaimal spectrum. It is recommended by the IEC design standard for wind turbines (International Electrotechnical Commission 2005), and expressed as in Equation (2.2),

$$\frac{fS_k(f)}{\sigma_k^2} = 4\frac{\frac{fL_k}{U_{hub}}}{(1+6\frac{fL_k}{U_{hub}})^{5/3}}, \tag{2.2}$$

where f is the frequency, $S_k(f)$ is the one-sided frequency spectrum, σ_k is the standard deviation of the velocity component, k is the index representing the velocity direction, L_k is the integral scale component of the velocity, and U_{hub} is the velocity at hub height.

Other wind spectra that exist are the Frøya, Mikkelsen and Davenport, as well as the von Karman spectrum which is commonly applied for wind tunnels. These will not be described further in this thesis as they are not relevant.

2.4.4 Spatial Coherence Models

The spectra described in Section 2.4.3 provide us with information about the variation of the wind with frequency in one point. However, they do not include spatial variations, such as the relationship between the time series of the wind velocities in two different points in space. These correlations decrease as the distance separating the two points increases, as well as when having large frequency variations. Hence, spatial coherence models provide information about the correlation as a function of frequency and separation between the points (Burton et al. 2011).

The two most applied coherence models are the Kaimal and the Mann shear models. Both are stationary and intended for neutral atmospheric conditions, meaning that a rising parcel of air remains at the same temperature as its surrounding environment (Auburn University 2021). These models will be explained in the following.

2.4.4.1 The Kaimal Spectral and Exponential Coherence Model

The Kaimal spectral and exponential coherence model can be simulated by a Fast Fourier Transform (FFT), and is based on measurements over a field. It uses an exponential coherence function as shown in Equation (2.3), where the coherence γ depends on the separation distance r between the points and the frequency f. L_c is the coherence scale parameter. The Kaimal model only includes coherence in the longitudinal direction, i.e. does not model coherence for the lateral and vertical velocity components (Nybø et al. 2020).

$$\gamma(r, f) = exp\left(12\sqrt{(\frac{fr}{U_{hub}})^2 + (\frac{0.12r}{L_c})^2}\right) \tag{2.3}$$

2.4.4.2 The Mann Uniform Shear Model

The Mann uniform shear model is a spectral tensor model that includes three-dimensional coherence, i.e. in the longitudinal, lateral and vertical directions. Similar to the Kaimal coherence model, also the Mann model uses a FFT in order to generate time histories of the wind from the spectra, but a three-dimensional FFT must be applied in order to generate all three turbulence components simultaneously (Burton et al. 2011).

According to a study performed by Bachynski and Eliassen (Bachynski and Eliassen 2018), the Mann model gives overall smaller surge and pitch excitations, as well as larger responses in yaw, sway and roll, compared to the Kaimal model.

2.4.5 Wind Shear

In addition to the temporal variations in the wind, there will also be spatial variations in the mean wind speed with height above the ground due to the viscous boundary layer at the earth surface slowing down the wind speed. This variation is called wind shear. To formulate this effect, two common models are applied, which are the power model and the logarithmic model. The power law is formulated as in Equation (2.4), where α is the power law exponent which varies according to the stability of the atmosphere, $\bar{U}_{ref}$ is the wind speed at the reference height z_{ref}, and z is the height above the MSL. α is commonly set to 0.14 [-] for offshore locations (International Electrotechnical Commission 2009).

$$\bar{U}(z) = \bar{U}_{ref}(\frac{z}{z_{ref}})^{\alpha} \tag{2.4}$$

2.5 Ocean Waves

Two parameters are often used to describe waves; the significant wave height H_s, and the peak period T_p. H_s is the mean height of the one-third largest waves, and T_p is the period in the spectrum having the largest energy.

Ocean waves are highly stochastic, meaning that they have random values for different instants in time on some interval. However, stationarity is often a good assumption over a period of several hours, meaning that statistical properties such as the expected values, the standard deviation and the mean value are constant in time.

Fluid flow can reasonably be approximated as incompressible, irrotational and inviscid, enabling the application of linear potential wave theory even though ocean waves are composed of several non-linear components. Using linear potential theory, irregular seas can be simulated by a sum of linear wave components with different frequencies. Equation (2.5) expresses the wave elevation for long-crested waves propagating in the positive x-direction. A_j is the wave amplitude, ω_j is the circular frequency, t is the time, k_j is the wavenumber and ϵ_j is the random phase angle of wave component number j (Faltinsen 1990). For deep water waves, ω_j and k_j are related by the dispersion relationship $\frac{\omega^2}{g} = k$.

$$\zeta(t) = \sum_{j=1}^{N} A_j \sin(\omega_j t - k_j x + \epsilon_j) \tag{2.5}$$

The wave amplitude A_j can be expressed by a wave spectrum $S(\omega)$ as shown in Equation (2.6), where $\Delta\omega$ is a constant difference between successive frequencies (Faltinsen 1990).

$$\frac{1}{2}A_j^2 = S(\omega_j)\Delta\omega \tag{2.6}$$

The wave spectrum will be described in the next sections. There exist several wave spectra in order to describe the sea surface based on measured wave data. The Pierson-Moskowitz (PM) spectrum and the Joint North Sea Wave Project (JONSWAP) spectrum are the most used for describing wind-generated seas, and are

single peak spectra.

2.5.1 The Pierson-Moskowitz Spectrum

Equation (2.7) are spectra belonging to the PM type spectra, which are valid for unlimited fetch (the distance in which the wind blows over the sea before reaching land) and for fully developed sea states. The spectrum is based on data from the North Atlantic Ocean, and relies on the assumption that it will approach the curve ω^{-5} for $\omega \to \infty$.

$$S(\omega) = \frac{A}{\omega^5}\exp[-\frac{B}{\omega^4}] \tag{2.7}$$

A and B in Equation (2.7) are given as

$$A = 0.0081g^2$$

$$B = 0.74(\frac{g}{U})^4,$$

where the only parameter is the wind speed U given at 19.5 m altitude. g is the acceleration of gravity and ω is the angular frequency given in rad/s.

2.5.2 The JONSWAP Spectrum

A project in 1968-1969 in the North Sea resulted in the JONSWAP spectrum, also known as the "Joint North Sea Wave Project". It is a spectrum most relevant for North Sea conditions. It is based on the PM spectrum, but instead of the wind speed, one introduces the peak frequency ω_p to the PM spectrum:

$$A = \alpha g^2$$

$$B = \beta\omega_p^4.$$

By inserting these expressions for A and B into Equation (2.7) and multiplying with the peakedness factor γ, the JONSWAP spectrum result in

$$S(\omega) = \alpha\frac{g^2}{\omega^5}\exp[-\beta(\frac{\omega_p}{\omega})^4]\gamma^{\exp[-\frac{1}{2}(\frac{\omega-\omega_p}{\sigma\omega_p})^2]}, \tag{2.8}$$

where α is the spectral parameter, β is the form parameter, and the standard devi-

ation is given by

$$\sigma = \begin{cases} 0.07 \text{ for } \omega \leq \omega_p \\ 0.09 \text{ for } \omega > \omega_p. \end{cases}$$

The peakedness factor γ is a value between 1 and 7 and is proportional to the ratio between the maximum energy in the JONSWAP spectrum and the maximum energy in the PM spectrum.

For $\gamma = 1$, the JONSWAP and the PM spectra are identical. In addition, the areas under the spectra will be equal in case they are used to describe the same sea state, meaning that the total energy in the sea state is equal. However, the two spectra differ in their energy distribution along the frequency axis. The JONSWAP spectrum will concentrate more of the energy close to the peak frequency compared to the PM spectrum, as seen in Figure 2.2.

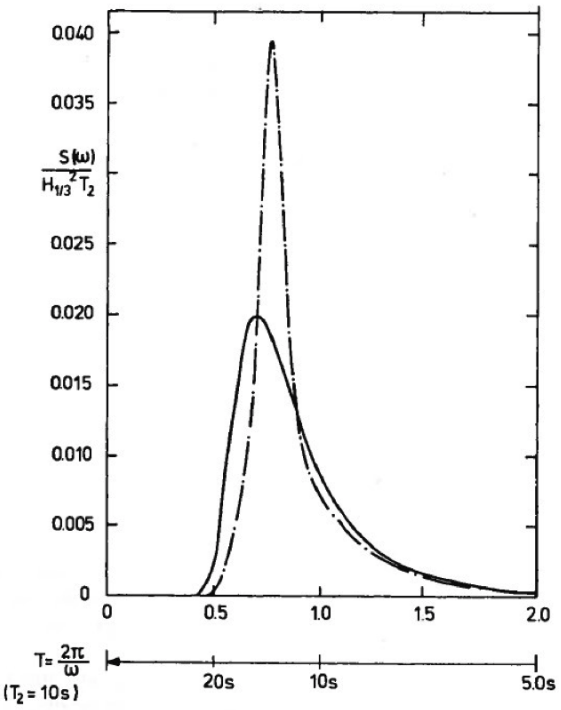

Figure 2.2: Examples of the Pierson-Moskowitz spectrum (solid line) and the JONSWAP spectrum (dotted line). $H_{1/3}$: significant wave height, T_2: wave period (Faltinsen 1990).

2.6 Damping

Damping is the transformation of energy from a vibrating structure into other forms of energy, thereby removing energy from the structure causing a reduction in the system's response (Puthanpurayil et al. 2011). Vibrational motion that occurs due

to wind and waves acting on a FOWT is most commonly not desired. It can result in early structural fatigue and/or failure, and in many cases unwanted noise. In order to reduce its extent, one can dissipate the vibration energy which represents the structure's damping characteristics, and thus the structure's ability to suppress unwanted vibration. This becomes particularly relevant for the total response when the system is close to resonance. The specific ways the energy is dissipated in vibration depend upon the physical mechanisms active in the structure. The physical mechanisms are complicated physical processes which are not fully understood. Which mechanisms that are predominant in the structure in a given situation will govern which types of damping that are present. Hence, mathematical representations of the physical damping mechanisms in the equations of motion of a vibrating system will be an approximation and generalization of the real physical situation due to the many contributions. Hence, a mathematical damping model does not give a detailed explanation of the underlying physics (Adhikari 2001), and in practice, it is necessary to rely on approximation from both theoretical and empirical knowledge.

As will be shown in Section 3.2.4.2, one way of obtaining the structural damping is to use Rayleigh damping. As steel cables are flexible, they are prone to vibration since they have low inherent damping characteristics (Yamaguchi and Fujino 1998). Vibration can result in cable or connection failure, reducing the life of the structure (Johnson et al. 2003). A stiffness proportional damping coefficient α_2 may hence be needed, damping out the modes with high frequencies. In practical applications, α_2 is selected to give a realistic energy dissipation at the peak period of the loading (SINTEF Ocean 2021).

2.6.1 Active and Passive Damping

In order to increase damping, there are two main methods; passive damping and active damping. Due to high costs and complexity, the implementation of active and semi-active damping has been slow. Such systems use added power in the form of electronically controlled sensors and actuators in closed-loop systems. They can even be tuned to remove resonances, unlike passive systems.

Passive damping is a well-developed method and is in general more cost-effective and simple (Park and Choi 2004). Passive vibration damping systems often uses a mechanical device or a fluid to reduce the vibration, or it can be achieved with viscoelastic materials such as polyurethane. However, passive vibration dampers tend to be less effective when compensating for vibrations occurring in more than one direction (Collins 2019).

2.6.2 Polyurethane

Polyurethane is a class of polymers composed of organic units which are good dampers. Unlike other common polymers such as polyethylene and polystyrene, polyurethane is produced from a large range of materials, and is therefore a class of polymers and not a distinct compound, allowing for different physical properties. A great advantage of polyurethane material is their abrasion resistance, which is superior to plastics' resistance. This is due to the elastomeric properties of polyurethane which plastics lack. Polyurethane will also return to its original shape when it has been stretched, and is good at shock absorption.

It is the polyurethane's viscoelastic nature that makes it a convenient passive damper (Gallagher 2022). Each cycle of vibration causes strain and friction in the polyurethane which converts mechanical energy into thermal energy which is dissipated as heat.

2.6.3 Damping of a Moored Floating Body

For a moored floating body, several processes contribute to the damping of the system (Langen and Sigbjörnsson 1979). They can be divided into two categories: structural damping and hydrodynamic damping. Also, damping effects created by drag on the mooring lines must be considered. This damping will depend on water particle velocity and the mooring lines' diameter, as well as the drag coefficient.

2.6.3.1 Structural Damping

The structural damping is caused by the material composition of the system in question, and by the couplings between the elements in the system. The damping is mainly due to the internal frictions and displacements in the material when the material is elastic. Such damping may vary with temperature, load size, load amplitude and load frequency due to its dependency on the internal characteristics of the structure's material.

2.6.3.2 Hydrodynamic Damping

Hydrodynamic damping is dependent upon the geometry of the body and the frequency of the oscillation of the system. Hydrodynamic damping includes three different contributions: potential damping, viscous damping and skin friction due

to shear forces (Larsen et al. 2019).

1. Potential damping result from the waves created due to the oscillation of the body at or close to the free sea surface. During this process, the motion energy of the body is transferred into wave energy.

2. Viscous damping is a result of vortices created by the body as it moves in water. The damping force is said to vary proportionally with the squared of the oscillation speed of the body. It can be calculated with the drag term in Morison's equation.

3. The damping from skin friction due to shear forces between the body and the water can be neglected for large structures since the potential and viscous damping sources are a magnitude larger.

2.6.4 Dynamic Load Factor

Figure 2.3 show the dynamic load factor for a 1 degree of freedom (DOF) elastic dynamic system as a function of the frequency ratio β, where ω and ω_0 are the load frequency and the natural frequency, respectively. The dynamic load factor is defined as the ratio between the dynamic and static displacement (Langen and Sigbjörnsson 1979),

$$\frac{|H(\omega)|}{H(0)} = \frac{(u_{max})_{dyn}}{(u)_{stat}} = \frac{1}{((1-\beta^2)^2 + (2\lambda\beta)^2)^{\frac{1}{2}}}, \tag{2.9}$$

where $H(\omega)$ is the complex frequency-response function, and its absolute value represents the mechanical transfer function. $H(0)$ is the static displacement, and λ is the damping ratio.

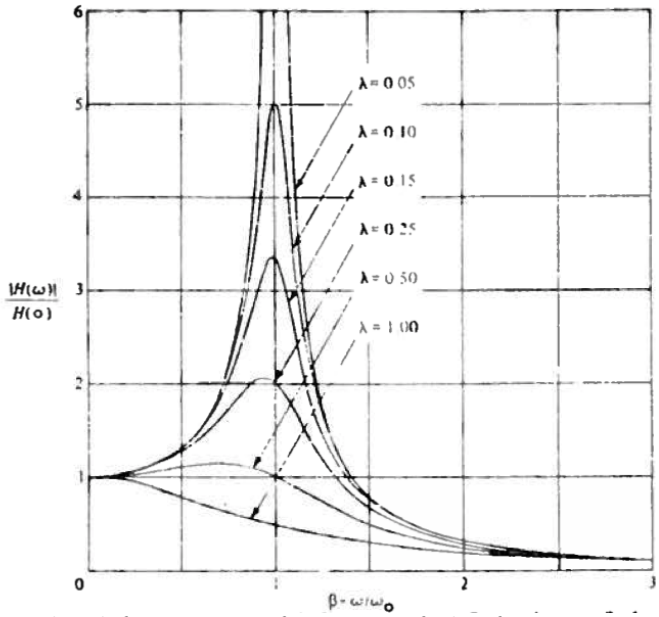

Figure 2.3: Dynamic load factor as a function of the frequency ratio (Langen and Sigbjörnsson 1979)

It can be seen from Figure 2.3 that the dynamic load factor goes to infinite at resonance when the damping λ goes to 0. Based on the same figure, the vibration problem can be divided into three special cases:

- $\beta \ll 1$: Stiffness controlled vibration (quasi-static)
- $\beta \approx 1$: Damping controlled
- $\beta \gg 1$: Inertia (mass) controlled vibration

For stiffness controlled vibration, the load frequency ω is small. When the load frequency is close to the natural frequency however, the system may experience resonance, and damping will be effective in order to limit the response. For inertia controlled vibration, the load frequency is large, and the structure is not able to catch up, implying that the dynamic response will be small.

2.7 Failure Modes

There are several failure modes relevant for the concept studied in this work which are important to be aware of. However, they will not be assessed in detail during this thesis, except from the ULS capacity of the concept.

2.7.1 Corrosion of Guy Wires

A guy wire is a tensioned cable, wire or rope which is designed to brace, guide or secure structures that are of considerable height and not self-supporting. The cables are subjected to high tension, and hence guy wires must be of considerable strength (Jingyoung 2021).

One of the main problems associated with the integrity and performance of metallic components, concerns the contact between the metal and seawater. Steel wires in contact with seawater can lead to corrosion of the material, resulting in rupture (Abriox 2019). There exist several methods to prevent corrosion, which are different in cost, performance and maintenance.

Cathodic protection is one possible solution to this problem. It is one of the most common and effective methods for preventing corrosion. The metal to be protected is connected to a more easily corroded sacrificial metal, acting as the anode, and then a DC current is passed between the two metals. The sacrificial metal hence corrodes instead of the protected metal. Two methods can be used to distribute cathodic current around the area to be protected. Either one can use an external galvanic anode, where the DC current arises from the natural difference in potential between the metals of the anode and the metal to be protected. Alternatively, one can use an external DC power source to impress a current through an external anode onto the surface of the protected metal, which then becomes the cathode (Lawson 1988; Reis Tagliari et al. 2019).

Another method in order to prevent corrosion is coating of the metal to be protected. The coating then acts as a barrier in order to inhibit the contact between corrosive materials. Several different coatings are available, such as epoxy and zinc. In cases of access difficulties, maintenance becomes challenging, and the use of highly effective, and often more expensive, coating is preferred.

2.7.2 Creep of Polymers

An alternative to steel which is prone to corrosion, is to apply polymers. This is a material having low density and favourable stiffness and damping characteristics, and which energy may be dissipated in different ways (Finegan and Gibson 1999). The major contribution, however, comes from the viscoelastic properties of polymeric materials, meaning that they present a reversible response, i.e. can return to their initial state (Chatzigeorgiou et al. 2017).

A disadvantage with polymer materials, however, is that they are prone to creep due to their viscoelastic properties (Jansen 2015). Creep causes a permanent change in dimension, and can lead to rupture either due to excessive deformation or due to cracking. It occurs to parts exposed to continuous stress below the yield strength of the material over an extended period of time, which will lead to a change in strain.

2.7.3 Ultimate Strength

The ultimate strength is the maximum load the structure shall sustain over its design lifetime in normal operation. A structure experiencing stresses exceeding the ultimate tensile strength is prone to rupture of the material. The ultimate strength is generally found by performing a test, measuring the engineering stress versus the strain. The highest point on the resulting stress-strain curve is the ultimate strength.

The construction costs of a WT constitute a considerable part of the overall initial investment, and depend on the structural design. In turn, the structural design depends on the ultimate (ULS) and fatigue (FLS) loads encountered during the structure's life. Semi-submersible WTs are subjected to a range of load conditions, caused by the environment (wind, waves, current, ice), by their operation (tow-out and installation, start-up, shutdown, normal operation, idling, parked, and in some cases faulted), and, perhaps, by accident (loss of mooring line, fire, ship collision) (E. Bachynski 2014). All these conditions must be accounted for when designing the semi-submersible WT, as well as its different components, and must be considered when calculating the ultimate strength.

Major failure modes in ULS are yielding, plastic mechanisms, overturning, capsizing and buckling (Amdahl n.d.; Det Norske Veritas 2013). For steel components, the most important material properties are the Young's modulus E, the yield point σ_y, and the ductility (Moan 2004). Ductility refers to the energy absorption ability of the steel before failure. In normal situations, structural steel is ductile, but can become brittle under certain conditions such as low temperature, high loading speed, unfavorable chemical composition and unusual (triaxial) states of stress and high level of residual stress. This can lead to the undesirable event of brittle fracture.

2.7.4 Fatigue

Material fatigue is the process in which small cracks in a component initiate and grow under the influence of a repeated loading (Ekberg 2009). Such processes are

difficult to observe and measure. Nano and micro scale cracks go undetected during normal inspection methods, and when a visible crack has formed after cyclic loading, the structure may already be close to failure. Marine structures are generally subjected to dynamic loads, and even if the load stays below the allowed stress, the cumulative effect of the varying load may cause fatigue cracks at locations with high stresses (Berge and Ås 2017).

A sign of fatigue is small cracks appearing due to repeated bending of for example a wire rope, developing points of stress concentrations, leading to loss of strength if the wires cannot adjust to their changed position. By repeated bending, the cracks may spread (Technology 2021).

Also, fatigue due to corrosion could cause challenges. This is the combined action of an alternating stress and a corrosive environment (AMPP 2022). The fatigue process can cause rupture of the metal, upon which corrosion is accelerated. When the metal is exposed to a corrosive environment, the failure can take place at even lower loads and after shorter time. A maximum tension of 300 MPa has been set in this work, but due to corrosion fatigue, this limit can be reduced. However, the purpose of this work is to investigate if this is a realistic concept from a global dynamic perspective, and this limitation is outside the scope of the work.

There are several approaches in order to perform a fatigue analysis. One can use an empirical S-N curve on the form shown in Equation (2.10), which plots the nominal stress range ΔS as a function of number of cycles to failure N, under the condition that specific criteria on fabrication standards are fulfilled. These curves are based on physical laboratory tests.

$$N \cdot (\Delta S)^m = K \tag{2.10}$$

In Equation (2.10), m is the slope of the S-N curve and K is the stress intensity factor which depends on the specimen geometry, the size and location of the crack or notch, and the magnitude and distribution of loads on the material.

On log-log scale, Equation (2.10) becomes, in most cases, linear or bi-linear (Berge and Ås 2017)

$$log(N) = log(K) - m \cdot log(S). \tag{2.11}$$

To estimate the fatigue lifetime of a structure, one must first determine the stress

time history at different points on the structure, in particular near welds and bolts. This is obtained from the dynamic finite element (FE) results. The hot spot stress can then be determined by applying the appropriate concentration factor, which accounts for global stress concentrations due to cut-outs or eccentricity in the calculated nominal stress, before evaluating the S-N curve (Berge and Ås 2017).

From the stress time history, the number of load cycles at different stress levels can be computed. For this purpose, different procedures exist, commonly referred to as cycle counting. The rainflow counting technique developed by Matsuishi and Endo (Anzai and Endo 1979) is generally considered the best method for fatigue damage estimation, at least for metal structures (Naess and Moan 2013). This method counts effective stress ranges based on the time history of peaks and valleys.

Having found the number of stress cycles for different stress levels S_i, the fatigue damage D is found by the Palmgren-Miner's rule

$$D = \sum_{i=1}^{n_s} K^{-1} n_i S_i^m, \tag{2.12}$$

where n_s is the total number of stress levels in the simulation time history, and n_i is the number of cycles at the different stress levels S_i. An S-N curve with slope m is assumed in Equation (2.12) (DNV 2015).

2.7.5 Fretting

In the case of a multilayer stranded steel wire or rope, fretting fatigue is considered to govern the fatigue life, which is due to stress concentration in the trellis contact points or in the contact between adjacent 'parallel' wires (Hobbs and Raoof 1996; Suh and Chang 2000). Trellis contact points are contact between the layers of the spiral strand. Fretting fatigue is the combined effect of fretting and fatigue and often also corrosion effects. According to Stephens et al., fretting is defined as

"*a surface wear phenomenon occurring between two contacting surfaces having oscillating relative motion of small amplitude.*"

Failures due to fretting fatigue result from micro cracks that arises in the fretting region. These may grow with cyclic stresses until fracture (Stephens et al. 2000).

2.7.6 Slamming

Slamming are impulse loads with high pressure peaks occurring during impact between a body and water (Faltinsen 1990). Slamming is very localized in space, and has a duration of the order of milliseconds. Slamming may occur due to steep breaking waves and should be avoided as it induces high loads to the body, and may cause significant structural damage. Slamming might affect the ULS and FLS design of OWTs.

2.7.7 Snap Loads

When a light to moderate pretensioned line goes into slack, snap loads may occur during re-engagement (Hsu et al. 2014). Such loads can result in shock on the line material and reduce its fatigue life. These loads may occur in various sea states and is not necessarily limited to extreme conditions.

2.8 Heave Plates

Heave plates are useful in order to increase a structure's natural period as well as damping in heave, roll and pitch, and to reduce the platform motions. However, the construction of heave plates can be complex and expensive. They are often used on semi-submersible and spar platforms, and provide the structure with increased added mass due to the large amount of water that is displaced when the platform moves. The increase in added mass result in an increase in natural period, urging to move the periods of the structure away from the wave energy spectrum. In addition, the sharp edges on heave plates give an increased vortex shedding, causing a larger damping force which reduces platform motions (D. Roddier et al. 2011). The generation of vortices depend on the thickness-to-diameter ratio of the plate as the flow field will be different for a thin plate than a thick plate. However, the effect of changing the thickness of the heave plate will not be studied in this thesis.

In order to estimate the added mass and damping due to heave plates, experiments as well as computational fluid dynamics (CFD) calculations are necessary. This is due to the importance of viscous forces, giving a highly non-linear problem. Several studies have been conducted concerning this, as heave plates have been used in the oil and gas industry for a long time, and are often necessary in FWT support structures. One of these studies will be used in this thesis, and will be discussed in the following.

The hydrodynamic properties of heave plates depend on, among others, the ratio between the diameter of the heave plate and the diameter of the column it is attached to, the porosity, the plate thickness-to-diameter ratio and the oscillation amplitude and frequency. Numerical studies on a column with a circular heave plate attached to one end are presented by Longbin Tao and Cai (2004), Longbin Tao and Thiagarajan (2003) and Tao et al. (2007). These studies were all conducted in deep water conditions, with a circular heave plate deeply submerged.

The effect of the heave plate is reduced when a column is attached to it, especially the added mass since less water is entrapped. The theoretical added mass of a circular disk oscillating vertically in infinite water is found by

$$A_{33} = \frac{1}{3}\rho D_{hp}^3, \tag{2.13}$$

where D_{hp} is the diameter of the heave plate (DNV GL 2017). With a cylinder attached to the circular disk, Tao et al. (2007) suggested that the theoretical added mass could be calculated by

$$A_{33,hp} = \frac{1}{12}\rho(2D_{hp}^3 + 3\pi D_{hp}^2 z - \pi^3 z^3 - 3\pi D_{cc}^2 z), \tag{2.14}$$

where $z = \frac{1}{\pi}\sqrt{D_{hp}^2 - D_{cc}^2}$, and D_{cc} is the diameter of the cylinder. The potential added mass is highly influenced by the D_{hp}/D_{cc} ratio, but this will not be studied in this thesis.

Non-linear effects occur in the presence of heave plates, especially in the present case where the hydrodynamics are not symmetric with regards to the motion and the column geometry; moving downwards, the surface perpendicular to the flow is the entire disc, whereas moving upwards, the presence of the column reduces the pressure loads on the disc (Lopez-Pavon and Souto-Iglesias 2015). However, analysis of these nonlinearities is beyond the scope of the present work.

A large ratio between the disc depth and the disc radius implies that the flow hardly will be influenced by the free surface (Lopez-Pavon and Souto-Iglesias 2015). Lopez-Pavon and Souto-Iglesias (2015) also found that there is a relatively low dependence between the added mass and frequency for large depth-radius ratio, which is also well documented in the literature.

3 Analysis of Floating Wind Turbine Structures

Semi-submersible WT systems are complex and dynamic, and exposed to time-varying environmental loads such as turbulent winds, random waves and current. When such loads act on a flexible integrated structure having a range of natural frequencies, one must ensure that the WT is not excited by these loads. In addition, the WT may experience various operational, start-up, shut-down and failure modes. These are all aspects that must be taken into account in the dynamic analysis of a semi-submersible WT in order to obtain a reasonable accurate model. Hence, frequency-domain methods are not suited for flexible structures exposed to time-varying loads.

At a minimum, considerations of aerodynamics, hydrodynamics, control systems and structural mechanics are required in the dynamic simulation of offshore WT systems. Additional considerations, such as drivetrain mechanics, interaction between the mooring lines and the soil and electrical considerations can also be included, but are outside the scope of this work. In the coupled analysis, the complete system of equations including the rigid body model of the floater and slender body models of blades, tower and mooring lines, are solved simultaneously in time domain. The aerodynamics, the structural dynamics, the hydrodynamics, and the servo dynamics will be explained in the following sections, followed by defining the term eigenfrequency as well as the procedure and reason for conducting an eigenvalue analysis. Lastly, SIMO-RIFLEX-Aerodyn, which is the software used in this work, will be introduced.

3.1 Wind Turbine Aerodynamics

A wind turbine rotor extracts kinetic energy from the incoming wind by applying a thrust force T which slows down the wind speed. In this way, power can be extracted. The theoretical upper limit of the aerodynamic efficiency for wind power extraction is called the Betz limit, and is 59.3% (Burton et al. 2011). Modern wind turbine efficiency reaches as high as 50%, but since the WT sets the fluid flow into rotation, giving a loss, as well as losses from for example drag, gears and electrical losses, the Betz limit is not obtained.

The blade element momentum (BEM) and the generalized dynamic wake (GDW) aerodynamic models are two methods that are computationally efficient in order to investigate WT aerodynamics. Neither method accounts for large rotor cone nor

large blade deflections as they assume the rotor plane being a flat disk. However, they are still regarded as methods giving accurate enough results for many operational conditions (M. O. L. Hansen et al. 2006).

3.1.1 Blade Element Momentum Model

The blade element momentum theory is one of the most commonly used methods to calculate the induced velocities on wind turbine blades. The theory is an extension of the actuator disk theory, which describes a mathematical model of an ideal actuator disk and assumes static flow. The BEM model assumes that the blades can be divided into small elements along the span, acting independently of surrounding elements, and that they aerodynamically act as two-dimensional airfoils. The elemental forces can then be summed up along the blade to find the total forces acting on the turbine (Moriarty and A. Hansen 2005). As opposed to the GDW model, the BEM model requires iteration of the axial and rotational induction factors (Macquart et al. 2012).

Several corrections are taken into account in the BEM theory, such as corrections for tip and hub loss, Glauert correction for high induction factors, skewed wake, as well as the influence of the tower. Sections 3.1.3 and 3.1.4 will explain these modifications in more detail.

3.1.2 Generalized Dynamic Wake Model

The generalized dynamic wake model, also known as the acceleration potential method, is based on a potential flow solution to the Laplace's equation (Moriarty and A. Hansen 2005). Since the GDW model is limited to lightly loaded rotors and assumes the induced velocities being small relative to the mean flow, it is used for mean wind speeds above 8 m/s as the method will be unstable at low wind speeds (Laino and A. C. Hansen 2004). Inherent in the model is dynamic wake effects, tip losses and skewed wake dynamics, whereas wake rotation is not included. Compared to the BEM model, the GDW model is the preferred model for dynamic flow, higher wind speeds and yawed inflow as it has a fully non-linear implementation to account for turbulence and spatial variations in the flow. The theory also allows for a more general distribution of pressure across the rotor plane compared to the BEM theory.

3.1.3 Corrections

Due to the many assumptions made of the reality when applying the BEM model, several corrections have to be implemented in order to arrive at a more true description of the dynamics experienced by a WT. Some of these are described in the following. Also the GDW model applies some of these corrections, although many of them are inherent, such as the dynamic wake effect, tip losses and skewed wake aerodynamics (Moriarty and A. Hansen 2005).

- Tip loss: this correction takes into account the vortices shed from the blade tips into the wake, which is one of the major limitations to the BEM theory. The vortices create helical structures in the wake and influences the induced velocity distribution at the rotor. The effect of induced velocity in the rotor plane is most pronounced close to the tips of the blades. To compensate for this, a theory developed by Prandtl can be applied in the BEM theory (Moriarty and A. Hansen 2005).
- Hub loss: similar to the tip loss, the hub loss correction serves to correct the induced velocity from a vortex being shed near the hub of the rotor. In the case that an element's local aerodynamics is affected by both the tip loss and the hub loss, the two correction factors are multiplied together (Moriarty and A. Hansen 2005).
- High induction factor: Figure 3.1 shows that for high rotor thrust coefficients C_T, the momentum theory is not valid. Glauert developed a correction to C_T for high induction factors a, which is the ratio between the induced velocity and the wind speed (J. Schepers 2007). The invalidity is due to a reversal of the flow at high tip speed ratios, which will cause the flow from outside of the wake to enter through the boundary, increasing the turbulence in the flow (Moriarty and A. Hansen 2005).

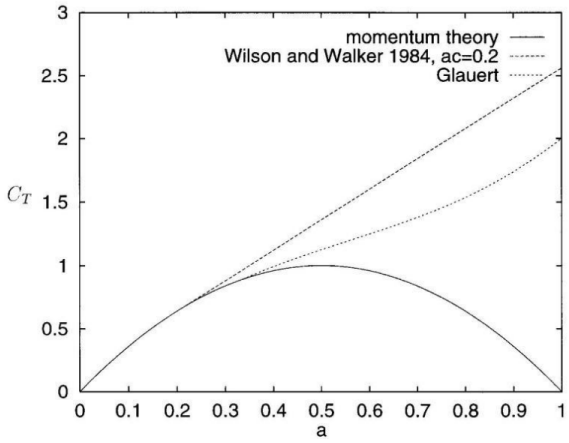

Figure 3.1: Glauert correction (M. Hansen 2015)

- Skewed wake: this phenomenon is caused by non-aligned inflow wind and rotor plane, for example if the WT has a yaw or pitch angle relative to the incoming wind, or if the rotor is tilted. In this case, the wake will not move in a horizontal path, but will be skewed somewhat vertically. To account for this, an empirical correction developed by Glauert can be added to the induction factor.

- Dynamic wake: a WT will be exposed to variable wind speeds, which in turn will change the WTs rotor speed in time and hence blade pitch angle. The flow is not able to catch up immediately to these changes in time, causing a time lag in the induced velocities. This is due to vortices being shed from the blades and convected downstream. This can be modelled by the Stig Øye filter for induced velocities (Snel and J. G. Schepers 1995).

3.1.4 Influence of the Tower

The tower will have an influence on the air flow which is called tower shadow. When the blades pass the tower, they see less wind. This is also due to the wind shear described in Section 2.4.5, having an increased wind speed with height. Tower shadow will only affect the horizontal wind component, and the most common way of modelling such flow is to use 2D potential theory.

The tower will also be exposed to forces from the wind which should be taken into account. Aerodynamic drag forces on the tower are important in extreme wind conditions, in which case the forces on the parked rotor are small. In this case, the drag force can be in the same order of magnitude as the thrust force. The drag force can be found using the Morison's equation which will be described in Section 3.3.3.

3.2 Structural Dynamics

The structural dynamics considers the response of an analysis. For WTs, the response is mainly elastic as the members are long and slender and may deflect. In order to take the global structural dynamics into account, there exist several methods, each having different level of accuracy; linear rigid body analysis, modal analysis, non-linear beam analysis, or the more complex finite element (FE) method. These will be discussed in the following sections.

3.2.1 Linear Rigid Body Analysis

The simplest way of modelling a WT with its platform is by one single rigid body. The six rigid body motions can then be defined: surge (η_1), sway (η_2), heave (η_3), roll (η_4), pitch (η_5) and yaw (η_6).

By then assuming steady-state harmonic loads and responses, disregarding non-linearities, the coupled equations of rigid body motions for the floating platform in six DOFs can be written as (Faltinsen 1990)

$$\sum_{k=1}^{6}[(M_{jk} + A_{jk}(\omega))\ddot{\eta}_k + B_{jk}(\omega)\dot{\eta}_k + C_{jk}\eta_k] = F_j(\omega)e^{i\omega t}; \quad \text{for } j = 1,..., 6, \tag{3.1}$$

and on matrix form as

$$(\boldsymbol{M} + \boldsymbol{A}(\omega))\ddot{\boldsymbol{\eta}} + \boldsymbol{B}(\omega)\dot{\boldsymbol{\eta}} + \boldsymbol{C}\boldsymbol{\eta} = \boldsymbol{F}. \tag{3.2}$$

M_{jk} are the components of the dry mass of the structure, A_{jk} are the added mass coefficients, B_{jk} are the damping coefficients, C_{jk} are the hydrostatic restoring coefficients, and η_k are the motions of the structure. The dot(s) represents the time derivative(s). F_j are complex quantities representing the amplitudes of the excitation forces and moments acting on the structure, and ω is the frequency of the harmonic excitation. The subscript k denotes the mode of the six DOFs, and the subscript j represents the force direction. The equations for $j = 1, 2, 3$ result from the Newton's second law, whereas for $j = 4, 5, 6$, the equations follow from the equation of angular momentum.

The uncoupled and undamped natural frequency for the k^{th} DOF can further be

found by

$$\omega_{nk} = \sqrt{\frac{C_{kk}}{M_{kk} + A_{kk}}}. \tag{3.3}$$

Excitation forces at these frequencies may give large responses unless the damping is significant or if the excitation force is low due to for example cancellation effects. This was discussed in Section 2.6.4.

In a FWT analysis, time domain is the preferred method in order to account for non-linearities from wind and waves. However, such calculations are time-consuming. By neglecting or linearizing the non-linear effects and calculate the structure's motion in the frequency domain, one reduces the computational time (Faltinsen 1990). In this case, the excitation forces and hence the motions of the structure will oscillate harmonically with the frequency of the incoming waves. The motions can then be written as a (6x1) matrix containing the six DOFs:

$$\boldsymbol{\eta}(\omega) = \begin{bmatrix} \vdots \\ \eta_{ka} e^{i(\omega t + \theta_k)} \\ \vdots \end{bmatrix}; \quad \text{for } k = 1,..., 6. \tag{3.4}$$

η_{ka} is the amplitude of the motion and θ_k is the phase angle of the motion in DOF k.

The excitation force can be written in a similar way:

$$\boldsymbol{F}(\omega) = \begin{bmatrix} \vdots \\ F_{ja} e^{i(\omega t + \theta_{F_j})} \\ \vdots \end{bmatrix}; \quad \text{for } j = 1,..., 6. \tag{3.5}$$

Inserting Equations (3.4) and (3.5) into Equation (3.1), the system of second order coupled differential equations can be solved. Equation (3.1) is then written in matrix form in the frequency domain as

$$[-(\boldsymbol{M} + \boldsymbol{A}(\omega))\omega^2 + i\omega \boldsymbol{B}(\omega) + \boldsymbol{C}]\boldsymbol{\eta}(\omega) = \boldsymbol{F}(\omega), \tag{3.6}$$

where $\boldsymbol{M}$, $\boldsymbol{A}$, $\boldsymbol{B}$ and $\boldsymbol{C}$ are the 6x6 mass, added mass, damping and restoring matrices, respectively.

3.2.2 Modal Analysis

In dynamic analysis, using the structural deflections, also called mode shapes, in order to describe the displacements of a member, one is no longer limited to only the six rigid body motions (Langen and Sigbjörnsson 1979). The mode shapes of a structure can be found from the eigenvalue problem as given in Equation (3.7), where the n different eigenvectors $\boldsymbol{\phi}$ are linearly independent, n being the number of DOFs. An arbitrary displacement of a linear time-invariant dynamic system can then be expressed as a linear combination of the eigenvectors as given in Equation (3.8), which will make up the time-varying structural deformations (He 2001).

$$[\boldsymbol{C} - \omega^2 \boldsymbol{M}]\boldsymbol{\phi} = 0 \tag{3.7}$$

$$\boldsymbol{r} = \sum_{i=1}^{n} \boldsymbol{\phi_i} y_i(t) = \boldsymbol{\phi y} \tag{3.8}$$

In Equation (3.8), $\boldsymbol{y}$ is a vector containing the displacement amplitudes.

Even though modal analysis is computationally efficient and can be sufficiently accurate for a WT analysis if the mode shapes are determined accurately, the method requires accurate pre-processing of the system modes, and it may be challenging to add modes.

3.2.3 Non-Linear Beam Analysis

Within structural engineering, there are important non-linear properties which could be necessary to take into account (Langen and Sigbjörnsson 1979). These can roughly be divided into

- Geometrical non-linearities;
- Non-linear material properties;
- Non-linear effects which are due to interaction between the structure and the environment, or, in case of a FWT, due to the controller.

The geometric non-linearities are mainly related to large displacements, and are relevant in connection with moored structures. For WTs, the geometric non-linearity is highly relevant for the blades. Material non-linearities are generally caused by the

materials elasto-plastic behaviour, but are normally not modelled. Non-linearities due to interaction between the structure and the environment can for example be related to drag damping induced by the motion of the structure in air and/or water.

By modelling the structure using beam, shell or solid elements and using a stepwise analysis to solve the equations of motion, dynamic effects that were not captured by the previous methods are found. A non-linear beam element formulation captures higher structural modes than modal analysis without pre-processing, and is more flexible when including multiple bodies. This formulation is however less computationally efficient.

3.2.4 Time Domain Finite Element Method

The present work employ FE modelling implemented in SIMA. Some important features included in the FE formulation are that beam and bar elements are based on small strain theory, which is a reasonable assumption for application to slender marine structures. The FE formulation also includes a description of non-linear material properties (SINTEF Ocean 2021).

The governing equation for structural dynamics can be written as in Equation (3.9), resulting by requiring that the virtual work done by external forces must be equal to the sum of the virtual work absorbed by the inertial, dissipative, and internal forces (Cook et al. 2002). It is a system of coupled second-order differential equations.

$$\boldsymbol{M}\ddot{\vec{D}} + \boldsymbol{B}\dot{\vec{D}} + \vec{R}^{int} = \vec{R}^{ext} \tag{3.9}$$

In Equation (3.9), $\vec{D}$ is the system displacement vector, R^{int} are the internal reaction forces written as in Equation (3.10) for a linear elastic material, and R^{ext} are the external forces which for a FWT include for example the hydrodynamic and the aerodynamic loads.

$$\vec{R}^{int} = \boldsymbol{C}\vec{D} \tag{3.10}$$

In order to solve the governing FE equations in (3.9), a step-by-step integration method in time is used. The response is found at discrete time instants, and both explicit and implicit methods can be used for time integration. However, for structural dynamic problems, implicit algorithms are better suited.

The mass and damping matrices, $\boldsymbol{M}$ and $\boldsymbol{B}$, will be described in further detail in the following sections, as well as the numerical solution method applied.

3.2.4.1 Mass Matrix Formulation

There are several ways to formulate the mass matrix, including lumped mass and consistent mass formulations (Cook et al. 2002). In the lumped mass formulation, the mass is distributed among the nodes of the element, yielding a diagonal mass matrix (Langen and Sigbjörnsson 1979). This is advantageous as the matrix does not have to be inverted, resulting in more efficient calculations.

A consistent mass matrix, however, is formulated as in Equation (3.11) for an element i, where V is the volume of the element, ρ is the mass density, and $\boldsymbol{N}$ are the same shape functions as used in the stiffness matrix.

$$\boldsymbol{m}_i = \int_{V_i} \rho \boldsymbol{N}^T \boldsymbol{N} dV \tag{3.11}$$

The mass matrix for the whole structure is further found from

$$\boldsymbol{M} = \sum_i \boldsymbol{a}_i^T \boldsymbol{m}_i \boldsymbol{a}_i, \tag{3.12}$$

where the compatibility conditions are represented by the following formulation

$$\boldsymbol{v_i} = \boldsymbol{a_i r}. \tag{3.13}$$

In Equation (3.13), $\boldsymbol{v}$ are the DOFs of each element, and $\boldsymbol{r}$ is a vector containing the DOFs of the whole structure.

3.2.4.2 Rayleigh Damping Model

Rayleigh damping is a computationally convenient way of obtaining the structural viscous damping in an FE analysis (OrcaFlex 2021). It is specified by a mass proportional term and a stiffness proportional term as expressed in Equation (3.14) (Langen and Sigbjörnsson 1979),

$$\boldsymbol{B_{Rayleigh}} = \alpha_1 \boldsymbol{M} + \alpha_2 \boldsymbol{K}, \tag{3.14}$$

where $\boldsymbol{M}$ and $\boldsymbol{K}$ are the mass and stiffness matrices, respectively.

The modal damping for a linear dynamic system can further be formulated as a function of the non-dimensionless mass-proportional damping coefficient α_1 and stiffness-proportional damping coefficient α_2 as in Equation (3.15) (SINTEF Ocean 2021). This is possible due to the property of the structural damping matrix as defined by Equation (3.14) of being orthogonal with respect to the eigenvectors.

$$\lambda_i = \frac{1}{2}[\frac{\alpha_1}{\omega_i} + \alpha_2\omega_i] \tag{3.15}$$

Equation (3.15) show that the mass-proportional damping is effective for low eigenfrequencies ω_i, whereas the stiffness-proportional damping is effective for high frequencies. For floating structures, α_1 is typically set to zero as the rigid-body motions may be important, and the damping becomes proportional to the eigenfrequency.

When applying the Rayleigh damping model, it is important to ensure that one does not overestimate the damping at frequencies with high energies (OrcaFlex 2021). Instead, under-damping the response, reaching at a conservative result, is far less critical than the non-conservative over-damping which one wishes to avoid.

Both damping coefficients α_1 and α_2 apply to all global DOFs, making it impossible to specify different damping levels for axial, bending and torsional deformations. Hence, the Rayleigh damping model is restricted to describing the overall damping level for the structure.

3.2.4.3 Direct Time Integration: Newmark-Beta

In the SIMO-RIFLEX-AeroDyn analysis, the governing FE equations in (3.9) are solved step-by-step in time. The response is computed at discrete time instants (t = $\triangle$t, 2$\triangle$t,... , n$\triangle$t). In general, explicit or implicit methods can be used for time integration. An explicit method relies only on previous data to compute the response $\vec{D}_{n+1}$, whereas an implicit method contains the terms $\dot{\vec{D}}_{n+1}$ and $\ddot{\vec{D}}_{n+1}$ on the right hand side of the equation. Explicit algorithms require smaller time increment $\triangle t$ for stability, but the computation for each time step is more efficient. Implicit algorithms, however, require more computational time per step, but fewer steps in total (Cook et al. 2002). Implicit algorithms are preferred in structural dynamics problems, such as the analysis of FWTs.

A commonly used implicit method is the Newmark-Beta algorithms. The Newmark

relations are:

$$\dot{\vec{D}}_{n+1} = \dot{\vec{D}}_n + \triangle t[\gamma \ddot{\vec{D}}_{n+1} + (1-\gamma)\ddot{\vec{D}}_n] \tag{3.16}$$

$$\vec{D}_{n+1} = \vec{D}_n + \triangle t \dot{\vec{D}}_n + \frac{1}{2}\triangle t^2[2\beta_{nb}\ddot{\vec{D}}_{n+1} + (1-2\beta_{nb})\ddot{\vec{D}}_n], \tag{3.17}$$

where γ and β_{nb} are weighting terms determined by requirements related to numerical stability, the amount of numerical damping and accuracy (Langen and Sigbjörnsson 1979). By applying the Newmark relations to Equation (3.9), the resulting Newmark-Beta algorithms are obtained. In order for the method to be unconditionally stable, $\gamma \geq \frac{1}{2}$ and $\beta_{nb} \geq \frac{1}{4}(\gamma + \frac{1}{2})^2$ (Goudreau and Taylor 1973; Langen 1974). Algorithmic damping is introduced for $\gamma \geq \frac{1}{2}$, but the accuracy reduces from $O(\triangle t^2)$ to $(\triangle t)$.

3.3 Hydrodynamics

Waves and currents may cause significant loads on semi-submersible WT structures. This thesis considers wave loads in deep water, and does not include currents. Since the analyses are run in deep water, the sea bottom does not have to be taken into account.

Due to the range of natural frequencies, diameters and displacements of semi-submersible WTs, different hydrodynamic theories may be necessary (Faltinsen 1990). Wave loads on large-volume structures can be analysed using linear potential flow theory, which includes wave excitation effects from both Froude-Krylov and diffraction, and provides the hydrodynamic loads added mass, damping and restoring (Faltinsen 1990). This will be explained in further detail in Section 3.3.2. In Section 3.3.3, Morison's equation used to calculate the wave loads on circular cylindrical sections will be described. But first, the hydrostatics will be introduced.

3.3.1 Hydrostatic Analysis

The hydrostatics refer to the pressure when the fluid is at rest, and is an important force component on the body. The pressure p is then only dependent on the submergence z, which for a fluid with density ρ can be expressed in the following way

$$\frac{dp}{dz} = -\rho g. \tag{3.18}$$

The hydrostatic restoring coefficients defined in Equation (3.1) is a result of the change in the buoyancy force due to the hydrostatic pressure when the body moves. The non-zero terms in the hydrostatic stiffness matrix for the submerged volume are found in the following. The stiffness in heave direction is based on the mean position of the structure and on the assumption of a rigid body (Faltinsen 1990):

$$C_{33} = \rho g A_{WP}, \tag{3.19}$$

where A_{WP} is the waterplane area calculated from Equation (3.20) for a semi-submersible WT with a circular waterplane area and diameter D.

$$A_{WP} = \frac{\pi D^2}{4} \tag{3.20}$$

The hydrostatic restoring stiffness in pitch can be calculated from Equation (3.21). It is used to calculate the mean pitch angle of the tower due to wind, which is a critical variable for a FOWT. This will be looked into in Section 5.3.1. The mooring system stiffness is neglected in this calculation since the influence of a spread mooring system on the linear wave-induced motion is generally quite small (Faltinsen 1990).

$$C_{55} = \rho g \nabla (z_B - z_G) + \rho g \iint\limits_{A_{WP}} x^2 dx dy = \rho g \nabla (z_B - z_G) + \rho g I_{WP} \tag{3.21}$$

In Equation (3.21), ∇ is the displaced volume of water, z_B and z_G are the overall center of buoyancy and center of gravity, respectively, and I_{WP} is the waterplane moment of inertia.

These restoring coefficients are only valid for infinitesimally small motions.

3.3.2 First-Order Effects

In linear theory, the first-order effects can be calculated assuming that the wave-induced motions and force amplitudes are linear proportional to the wave amplitude, which is a good assumption as long as the wave steepness is small and the wave amplitudes small relative to the body dimensions (Faltinsen 1990).

Another simplification made in linear analysis, is that the hydrodynamic problem

of a floating structure is separated into two parts; the diffraction problem and the radiation problem. From the diffraction problem, the wave excitation forces and moments are obtained by imposing incident waves on the body restrained from oscillating. The radiation problem, however, provides the added mass, damping and restoring terms on the body when it is forced to oscillate in all DOFs with the wave excitation frequency (Faltinsen 1990). The added mass and damping are proportional to the acceleration and the velocity of the forced motion, respectively, and are hence dependent on the wave frequency as opposed to the restoring terms. The damping in linear theory is only obtained from the generation of waves, since the fluid is assumed inviscid, and hence viscous drag is not taken into account.

The excitation loads obtained from the diffraction problem can be divided into two components; the Froude-Kriloff loads and the diffraction loads. The latter are due to the structure changing the wave pressure field, whereas the Froude-Kriloff loads are related to the loads acting on the structure from the undisturbed pressure field of the incident waves (Faltinsen 1990). In order to obtain this contribution, one has to integrate the incident wave dynamic pressure p along the mean wetted hull surface as in Equation (3.22) (Faltinsen 1990). In potential-flow theory, the Froude-Kriloff force $F_{FK,i}$ only depends on the incident-wave acceleration, i.e. not on the rigid-body acceleration.

$$F_{FK,i} = -\iint_S p n_i ds \tag{3.22}$$

In Equation (3.22), n_i are the unit vectors normal to the body surface according to the assumed coordinate system (n_1, n_2 and n_3, respectively), S is the wetted surface and s is the variable of integration.

3.3.3 Morison's Equation

Morison's equation is often used to calculate wave forces on slender cylindrical structures as an alternative to potential flow theories, as it accounts for viscous forces. Viscous forces are important for large wave heights and long waves.

Morison's equation is applicable for bodies with small diameter D compared to the wave length λ. A widely used limit for its applicability is $\lambda/5 > D$ (Faltinsen 1990). In this region, viscous forces matter. Morison's equation provides the horizontal force from an incident wave on an infinitesimal strip with length dz of a floating cylinder, as expressed in Equation (3.23),

$$dF_x = \underbrace{\rho\frac{\pi D^2}{4}(1+C_a)adz - \rho C_a\frac{\pi D^2}{4}\dot{v}dz}_{\text{Inertia forces}} + \underbrace{\frac{1}{2}\rho C_D D(u-v)|u-v|dz}_{\text{Drag forces}}, \tag{3.23}$$

where a and u are the horizontal wave particle acceleration and velocity, respectively, at the midpoint of the strip, and v is the horizontal body velocity at the midpoint of the strip. C_a is the added mass coefficient, and C_D is the drag coefficient.

The first term in Equation (3.23) represents the Froude-Krylov force, and the second term is the correction due to added mass from the movement of the cylinder in water. The last term contains the viscous drag forces. In order to obtain the 3D drag force, integration along the length of the body must be applied.

3.4 Servo Dynamics

The servo dynamics concerns the control of the WT in order to maximize power production for wind speeds below-rated wind speed, keep constant power and reduce loads for wind speeds above-rated wind speed, and in extreme conditions, shut down the WT. The rated wind speed is the wind speed at which the maximum output power of the generator is reached. The control system's job is also to alleviate the load on the drive-train and avoid enhancement of structural loads.

Large, modern wind turbines are predominantly operated using a strategy called "variable speed, variable pitch" (Bachynski-Polić n.d.). Variable speed, which means that the rotor can turn at different speeds, was enabled through the development of efficient and cheap power electronics, which allow for the efficient conversion of alternating-current (AC) electricity at one frequency, to direct current (DC), and then back to the necessary grid frequency (AC). Prior to this development, delivering AC power at the grid frequency required WTs to operate at a constant rotor speed. Aerodynamic efficiency across a wide range of wind speeds is remarkably higher for variable speed WTs.

With variable pitch, meaning that the blades' pitch angle can be actively controlled and varied, the aerodynamic loads can be more carefully controlled than the alternative, fixed pitch approach (Bachynski-Polić n.d.). A fixed pitch turbine would require the use of a mechanical brake or stall in order to reduce the rotor speed in high wind speeds. Stall-regulated designs tend to have lower aerodynamic efficiency across all wind speeds compared to variable pitch designs, providing significant advantages to the variable pitch approach.

Pitching of the blades is the most common method in order to vary the rotor speed. For below-rated wind speeds, the pitch angle is kept constant, whereas the generator torque varies in order to operate the WT as close to the optimal tip speed ratio as possible. Above-rated wind speed, the blades' pitch angle is varied in order to minimize the structural loads, which is one of the functionalities managed by the control system.

3.5 Eigenfrequency

Eigenfrequencies or natural frequencies are discrete frequencies at which an undamped system is prone to vibrate (Comsol 2018). When the system vibrates at a certain eigenfrequency, the structure will deform into a corresponding shape called the eigenmode. First mode, second mode and n^{th} mode represent the order in which least energy is required to deform the structure (midas Civil 2015).

The natural frequencies and mode shapes are functions of the structural properties (e.g. elastic modulus) and boundary conditions (University of Rochester 2022). Changing the structural properties of the structure only changes the natural frequency, whereas adjusting the boundary conditions also affect the mode shapes.

The determination of the eigenfrequencies of a structure is done through an eigenvalue analysis which will be discussed in Section 3.6. Such an analysis is important in order to ascertain that a periodic excitation does not cause resonance. Excitation sources on OWTs arise from the wind turbulence, the ocean waves, the rotational speed of the rotor (denoted by 1P), and the vibrations imposed by the blades passing the tower causing a shadowing effect (termed as 3P in case of three blades) (Alkhoury et al. 2021). The 1P frequency is a frequency range bounded by the lowest and highest speeds of the rotor. This is due to the fact that most modern industrial WTs are equipped with variable speed rotors.

3.6 Eigenvalue Analysis

An eigenvalue analysis determines the natural frequencies and corresponding mode shapes of a structure when damping is neglected and no external forces is acting (University of Rochester 2022). These results characterize the basic dynamic behavior of the structure and indicates how the structure will respond to dynamic loading.

In order to obtain the natural frequencies and mode shapes, a reduced form of the

equation of motion is used. If there is no damping and no load applied, the equation of motion in matrix form reduces to

$$\boldsymbol{M}\ddot{u} + \boldsymbol{K}u = 0, \tag{3.24}$$

where **M** is the mass matrix and **K** is the stiffness matrix. To solve Equation (3.24), a harmonic solution is assumed on the following form

$$u = \phi \, sin \, \omega_0 t, \tag{3.25}$$

where ϕ is the eigenvector or mode shape, ω_0 is the circular natural frequency, and t is the time variable. The number of eigenvalues and eigenvectors is equal to the number of DOFs that have mass, or the number of dynamic DOFs.

In the harmonic form of the solution, all the degrees of freedom of the vibrating body move synchronously, i.e. the structural configuration does not change its shape during the motion. Only the amplitude changes.

3.7 SIMO-RIFLEX-AeroDyn

The coupled code SIMO-RIFLEX-AeroDyn are calculation engines used in the software SIMA (DNV GL 2015). SIMA is a simulation program developed by MARINTEK, providing a graphical user interface to SIMO-RIFLEX-AeroDyn, as well as a post-processing tool.

The SIMO-RIFLEX-AeroDyn code takes advantage of the nonlinear beam element solver in RIFLEX (MARINTEK 2013), hydrodynamics models in the time domain simulation program SIMO for multi-body systems (MARINTEK 2012), and the aerodynamic force models in AeroDyn. SIMO-RIFLEX is developed by MARINTEK, and is the state-of-the-art tool for dynamic response analysis for moored offshore structures. SIMO-RIFLEX was extended with the AeroDyn code by Bachynski (E. Bachynski 2014) to form the SIMO-RIFLEX-AeroDyn code. This was in order to address the need for large volume hydrodynamics and second-order forces in FWT analysis. TurbSim is implemented in AeroDyn, which receives WT element positions, orientations and velocities from RIFLEX. In return, AeroDyn transfers the resulting aerodynamic forces on the blades and tower to RIFLEX. AeroDyn calculates the aerodynamic loads based on the BEM or GDW theory as discussed in Sections 3.1.1 and 3.1.2, respectively, and allows for the inclusion of turbulent wind.

In SIMO-RIFLEX-AeroDyn, the bar elements are described in a total Lagrangian formulation, meaning that the deformed properties in a new incremental configuration are referred to the initial configuration, which is used as reference. The beam theory applied assumes, in addition to the assumptions mentioned above, that a plane section of the beam initially normal to the x-axis remains plane and normal to the x-axis during deformation (SINTEF Ocean 2021). There are also several other assumptions applied, such as small strains, neglection of lateral contraction caused by axial elongation, and neglection of torsional warping resistance.

4 The Semi-Submersible Wind Turbine

4.1 The OO-Star Semi-Submersible Wind Turbine

The OO-Star semi-submersible floating substructure as seen in Figure 4.1 was designed by Dr.techn. Olav Olsen and was used as the base case in this work. It consists of three columns in a star shape with a centered column mounted on a three-legged pontoon in 130 m water depth. It is mostly built up by post-tensioned concrete. Catenary mooring lines are attached to the top of each of the three outer columns suspended with clump weights, providing station keeping. The rotor nacelle assembly (RNA) as well as the tower, which are also used in the modified concept studied in this work, have dimensions as listed in Table 4.1 taken from the LIFES50+ project (Müller et al. 2017).

4.2 The Tensegrity-Based Semi-Submersible Wind Turbine

The modified semi-submersible foundation is similarly studied in 130 m water depth, but instead of concrete, it is made of steel. The three catenary mooring lines are identical to the ones used in Dr.techn. Olav Olsen's design, except from being shorter, and are attached to the periphery of the circular heave plate mounted on the bottom of the centered column, at a depth of 40 m. The new foundation concept consist of six outer columns instead of three, forming the corners of a hexagon with an angle of 60° between them in the horizontal plane.

The pontoons have been replaced, and the outer columns are attached to each other and to the centered column through a tensegrity system as explained in Section 2.1. At the top and bottom of the outer columns, horizontal guy wires and beams are attached, forming two sets of "bicycle wheels" which are based on the same concept as was described in Section 2.2. The horizontal guy wires running from the outer columns placed radially around the centered column, to the centered column carrying the tower, act as the spokes, which similarly are given a pretension in order to remain in tension after applying a load. The beams connecting the outer columns to each other represents the rim.

From 11 m above the MSL and in the positive z-direction, the tower is identical to the DTU 10 MW WT. Below, the central column is prolonged with a constant diameter and thickness in the negative z-direction, reaching a draft of 40 m. Crushed stone is used as ballast in the bottom of the centered column to ensure stability.

The modified semi-submersible wind floater concept is depicted in Figure 4.2.

Figure 4.1: The OO-Star Wind Floater Semi-Submersible (Dr.techn. Olav Olsen AS 2021)

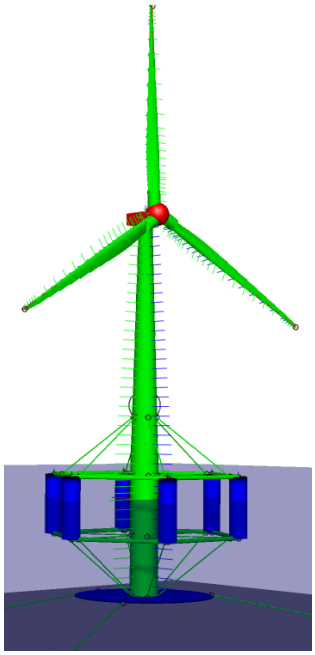

Figure 4.2: The modified semi-submersible concept, SIMA model

Table 4.1: Main parameters of the DTU 10 MW reference WT (Müller et al. 2017)

Parameter	**Value**
Tower base diameter [m]	11.385
Tower top diameter [m]	5.165
Tower elevation above MSL [m]	115.63
Wall thickness, base - top [m]	0.075-0.028
Hub height [m]	119
Tower mass [t]	1256
Nacelle mass [t]	444.5
Rotor mass [t]	230
Rated thrust force [kN]	1500

4.3 Explanation of Terms

Throughout the thesis, when referring to the tower, it is the part of the centered column from 11 m above the MSL and up to, not including, the RNA, whereas when referring to the centered column, it is the entire column, from 40 m below the MSL and up to, including, the RNA. The part of the centered column below the tower,

i.e. from 11 m above the MSL and in the negative z-direction, is considered a part of the foundation, including the mass of the ballast in the bottom part of the centered column, as well as the outer columns and the tensegrity system.

4.4 Operation of the Wind Turbine

It is the ”variable speed, variable pitch” strategy which is relevant in this work as discussed in Section 3.4. The wind speed in which the blades start rotating and generates power is called the cut-in wind speed (Energy 2022), which for the wind turbine in question is 4.0 m/s (Bak 2013). The rated wind speed is 11.4 m/s. This is the maximum operational condition. The cut-out wind speed is the speed at which the turbine shuts down to prevent unnecessary strain on the rotor, which for the DTU WT is at a wind speed of 25.0 m/s.

4.5 Tower

The DTU 10 MW reference WT is designed and approved to be connected to a fixed foundation. Its tower stiffness should therefore in theory be altered when mounted on a FWT foundation design as pointed out by the DNV standards (Det Norske Veritas 2013). Even when the mass and stiffness distributions over the height are kept the same as for the tower for an onshore wind turbine, the eigenfrequencies of the tower are changed when mounted on a floater due to a more flexible support. If it is desired to keep the eigenfrequencies of the tower unchanged, the tower would have to be made more flexible when supported by a floater. However, higher-order tower bending eigenfrequencies are coupled to the rotor loads, and if changed, may lead to undesirable vibrations. Hence, the issue in this context is whether or not the turbine fulfills its performance and safety requirements if the stiffness of the tower is altered, and will not be done in this work.

5 Semi-Submersible Wind Turbine Spreadsheet-Based Parametric Design

A design challenge with semi-submersible WTs is that they must have sufficient stability and structural strength, and at the same time have low cost of the produced power in order to be competitive. In this work, this is aimed achieved by reducing the amount of material used by applying a tensegrity system in order to connect the different elements of the foundation. Also, in order to avoid resonant rigid-body motions and structural vibrations excited by loads, natural periods and modes must be well designed. These considerations, along with other criteria such as restricting the maximum static pitch angle of the WT and obtaining equilibrium position of the entire system, will be studied in the following.

5.1 Foundation Definition

The modified foundation with the dimensions defined is depicted in Figure 5.1. These dimensions are a result of a parametric study, looking at the effect of changing them on the intact stability and natural periods. The dimensions were also chosen keeping in mind the goal of reducing the cost and environmental impact of the foundation.

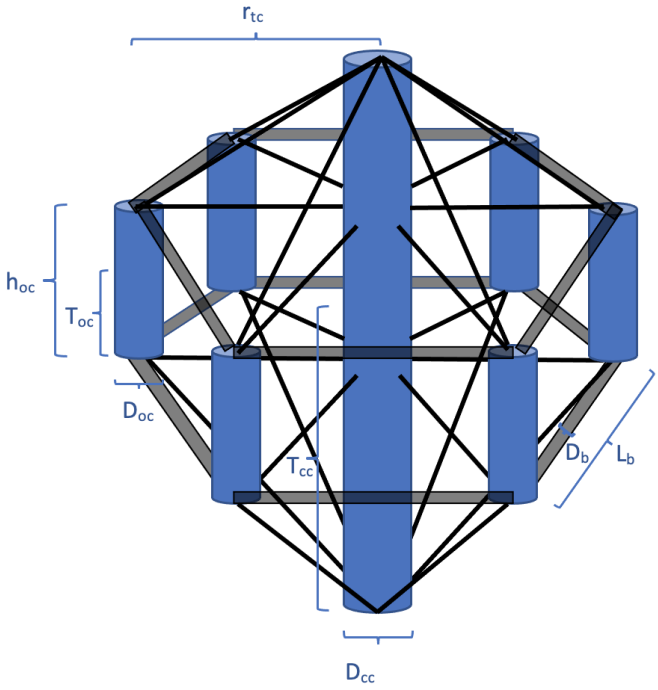

Figure 5.1: Parametric design definitions

The hull, made of steel, has in the initial design process the properties tabulated in Table 5.1. It has a material density $\rho_s = 7850$ kg/m^3, except from the centered column (excl. the RNA) which has a material density $\rho_{cc} = 7850 \cdot 1.05 = 8242.5$ kg/m^3, which is taken from the LIFES50+ project. The steel weight was found from these considerations, and the displacement was found from geometry considerations.

Table 5.1: Hull parameters

Parameter	**Value**
Young's modulus [N/m^2]	2.1E+11
Density [kg/m^3]	7850
Centered column density (excl. RNA) [kg/m^3]	8242.5
Allowable pretension stress [MPa]	300

The design space consist of six outer columns (oc), one central column (cc) that supports the DTU 10 MW reference WT, as well as a tensegrity system connecting the columns. The bottom diameter and thickness of the tower were applied on the 40 m prolonged section below the MSL, as well as on the first 11 m section above the MSL. The center to center (c/c) distance between the central column and the outer columns is denoted r_{tc}, which is identical to the distance between the center of each of the outer columns. Further, h_{oc}, T_{oc} and D_{oc} are the height, draft and diameter of the outer columns, respectively, and D_{cc} and T_{cc} are the diameter and draft, respectively, of the bottom part of the centered column. The structural details of the connections between the beams and guy wires to the columns were not investigated in this work.

In total, the tensegrity system consist of 24 guy wires in tension colored black in Figure 5.1, and 12 beams in compression colored grey in the same figure, having diameter D_b and length L_b.

Based on these parameters, the first calculations of the semi-submersible WT behaviour could be obtained by simple computations in a spreadsheet, applying engineering assumptions and physical relations. This will be studied in the following.

5.2 Design Parameters

The following sections will describe the main dimensions of the modified foundation, and which parameters that are varied in the parametric study. Also, general assumptions about the design will be presented.

The hull, which is based on the concept developed by Dr.techn. Olav Olsen, was parameterized by defining the following dimensions: 1) the draft of the centered column, T_{cc}, and the outer columns, T_{oc}, 2) the diameter of the outer columns, D_{oc}, 3) the distance between the columns, r_{tc}, and 4) the number of outer columns, n_{oc}.

5.2.1 Wind Turbine

The DTU 10 MW reference WT was used in this study, although the tower for a floater should be different from that for a fixed support as discussed in Section 4.5. The length of the tower is 104.63 m, and it is divided into sections, each having constant thickness, but with linearly varying diameter, see Appendix A. The outer diameter and wall thickness decreases with increasing height on the tower, with (5.165, 0.028 m) and (11.385, 0.075 m) at the top and bottom of the tower, respectively. The bottom dimensions of the tower has been used as the constant dimensions for the extended column, reaching a draft of 40 m. Increasing the draft give better stability as the ballast can be placed at a lower z-coordinate, lowering the vertical center of gravity (COG), which was done for the present concept.

5.2.2 Outer Columns

The six outer columns are identical and described by their diameter D_{oc}, freeboard and draft T_{oc}. Their diameter influence the waterplane area and waterplane moment of inertia as well as their steel weight, as does their height h_{oc}, changing the expenses of producing the structure. Their dimensions will be found in Section 5.4.

5.2.3 Distance between the Outer Columns and the Tower

Increasing the distance between the outer columns and the tower r_{tc} gives higher restoring coefficients in pitch and roll which could be necessary in order to satisfy the maximum static pitch angle requirement discussed in Section 5.3.1. A disadvantage of an increased distance is that the members connecting them become longer, possibly increasing their dimensions and exposure to fatigue damage. As the distance increases, also the assumption of rigid body motions become less valid, as well as having to increase the diameters and thicknesses of the connecting beams and guy wires. Increasing the outer dimensions also reduces the number of suitable sites and could increase the cost of construction and transportation to the operation site.

5.2.4 Tensegrity Components

The beams and guy wires connecting the outer columns to the centered column, as well as connecting the outer columns to each other, make up the tensegrity system. Both the beams and guy wires are characterized by their Young's modulus E, cross-sectional area, stressfree length L_0, dry mass per length and outer diameter.

The dimensions of the members in tension were found by considering the weight of the centered column, which includes the weight of the RNA and ballast. The angle between the angled guy wires and the centered column was found by trigonometric considerations, resulting in an angle of 50.9°. Then, by considering the weight of the centered column, the force in the guy wires could be found, resulting in $F_w = 4.29$ MN per wire. This force applies to the angled wires below the MSL, but as a simplification, was also used in order to find the diameter of the remaining wires. However, these could have had smaller dimension as they carry less load. The diameter, which hence was applied on all the tensional members in the tensegrity system, could be found according to the following equation:

$$D_w = 2 \cdot \sqrt{\frac{F_w}{\sigma_a \pi}}, \tag{5.1}$$

where $\sigma_a = 300$ MPa is an assumed allowable stress.

The dimensions of the compressive beams, however, were found by checking against buckling, using the DNV Design Codes and Standards. The buckling strength could be verified with the DNV recommended practice *Buckling Strength of Shells* (DNV 2013). Amplification of stresses due to dynamic structural responses must be taken into account in the ultimate strength evaluation. The non-linear amplification factor α is calculated according to Equation (5.2), where P_E is the Euler load calculated from Equation (5.3), and P is the compressive force acting on the beam. In order to calculate the Euler load, the length of the beam L_b must be known, as well as the bending stiffness EI found by multiplying the Young's modulus with the beam moment of inertia I, calculated from Equation (5.4) for a hollow circular cylinder with outer diameter D_b and thickness t_b. The thickness was assumed to be $D_b/70$ after guidance with the supervisors. The diameter of the beams could be found based on these equations, and it was verified that such large-diameter pipes exist on the market.

$$\alpha = \frac{1}{(1 - \frac{P}{P_E})} \tag{5.2}$$

$$P_E = \frac{\pi^2 EI}{L_b^2} \tag{5.3}$$

$$I = \frac{\pi}{64}(D_b^4 - (D_b - 2t_b)^4) \tag{5.4}$$

The horizontal c/c distance between the outer columns and the central column is the same as the c/c distance between the outer columns, and hence the length of the beam elements. This distance is 40 m, and will be found in Section 5.3.1. However, the connections of the guy wires were placed on the peripheries of the columns, resulting in a length of 30.808 m for the horizontal guy wires. The length of the angled guy wires running between the top of the outer columns to 34.271 m above the MSL on the tower, and from the bottom of the outer columns to the bottom of the centered column, are all 39.675 m long. Their connections were similarly placed on the peripheries of the columns.

For the beam elements, also the torsional stiffness must be found according to Equation (5.5), with the shear modulus given by Equation (5.6), where $\nu = 0.3$ is the Poisson's ratio.

$$T = G \cdot 2I \tag{5.5}$$

$$G = \frac{E}{2(1+\nu)} \tag{5.6}$$

The resulting dimensions of the members in the tensegrity system are summarized in Tables 5.2 and 5.3.

Table 5.2: Properties of the beams in the tensegrity system

Parameter	**Value**
Length [m]	40
Diameter [m]	1.4
Thickness [m]	0.02
Cross-sectional area [m^2]	0.0867
Axial stiffness [MN]	18 209
Bending stiffness [MNm^2]	4335
Torsional stiffness [MNm^2/rad]	3335

Table 5.3: Properties of the guy wires in the tensegrity system

Parameter	**Value**
Length angled guy wires [m]	39.675
Length horizontal guy wires [m]	30.808
Diameter [m]	0.1349
Cross-sectional area [m^2]	0.0143
Axial stiffness [MN]	3000

5.3 Design Criteria

In order to find a realistic design from the spreadsheet calculations, some design criteria must be defined. One of the main goals of this thesis was to reduce the applied material as much as possible, making the semi-submersible concept as economically and environmentally beneficial as possible. This is achieved when the power production is maximized, and the construction, installation and operational costs are minimized. An assessment of the costs will however not be conducted in this work.

Having these goals in mind, the criteria listed in the following were used at the spreadsheet design stage.

5.3.1 Hydrostatic Consideration

The mean pitch angle of the tower cannot exceed a certain level. In order to calculate it, the hydrostatic stiffness in pitch C_{55} must be known. It is dependent on the center of gravity, the center of buoyancy and the waterplane moment of inertia as calculated from Equation (3.21). For the present foundation concept, the mean pitch angle is mainly restricted by having a large waterplane moment of inertia I_{WP}, which is typical for semi-submersible foundations. It is calculated according to Equation (5.7) for the construction considered in this thesis, which has a circular waterplane area. The parallel axis theorem was applied for the buoyancy elements placed radially out from the centered column carrying the WT.

By varying the diameter of the outer columns D_{oc}, the number of outer columns n_{oc}, and the distance between the outer and centered column r_{tc}, the necessary waterplane moment of inertia could be found, as well as the necessary diameter, number of outer columns and distance, in order to limit the pitch angle, calculated from Equation (5.8). Both the parameters for calculating these values as well as their results are summarized in Tables 5.4 and 5.5.

$$I_{WP} = \frac{\pi D_{cc}^4}{64} + n_{oc}(\frac{\pi D_{oc}^4}{64} + \frac{\pi D_{oc}^2}{4} r_{tc}^2) \tag{5.7}$$

$$\eta_5 = \frac{F_{T,rated} \cdot H_{MSL}}{C_{55}} \cdot \frac{180^\circ}{\pi} \tag{5.8}$$

The numerator in Equation (5.8) represents the mean wind turbine thrust overturning moment which causes the static pitch angle. An inclining WT reduces the projected area of the WT blades and thereby decreases their effect. Also, large pitch motions result in large gravitational forces which is neither convenient. Hence, it was desired to keep the static pitch angle at a minimum, and maximum 6° after guidance with the supervisors. The mooring system stiffness was neglected in the calculation of the mean pitch angle, and small inclination angles and minimal coupling with surge is assumed.

In Section 3.3.1, also the equation for heave hydrostatic stiffness was presented, and the input parameters and result for its calculation are found in Table 5.4. For the foundation concept having a circular waterplane area, the hydrostatic stiffness in roll and pitch are the same. The hydrostatic stiffness in surge, sway and yaw were derived from the mooring system.

Table 5.4: Input parameters and results for calculating the body hydrostatic stiffness

Seawater density [kg/m^3]	ρ	1025
Gravitational acceleration [m/s^2]	g	9.81
Displaced volume [m^3]	∇	7905
Vertical center of buoyancy [m]	z_B	-14.3
Vertical center of gravity [m]	z_G	4.2
Centered column bottom diameter [m]	D_{cc}	11.385
Number of outer columns [-]	n_{oc}	6
Outer column diameter [m]	D_{oc}	7
C/c distance centered to outer columns [m]	r_{tc}	40
Waterplane area [m^2]	A_{WP}	332.7
Waterplane moment of inertia [m^4]	I_{WP}	370 983
Heave hydrostatic stiffness [MN/m]	C_{33}	3.35
Pitch/roll hydrostatic stiffness [MNm/rad]	C_{55}	2262

Table 5.5: Input parameters and result for calculating the mean pitch angle

Rated thrust force [kN]	$F_{T,rated}$	1500
Hub height above MSL [m]	H_{MSL}	119
Mean pitch angle [degrees]	η_5	4.52

5.3.2 Hydrodynamic Consideration

It is desired to keep the natural periods of the FWT outside the wave energy range. This range depends on the site location and weather, but typically, waves contain most energy within 5 to 20 s. For a semi-submersible platform, it is the heave natural period which typically lies within the wave energy range, and will be the most critical to assess. The heave natural period was calculated from Equation (5.9), assuming a rigid body and neglecting the mooring system stiffness. The restoring force associated with the heave motion is due to the change in displaced volume. In this design, it was not possible to keep the modified concept outside the wave energy range without the use of a heave plate. Without a heave plate, the heave natural period was calculated to be 10.32 s, which is in the middle of the wave spectrum.

$$T_{n3} = 2\pi\sqrt{\frac{M + A_{33}}{C_{33}}} \tag{5.9}$$

The input parameters and result from the calculation of Equation (5.9) are summarized in Table 5.6. The heave plate size was adjusted to find the necessary added mass, obtaining the desired heave period outside the wave energy range. The heave added mass will be calculated in Section 5.6.

Table 5.6: Input parameters and result for calculating the heave natural period

Heave plate diameter [m]	D_{hp}	43.7
Total mass [kg]	M	8.1E+06
Heave added mass [kg]	A_{33}	28E+06
Heave hydrostatic stiffness [MN/m]	C_{33}	3.35
Heave natural period [s]	T_{n3}	20.65

Further, it is critical to keep the rigid body natural periods away from the excitation periods of the WT. This will be discussed in the following.

5.3.3 The 1P and 3P Frequencies of the Wind Turbine

For wind turbines, the rotational frequency 1P and blade passing frequency 3P are important characteristic frequencies as mentioned in Section 3.5. The coupling of the 1P and 3P frequencies with natural frequencies of the entire system should be avoided. Table 5.7 show that the 1P and 3P frequencies of the DTU WT are less than 10 s, which is well out of the range of all the natural frequencies of the semi-submersible WT considered in this work, which will be found in Section 6.8. Hence, coupling of the motion of the whole system with the rotation of the blades will not be of any concern.

Table 5.7: The 1P and 3P frequencies of the DTU 10 MW WT

Frequency	**Minimum**	**Maximum**
Rotational frequency	6 rpm	9.6 rpm
1P	6.25 s	10.0 s
3P	2.08 s	3.33 s

5.3.4 Other Criteria

There are also other criteria besides the ones listed above that are desired to fulfill:

- Minimize the hull weight in order to reduce the material cost.
- Minimize fatigue damage and thereby maximize the WT's lifetime.
- Keep outer dimensions at a reasonable size such that the platform can be constructed at most shipyards.
- Keep the draft relatively low to maintain one of the main advantages with semi-submersible foundations. In such case, the WT can be towed in shallow waters and mounted at most quaysides.

5.4 Dimensions of the Outer Columns

In order to calculate the thickness of the outer columns, a design assumption as defined in Equation (5.10) was made after guidance with the supervisors. It states that the total steel weight of the hull is 25% of the mass displacement. This is a conservative estimate which was used as a starting point.

$$M_s = 0.25\rho\nabla \tag{5.10}$$

The thickness of the outer columns could then be found using Equation (5.11), which is based on the design assumption in Equation (5.10), where ρ is the sea water density and ρ_s is the material density.

$$t_{oc} = \frac{\rho D_{oc} h_{oc}}{8 \cdot \rho_s (D_{oc} + 2h_{oc})} \tag{5.11}$$

Table 5.8 summarizes the dimensions of the outer columns. They have a constant diameter of 7 m which was found considering the mean pitch angle of the tower as discussed in Section 5.3.1.

Table 5.8: Main dimensions of one outer column

Diameter [m]	D_{oc}	7
Thickness [m]	t_{oc}	0.05
Height [m]	h_{oc}	25
Draft [m]	T_{oc}	15
Steel mass [t]	M_{oc}	214.7
Displacement [m^3]	∇_{oc}	577.3
Center of buoyancy [m]	$z_{B,oc}$	-7.5
Center of gravity [m]	$z_{G,oc}$	-2.5

5.5 Ballast Weight

The centered column was filled with ballast in order to achieve equilibrium between the buoyancy force and the total mass. The necessary ballast weight was calculated from Equation (5.12), with the input parameters and resulting weight summarized in Table 5.9. The values given in the table includes the total mass of each input. The ballast was placed at the bottom of the centered column in order to lower the center of gravity, obtaining better stability. No ballast was considered in the outer columns.

Permanent crushed stone was used as ballast material as it is cheap and has a large mass per volume of 2500 kg/m^3, covering a height of 10.84 m of the bottom part of the tower.

$$M_{ballast} = \rho\nabla - M_{oc} - M_{cc} - M_b - M_w - M_{ml} \tag{5.12}$$

Table 5.9: Input parameters and result for calculating the ballast mass (the values are the total mass of each input)

Displacement [m^3]	∇	7905
Outer column mass [kg]	M_{oc}	1.29E+06
Centered column mass [kg]	M_{cc}	3.05E+06
Beam mass [kg]	M_b	3.27E+05
Guy wire mass [kg]	M_w	9.5E+04
Mooring line mass [kg]	M_{ml}	6.60E+05
Resulting ballast mass [kg]	$M_{ballast}$	2.69E+06

5.6 Calculation of Added Mass

The total added mass in heave was calculated using Equation (5.13). The added mass includes contribution from the six outer columns, the six beams in compression below the MSL, as well as the added mass from the heave plate attached to the center column $A_{33,hp}$, as found from Equation (2.14). The heave added mass for the outer columns is approximated as the added mass of a sphere with diameter D_{oc}. The interaction between the components is neglected in this calculation.

$$A_{33} \approx \frac{\pi}{12} \cdot \rho \cdot n_{oc} \cdot D_{oc}^3 + \rho\pi L_b \cdot \frac{D_b^2}{4} \cdot n_b + A_{33,hp} \tag{5.13}$$

The total added mass in surge is given by Equation (5.14), where T_{cc} is the draft of the centered column and T_{oc} is the draft of the outer columns.

$$A_{11} = \frac{\rho\pi}{4}(T_{cc}D_{cc}^2 + n_{oc}T_{oc}D_{oc}^2 + n_b D_b^2 \frac{L_b}{2}) \tag{5.14}$$

The input parameters for calculating the added masses in Equations (5.13) and (5.14) are summarized in Table 5.10 along with the resulting masses.

Table 5.10: Input parameters and results for calculating the added masses

Seawater density [kg/m^3]	ρ	1025
Number of outer columns [-]	n_{oc}	6
Outer column diameter [m]	D_{oc}	7
Outer column draft [m]	T_{oc}	15
Beam length [m]	L_b	40
Beam diameter [m]	D_b	1.4
Number of beams below MSL [-]	n_b	6
Centered column draft [m]	T_{cc}	40
Centered column bottom diameter [m]	D_{cc}	11.385
Heave plate diameter [m]	D_{hp}	43.7
Heave plate added mass [kg]	$A_{33,hp}$	2.71E+07
Surge added mass [kg]	A_{11}	7.91E+06
Heave added mass [kg]	A_{33}	2.80E+07

5.7 Comparison between the Resulting Foundation Design and the OO-Star Foundation

The main properties of the reference substructure are listed in Table 5.11 along with the properties of the modified concept (Pegalajar-Jurado et al. 2018). The substructure of the new concept includes the six outer columns, the 12 beams in compression, the 24 guy wires in tension as well as the centered column from 11 m above the MSL and down to 40 m depth, including the ballast weight.

Table 5.11: Comparing the properties of the two concepts' substructure

	Mooring length	Draft	Freeboard	Tot.displ.volume	Mass (excl.mooring)
OO-Star	703 m	22 m	11 m	23 509 m^3	21 709 t
New concept	455 m	40 m	11 m	7905 m^3	7443 t

From Table 5.11, it is seen that a mass reduction of 65.7% is achieved with the new foundation concept compared with the foundation of the OO-Star concept. It is also seen that the mooring line length of the modified concept has been shortened, which is due to moving the connection between the mooring lines and the hull from the top of the outer columns in the reference concept, to the bottom of the tower at a draft of 40 m in the modified concept.

The results also show that the new concept has almost twice as large draft as

the reference concept from OO-Star. This is normally not desired for a semi-submersible foundation concept, as a low draft is one of the great advantages with semi-submersible foundations.

Compared to the SpiderFLOAT concept mentioned in Section 2.3, the resulting design is 43% heavier, and has a 5 m larger radius. However, it is difficult to see how the SpiderFLOAT concept deals with the lack of shaft yaw stiffness, which may introduce undesirable dynamic behaviour.

6 Modelling in SIMA

The computations and modelling of the modified WT concept presented in this thesis have been performed using the coupled code SIMO-RIFLEX-AeroDyn, and was used to look at the behaviour of the structure and to verify the spreadsheet calculations. Time domain coupled dynamic analysis has been performed and run in 130 m water depth, with an external controller written in Java for the DTU 10 MW WT. This controller is developed for a bottom-fixed WT, which may cause challenges with regards to negative damping in pitch when applied to a FWT.

Being a complicated structure containing many different components, the modelling process was time-consuming. The schematic representation of the nodes in the SIMA model is represented in Appendix F. However, the model was successfully built, and the spreadsheet calculations could be verified against the results provided by SIMO-RIFLEX-AeroDyn. This was an important verification in order to have a believable concept. The procedure will be presented in the following sections. SIMA version 4.2.0 for Windows is used for the analyses.

6.1 Coordinate System

The global coordinate system is set according to the Germanischer Lloyd standard (Germanischer Lloyd 2012), having its origin at the still water level in equilibrium position without any external forces acting. The x-axis is pointing in the downwind direction, and the z-axis points vertically upwards along the centered column as shown in Figures 6.1 and 6.2. The rotations around the axes are defined positive by the right-hand rule.

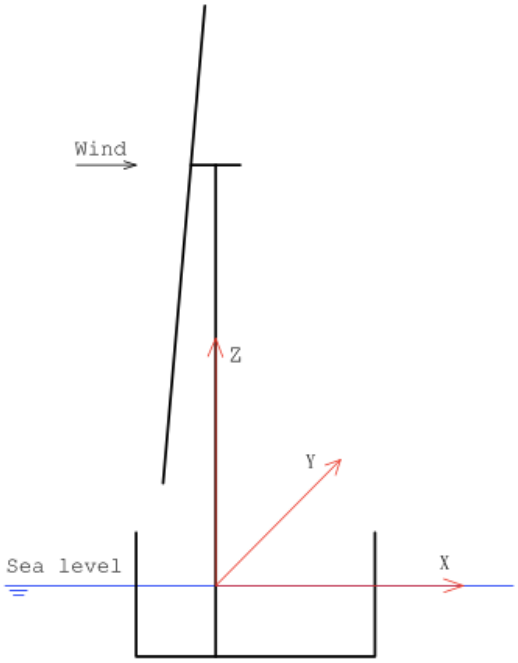

Figure 6.1: Coordinate system, side-view

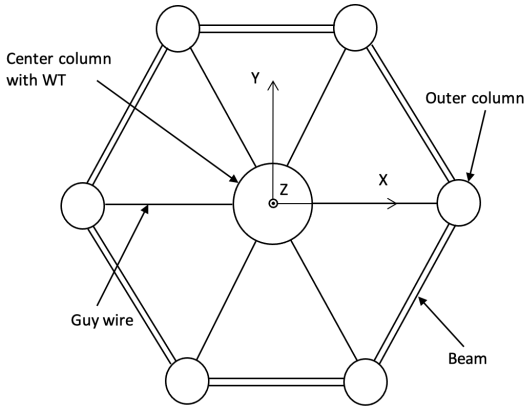

Figure 6.2: Coordinate system, top-view

6.2 Units

The SI units have been used throughout this work, as defined in Table 6.1.

Table 6.1: Units

Parameter	**SI unit**
Length	m
Time	s
Mass	kg
Force	N
Stress	Pa (N/m^2)

6.3 Time Integration Parameters

The simulations conducted in SIMO-RIFLEX-AeroDyn were performed with the integration parameters presented in Table 6.2. Applying these parameters will maintain an unconditionally stable integration method while introducing a small amount of algorithmic damping, as was discussed in Section 3.2.4.3. However, a slight reduction in accuracy occurs.

Table 6.2: Newmark-Beta integration parameters applied in SIMO-RIFLEX-AeroDyn simulations

$\triangle$t	0.1 s
γ	0.505
β_{nb}	0.2525

6.4 Wave and Wind Modelling

The waves were modelled as unidirectional wind waves calculated from wave spectra. The JONSWAP-3 parameter spectrum was used, as described in Section 2.5.2. The wind was modelled as stationary uniform, only having a horizontal velocity component.

For the ULS analyses however, the TurbSim program from NREL was used to generate the turbulence box as explained in Section 2.4.2, and a fluctuating three component wind was used. An example of a TurbSim input-file is attached in Appendix C.

The Airy linear wave theory was used for the wave calculation method. Unidirectional wave spectra are thought of as a sum of a large number of regular waves at different frequencies as was discussed in Section 2.5. The wave theory gives a linearised description of the propagation of gravity waves, and is based on the assumption that the fluid flow is inviscid, incompressible and irrotational.

The wave model is somewhat simplistic as it does not take wave breaking into account nor second order wave effects. In this study, wave breaking is not likely to occur as the wind turbine is located in deep water, even though it may occur due to the foundation geometry. Second order wave forces may occur, which represents a weakness in the model, but are however less in magnitude compared to first order wave forces (Joseph et al. 2014). Second order wave effects are caused by differential wave elevation around the body and the quadratic velocity component of water particles.

6.5 Modelling of the Extended Centered Column

From 11 m above the MSL, the shaft of the DTU reference WT was extended, reaching a depth of T_{cc} = 40 m. The whole centered column was modelled as RIFLEX elements. For long cylinders in infinite fluid, the added mass coefficient in normal direction can be approximated as 1.0 [-] (DNV GL 2017). In tangential

direction, the added mass coefficient C_a was found by using the hydrodynamic mass force from Morison's equation for a circular cylinder:

$$F_x = \frac{\pi}{4}\rho D_{cc}^2 a_x C_a T_{cc}, \tag{6.1}$$

where a_x is the flow acceleration and D_{cc} and T_{cc} are the diameter and draft of the centered column, respectively.

Setting Equation (6.1) equal to the equation for added mass in heave

$$A_{33} = \frac{\pi}{12} D_{cc}^3 \rho a_x, \tag{6.2}$$

the following expression is found for the added mass coefficient in tangential direction:

$$C_a = \frac{1}{3}\frac{D_{cc}}{T_{cc}}. \tag{6.3}$$

This resulted in an added mass coefficient in tangential direction of 0.0949 [-].

The drag coefficients were set to 1.0 [-] in normal direction, and in tangential direction, the drag will be small, and was as a first estimate set to 0.05 [-] after guidance with the supervisors.

6.6 Modelling of the Outer Columns

The outer columns were modelled as SIMO bodies, with the option 'apply gravity force' included in SIMA. This means that SIMO does not include the buoyancy of the body. Instead, the buoyancy is included by defining slender elements having the same volume as the bodies, and include gravity and buoyancy on these. The forces acting on the slender elements are calculated with Morison's equation. They were assigned a specific volume and mass, in addition to an added mass and drag which will be found below. The Froude-Kriloff forces has to be accounted for in the model due to the slender elements defined. SIMO-RIFLEX-AeroDyn calculates the Froude-Kriloff force based on the given volume of the body.

The outer columns' heave added mass are approximated as the added mass of a sphere, calculated as

$$A_{33,oc} = \frac{\rho}{12 \cdot T_{oc}} \pi D_{oc}^3. \tag{6.4}$$

Since the input into SIMO-RIFLEX-AeroDyn is the added mass in kg/m, the added mass was divided by the draft of the outer columns. Similar was done for the surge and sway added masses, which was also included in the SIMO-RIFLEX-AeroDyn model, calculated by

$$A_{11,oc} = A_{22,oc} = \frac{\rho}{4 \cdot T_{oc}} \pi D_{oc}^2 T_{oc}. \tag{6.5}$$

The results, given for one outer column, are summarized in Table 6.3.

Table 6.3: Outer column added mass

Parameter	**Value**
Heave added mass [kg/m]	6136
Surge and sway added mass [kg/m]	39 447

The drag force term for the outer columns in heave direction was found using the following equation:

$$C_{D,3} = \frac{1}{2T_{oc}} \rho A_{oc}, \tag{6.6}$$

where A_{oc} is the cross-sectional area of the outer columns.

In surge and sway direction, the drag term was found by the drag force term in Morison's equation:

$$F = \frac{1}{2} \rho C_D D_{oc}, \tag{6.7}$$

where C_D is set to 1.0 [-]. The resulting drag terms are summarized in Table 6.4.

Table 6.4: Outer column drag

Parameter	**Value**
Drag in heave [Ns^2/m^3]	1314.89
Drag in surge and sway [Ns^2/m^3]	3587.50

6.7 Modelling of the Beams and Guy Wires

The members in tension and compression attaching the outer columns to each other and to the centered column are depicted in Figure 5.1, and their properties are given in Tables 5.2 and 5.3.

The members in compression above and below water were modelled differently in SIMA. The members above water were modelled as bar elements, whereas the ones below water were modelled as beam elements. The only stiffness property inserted for bar elements into SIMO-RIFLEX-AeroDyn, is the axial stiffness. For beam elements, also the torsional and bending stiffnesses are specified. As all the beams have the same dimensions, their properties are equal. For the beams below water, an added mass coefficient of 1.0 [-] was inserted into SIMO-RIFLEX-AeroDyn.

The guy wires were given a pretension which provides geometric stiffness, and in turn restricts yaw motion of the foundation. The yaw motion is important to limit as the increased tension in the mooring lines due to large yaw motions might impose a design condition (Gao 2022). However, since it is common to assume that the wind direction does not change, the yaw motions are considered small. The small yaw motions are mainly due to aerodynamic yaw moments, and could also be induced by hydrodynamic yaw moments for non-axial-symmetrical floaters.

The stressfree lengths L_0 and corresponding pretension F of the guy wires are as indicated in Table 6.5. The pretension is found by

$$F = \frac{EA(L - L_0)}{L_0}, \tag{6.8}$$

where A and L are the cross-sectional area and length of the guy wires, respectively.

Table 6.5: Stressfree lengths and pretension of the guy wires

Part of tensegrity system	**Length [m]**	**Stressfree length [m]**	**Pretension [MN]**
Angled wires	39.675	39.500	13.29
Horizontal wires above water	30.808	30.750	5.66
Horizontal wires below water	30.808	30.738	6.83

The tabulated stressfree lengths and corresponding pretensions in Table 6.5 are the ones used in the base load cases presented in Section 7.2.

6.8 Free Decay Test

Decay tests were performed in order to estimate the natural frequencies of the system in a given mode of motion, i.e. surge, sway, heave, roll, pitch or yaw (E. Bachynski 2021). In the SIMO-RIFLEX-AeroDyn analyses, a consistent mass formulation, as explained in Section 3.2.4.1, was employed in order to give better accuracy. The use of a consistent mass formulation implies that computed natural frequencies are an upper bound on the exact natural frequencies of the model (Cook et al. 2002).

A force was applied to the system in order to displace it by a given amount, then released. The force was applied in the COG in order to limit the coupling between motions. In such case, the resulting motion in the DOF of interest can be described as

$$m\ddot{x} + b(\dot{x})\dot{x} + k(x)x = 0, \tag{6.9}$$

where x is the displacement, m is the mass including the added mass, $b(x)$ represents a damping function, and $k(x)$ represents a stiffness function. This equation assumes that no external excitation forces are acting. Hence, it is the time period after the force has been released which is of interest.

The eigenvalue analyses were mainly conducted in order to check the heave natural period and ensure that it laid outside the wave period in order to avoid resonance. Before the heave plate was added, the period laid in the middle of the wave period. The heave plate was dimensioned to increase the natural period, reaching a minimum of 20 s.

During the decay tests, the wind turbine is parked and the blades are feathered. The tests are carried out in calm water ($H_s = 0.01$ m, $T_p = 20$ s and U = 0.01 m/s). The results are shown in Figure 6.3 and the natural periods are summarized in Table 6.6. The decay tests are plotted from the time in which the force applied is deactivated, and hence the time period of interest for calculating the natural periods.

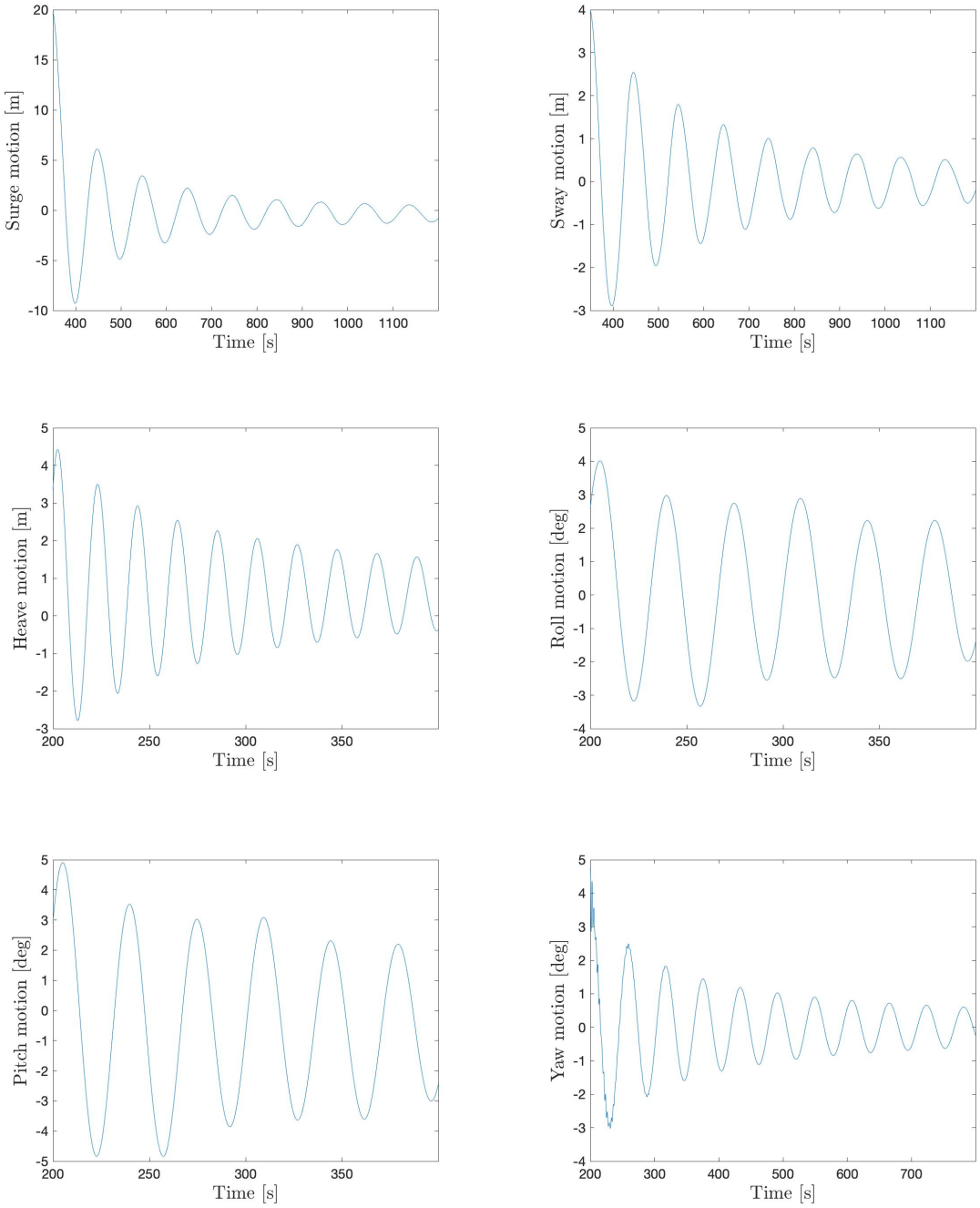

Figure 6.3: Free decay test of six DOFs

Table 6.6: Natural periods of the platform in six DOFs

Degree of freedom	**Natural period** [s]
Surge/sway	98.6
Heave	20.8
Pitch/roll	34.7
Yaw	57.9

It should be mentioned that due to coupling of different DOFs (surge-pitch and sway-roll in particular), the platform will always move in other DOFs than the one studied when performing free decay tests. For the surge free decay test, the largest amplitude in pitch was around 1.5 degrees, while for the pitch free decay test, the largest amplitude in surge was around 2 m. Similar results were found for the sway and roll decay tests. These values are small compared to the value of the motion in the degree of freedom being tested, and the results are therefore considered reasonable accurate.

The heave natural period from the decay test was found to be 20.8 s, which is close to the value found in the preliminary design process (20.65 s) in Section 5.3.2. This indicates that the mooring system has limited restoring contribution in the heave DOF, as the mooring system was only included when finding the natural period in the decay test.

6.9 Modelling of the Heave Plate

For the WT foundation concept in question, a heave plate was necessary in order to remove the heave natural period of the structure away from the wave energy spectrum. The circular heave plate is attached to the bottom of the centered column, at 40 m water depth. A large ratio between the disc depth and the disc radius implies that the flow hardly will be influenced by the free surface as was discussed in Section 2.8. This is the case for the current model, having a ratio of $40/21.85 = 1.83$, and free surface effects can hence be neglected. The heave plate is modelled as a slender element and given the parameters tabulated in Table 6.7. The thickness of the plate was set to 0.05 m, taken from the doctoral thesis by Kvittem (2014), and the mass was found to be 11.78E+06 kg/m, given per thickness of the heave plate. However, the mass was not included in the calculations and analyses conducted in this work.

Table 6.7: Heave plate parameters

Parameter	**Value**
Diameter [m]	43.70
Thickness [m]	0.05
Mass [kg/m]	11.78E+06
Area [m^2]	1500
Added mass [kg/m]	5.42E+08
Drag [Ns^2/m^3]	14.3E+06

The added mass of the heave plate was calculated according to Equation (2.14), resulting in a value of 5.42E+08 kg/m, given per thickness of the heave plate.

In order to calculate the drag force induced by the heave plate, SIMO-RIFLEX-AeroDyn applies the following equation,

$$F_d = C_D L v^2, \tag{6.10}$$

where C_D is the drag coefficient, L is the thickness of the heave plate and v^2 is the speed of the heave plate relative to the fluid it is submerged in. The quadratic drag coefficient was inserted into SIMO-RIFLEX-AeroDyn, calculated from Equation (6.6). The area inserted into the equation is the heave plate's area minus the area of the centered column which it is attached to, and the draft T is the thickness of the heave plate. This resulted in a drag of 14.3E+06 $\mathrm{Ns^2/m^3}$.

In order to find the right size of the heave plate, obtaining the desired heave natural frequency outside the wave energy spectrum, spreadsheet-based calculations were conducted, as well as an eigenvalue analysis in SIMO-RIFLEX-AeroDyn in order to verify the hand calculations as explained in Section 6.8. The resulting size of the heave plate in order to achieve this was a cross-sectional area of 1500 $\mathrm{m^2}$. With such a large plate, an alternative solution to attache it to the bottom of the centered column, is to attach a cover to the lower "bicycle wheel". In SIMO-RIFLEX-AeroDyn however, the plate was modelled as a slender element attached to the bottom of the centered column.

In this work, a plain disc configuration without any structural reinforcements has been analysed as the heave plate which is relevant for numerical model calibration. However, from a structural point of view, a plain disc configuration is not feasible in a practical application. In practice, the disc has to be radially and circularly reinforced (Lopez-Pavon and Souto-Iglesias 2015). These reinforcements may alter the heave plate's hydrodynamic performance, but is not studied any further in this work.

With such a large heave plate, it must withstand a large added mass, in addition to having the mooring lines connected to it. It can hence be challenging to produce. Even though the concept studied in this thesis is of light weight compared to many other FWT foundation concepts, it must be possible to produce. Hence, the heave plate configuration used in this work may not be the best solution, nor even realistic, but has not been assessed in further detail.

6.10 Modelling of the Mooring Lines

A spread mooring system is composed of a floating body having its motions restricted by a set of anchor lines (Faltinsen 1990). The total stiffness of the mooring lines is composed of two contributions: geometric stiffness and elastic stiffness. The geometric stiffness is provided by the weight of the line, the pretension of the line, the length of the line and the buoy weights. The elastic stiffness is due to the line axial elongation. Since catenary chain is used for the spread mooring system in this work, geometric stiffness will dominate as catenary chain has minimal elasticity.

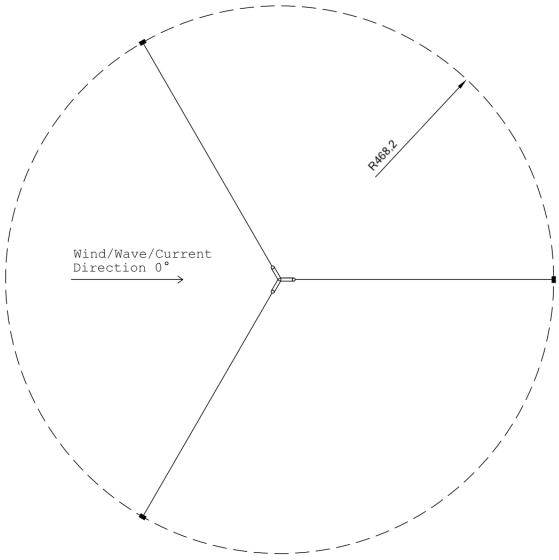

Figure 6.4: Mooring line system configuration (topview)

The mooring system of the structure is composed of three mooring lines which are all modelled similarly and attached to the heave plate mounted on the bottom of the centered column. The configuration is depicted in Figure 6.4. The anchor lines are pretensioned and modelled as bar elements with drag coefficients and added mass coefficients as tabulated in Table 6.8, along with the other properties of the mooring lines. These are the same as used in the LIFES50+ project, except that the length of the mooring lines are changed since they are attached at 40 m water depth instead of at 9.5 m above the MSL, as well as mounted closer to the centered column compared to the OO-Star concept. To each mooring line there is a weight of 51 025 kg attached.

Table 6.8: Properties of the mooring system

Parameter	**Value**
Number of mooring lines [-]	3
Adjacent angle [degrees]	120
Anchor depth below MSL [m]	130
Length [m]	455.3
Anchor radius from center line [m]	468.2
Mass one mooring line [t]	219.95
Clump weight [kg]	51 025
Cross-sectional area [m^2]	0.048
Drag coefficient in tangential direction [-]	0.25465
Drag coefficient in normal direction [-]	2.0
Added mass coefficient in normal direction [-]	1.0

The attachment of the mooring system to the structure was moved several times. The mooring lines were at a first stage attached to the periphery of the heave plate mounted on the bottom of the centered column. However, this did not provide enough stiffness in yaw. The three mooring lines were then attached to the top of three of the outer columns. This was neither a good solution as it gave large differences to the remaining three columns. Hence, three crowfoot cables were attached to the outer columns to which the three mooring lines were connected. However, this gave unsymmetrical distribution of forces to the foundation. Hence, the mooring lines were again attached to the periphery of the heave plate which at this stage had been given a larger circumference in order to achieve a larger heave period outside the wave period. In turn, also the yaw stiffness was satisfactory. The entire mooring line hence consist of a catenary line anchored to the seafloor and connected to the heave plate, with a clump weight attached to them.

For long cylinders in infinite fluid, the added mass coefficient can be approximated as 1.0 [-]. This was done for the mooring lines in the model developed in SIMO-RIFLEX-AeroDyn, which was also done in the LIFES50+ project (DNV GL 2017).

6.11 Modelling of the Blades

The blade model is the same as used in the LIFES50+ project, and consist of 26 elements modelled as beam cross-sections. They have a total length of 86.37 m per blade, and weigh 41.7 t each. A stiffness proportional damping is included on the blades, and they are given an axial stiffness of 1E+12 N, a bending stiffness around both y- and z-axis of 1E+12 Nm^2, and a torsion stiffness of 1E+12 Nm^2/rad.

7 ULS Analyses

In this section, the procedure of the assessment of the ultimate strength will be explained. Four different load cases will be run on the new foundation concept, changing the wind speed, significant wave height, peak period and shear parameter. The elements in the tensegrity system are then checked for large axial forces as well as large relative displacements. Sensitivity studies will then be conducted in order to look at how different modifications to the critical elements in the tensegrity system changes the response.

7.1 Resolution Requirements

In the setup of design simulations, the resolution, i.e. the simulation length and number of seeds, of the relevant environmental conditions, is important in order to obtain converged solutions. If for example the resolution of the wind speed is too coarse, effects such as the 3P tower excitation may not be captured. This may lead to an over- or, worse, underestimation of fatigue damage or ultimate loading. In a complete design analysis, sensitivity studies are therefore necessary to perform. However, in this thesis, assumptions will be made regarding this due to time limitations.

Each simulation is set to 4000 s and corresponds to a 3000 s dynamic analysis since the first 1000 s are filtered to eliminate the start-up transient effects. This run-in-time is expected for different semi-submersible concepts if no proper initial condition apart from the correct rotor speed is applied (Müller et al. 2017).

7.2 Base Load Cases

Load cases define the specific design load criteria for the structural design according to defined classes of environmental impact. These external conditions describe the wind, waves, currents, etc. in different severeness. The intention of the load case definitions is to cover all relevant load situations within the designed lifetime of the system. However, due to time limitations, only a selection of load cases will be analysed in this work, as well as a limited number of seeds, with only two seeds for the wind and five seeds for the waves. It is important to emphasize that the reduced set of load cases cannot be taken to be sufficient for a complete design.

Three operational conditions as well as one extreme (parked) condition has been se-

lected among the derived critical design load cases (DLCs) in ULS in the LIFES50+ project (Krieger et al. 2015) and the DTU Wind Energy Offshore Design Load Basis (Natarajan et al. 2016), where the same WT as used in this work was analysed. The load cases from this project are tabulated in Appendix D. Even though the selected load cases may not be the critical DLCs for the present structure as the foundation is not the same, they will be used in the ULS analysis since this work considers the early design phase of the tensegrity-based foundation concept, and the goal is to check if the concept of using a tensegrity system is at all realistic, not arrive at a final design. Hence, a simplified strategy for the foundation system has been performed to find out if it is possible to use. In order to decide which load cases that should have been considered, it is recommended to perform extensive sensitivity analyses.

In the LIFES50+ project, partial safety factors (PSFs) have been applied, as tabulated in Table D2. This has not been done in this work, as the purpose was to investigate the application of a tensegrity-based system to a FOWT foundation concept, and not arrive at a final design. Hence, the design procedure in this work has not been conducted according to DNV standards.

Three of the chosen load cases correspond to ultimate loads in severe sea state (SSS) during power production in which the blades are rotating and the control is active, and one analysis correspond to ultimate loads in extreme sea state (ESS) during parked condition in which the blades are pitched and the turbine is shut down to avoid damage in extreme conditions. The definition of extreme events in wind industry standards are the 50 years recurrence period. Hence, a 50 year wind and wave environment is applied in this condition, which for the considered site in the LIFES50+ project, the Gulf of Main, is equal to a wind speed of $v_{50} = 44$ m/s and a significant wave height of $H_{s,50} = 10.9$ m. The resulting load cases are tabulated in Table 7.1.

Table 7.1: Ultimate limit state dynamic load cases in different sea states (SS) for operational and extreme condition

Base load case	**U** [**m/s**]	$\mathbf{H}_s$ [**m**]	$\mathbf{T}_p$ [**s**]	**Shear**	**SS**	**Turbine status**
1 (Below-rated)	4	7.7	18	0.14	SSS	Operating
2 (Rated)	11.4	10.9	20	0.14	SSS	Operating
3 (Above-rated)	26	10.9	11.7	0.14	SSS	Operating
4 (Extreme)	v_{50}	10.9	11.7	0.11	ESS	Parked

As shown in Table 7.1, the operational conditions include below-rated, rated, and

above-rated wind speeds. For these conditions, the minimum peak wave period used in the LIFES50+ project is chosen according to (DNV GL AS 2016)

$$11.1\sqrt{\frac{H_{s,50}}{g}} \leq T, \tag{7.1}$$

obtaining a minimum wave period of $T_{min} = 11.7$ s. The upper wave period is set to T = 20 s to give indication to the effect of swell waves on the structure (Müller et al. 2017).

The shear parameter tabulated in Table 7.1 is used to compute the mean u-component wind speeds across the rotor disk (Jonkman 2016). It is the exponent used to define the power-law wind profile, as defined in Equation (2.4), corresponding to the exponent α.

For semi-submersible foundations, wave lengths which are a portion of the distance between structure buoyancy columns could cause strong excitation and significant ULS loads (Müller et al. 2017). This indicates that it is not necessarily extreme wave heights that result in maximum loads; specific wave periods at lower wave heights might provide dimensioning loads. Therefore, a careful selection of wave periods is recommended. This is the reason for which a large number of wave periods have been considered in the ULS analyses conducted in the LIFES50+ project, as defined in Table D1 in the appendix, even though only a selection of these will be used in the analyses performed in this work due to time limitations.

7.3 Input Into TurbSim

An example TurbSim input-file is attached in Appendix C. The turbulence intensity is set to "B", which is a standard IEC category of turbulence characteristic and is defined in the international standard IEC61400-1 3rd edition (International Electrotechnical Commission 2005). Also, the normal turbulence model (NTM) is defined in this standard, which is used as the standard wind turbulence model in the analyses conducted in this thesis. The wind files constructed in TurbSim, as discussed in Section 2.4.2, were inserted into SIMO-RIFLEX-AeroDyn with these variables defined, as well as the variables in Table 7.1.

7.4 Sensitivity Analyses

In Table 7.1, the base load cases are tabulated. In the following sections, the different sensitivity analyses conducted will be explained, and the results from these, presented in Section 8, will be compared to the ones from the base load cases.

The different parts of the tensegrity system were divided into three groups during the sensitivity analyses in order to modify only the groups exceeding the total allowable maximum stress after running the base load cases. σ_{max} represents this limit, which was set to 600 MPa after guidance with the supervisors. From Equation (7.2), the corresponding maximum allowable force in the guy wires was found, where A is the cross-sectional area of the guy wires. The groups are as indicated in Table 7.2.

$$F_{max} = A \cdot \sigma_{max} \tag{7.2}$$

Table 7.2: Groups in the tensegrity system

Group	**Part of tensegrity system**
1	Angled wire below water
2	Angled wire above water
3	Horizontal wires

7.4.1 Sensitivity Analysis 1: Modifying the Cross-Sectional Areas

The guy wires experiencing large axial forces can have their cross-sectional areas increased in order to reduce the response. The cross-sectional area was found according to Equation (7.3), where S_{max} is the maximum force encountered in the most critical guy wire in the tensegrity system during the base load cases for each group, and the allowable pretension stress σ_a was set to 300 MPa.

$$A = \frac{S_{max}}{\sigma_a} \tag{7.3}$$

In order to find the importance of the geometric stiffness, the stressfree lengths of the guy wires with modified cross-sectional areas must be altered. The reason is that when the cross-sectional areas are increased, the pretensioned force will increase. In order to maintain a constant pretension F, the stressfree lengths L_0 can be modified according to

$$L_0 = \frac{EAL}{F + EA}, \tag{7.4}$$

found by solving Equation (6.8) with repsect to L_0. L is the length of the guy wire.

7.4.2 Sensitivity Analysis 2: Modifying the Effective Young's Modulus and Adding Rayleigh Damping

Another way of restricting the response in the guy wires is to add polyurethane clumps, damping out the response in order to keep the dynamic response within an acceptable level as discussed in Section 2.6.2. A study of changing the effective axial stiffness $(EA)_{eff}$ on the components in the tensegrity system experiencing large forces, can be performed to achieve this. In order to calculate the effective axial stiffness $(EA)_{eff}$, the following equation was used

$$\frac{(EA)_{eff}}{L_w} = \frac{1}{\frac{L_w - L_p}{EA_w} + \frac{L_p}{E_p A_p}}, \tag{7.5}$$

where A_w is the cross-sectional area of the guy wire, L_w is the length of the guy wire, L_p is the length of the polyurethane section, $E = 2.1\text{E+}05$ MPa is the Young's modulus of the guy wire, $E_p = 300$ MPa is the Young's modulus of the polyurethane, and A_p is the cross-sectional area of the polyurethane. The length of the polyurethane section L_p is taken to be 10% of the length of the wires after guidance with the supervisors.

The cross-sectional area of the polyurethane material was found from Equation (7.6). The denominator represents the maximum stress, chosen after guidance with the supervisors.

$$A_p = \frac{S_{max}}{10\ MPa} \tag{7.6}$$

As explained in Section 7.4.1, the stressfree lengths of the modified guy wires must be altered according to Equation (7.4) in order to look at the effect of the geometric stiffness. This was also done in the present sensitivity analysis.

In addition to changing the effective axial stiffness, a stiffness proportional damping was added to the guy wires. As discussed in Section 3.2.4.2, the Rayleigh damping model is convenient in order to obtain the structural viscous damping. At a first stage, it was assumed a stiffness proportional Rayleigh damping λ as defined in

Equation (3.15) of 5% after guidance with the supervisors. The frequency ω was found from the time plot of the axial force in the most critical guy wire. The time period T between the maximum force encountered in the guy wire and the following maximum was used to find the frequency from Equation (7.7).

$$\omega = \frac{2\pi}{T} \tag{7.7}$$

7.4.3 Sensitivity Analysis 3: Reducing the Axial Stiffness

In order to look at the effect of applying guy wires with low axial stiffness, it was reduced by a factor of 100 while also adjusting the stressfree lengths according to Equation (7.4). Polyester could be such a material, being relatively elastic. Applying such an elastic material on the wires, there can be issues with large relative displacements of the system. This will be reported in the result section.

7.4.4 Sensitivity Analysis 4: Reducing the Axial Stiffness and Adding Rayleigh Damping

Applying more elastic guy wires, the system will act less static, and will be approaching the resonance frequency as seen in Figure 2.3, i.e. $\beta \to 1$. In this area, applying damping to the system will have an effect, which was studied in sensitivity analysis 4 by reducing the axial stiffness by the same amount as in sensitivity analysis 3, and applying the same Rayleigh damping as was done in sensitivity analysis 2.

8 Results and Discussion of the ULS Analyses

Each base load case was run with five different wave seeds and two different wind seeds. In the following sections, the results from the seed in the load case causing the largest force in one of the beams or guy wires in the tensegrity system, are tabulated. The section names in bold letters represents these critical elements, which are also plotted for each load case. The different sections of the tensegrity system are schematically represented with their respective names in Appendix E, along with the numbering of the outer columns.

In addition, in order to look at the relative motion between the outer columns and the centered column, the angle between their relative position before the dynamics are introduced to the analysis, and their maximum and minimum relative positions during the analysis, is tabulated for all the six outer columns. Also, the mean angles and standard deviations are presented. A large relative angle may cause reduction in fatigue life, and is desired to keep at a minimum. The guy wire connectors must be able to resist these angles, and end moments should be avoided as fretting can occur, as discussed in Section 2.7.5. Hence, the attachments should allow for relative motion of the guy wires, which will give an additional cost, in order to avoid local bending moments. In addition, the local tensions at the connections of the wires must be low enough for them not to break, which requires large enough cross-sectional areas of the guy wires.

8.1 Results from Base Load Case 1

Table 8.1: Resulting forces and standard deviation for all the sections in the tensegrity system after running base load case 1

Section	**Max force [MN]**	**Min force [MN]**	**Mean [MN]**	**Standard deviation [MN]**
Guy wires				
AngTop1	10.16	7.07	8.89	0.37
AngTop2	9.71	8.06	9.00	0.22
AngTop3	10.89	7.72	9.12	0.35
AngTop4	10.91	7.72	9.13	0.36
AngTop5	9.70	8.06	9.01	0.22
AngTop6	10.16	7.08	8.89	0.37
AngBott1	15.19	13.41	14.27	0.24
AngBott2	14.97	13.60	14.21	0.17
AngBott3	15.16	13.14	14.14	0.24
AngBott4	15.16	13.13	14.14	0.24
AngBott5	15.19	13.41	14.27	0.24
AngBott6	14.97	13.59	14.21	0.17
TopMid1	4.23	2.65	3.35	0.20
TopMid2	3.42	3.16	3.29	0.03
TopMid3	3.93	2.20	3.22	0.20
TopMid4	3.94	2.19	3.21	0.20
TopMid5	3.43	3.16	3.29	0.03
TopMid6	4.23	2.65	3.35	0.19
BottMid1	4.51	2.31	3.66	0.25
BottMid2	4.15	3.24	3.74	0.14
BottMid3	4.85	3.00	3.81	0.24
BottMid4	4.86	3.02	3.81	0.24
BottMid5	4.14	3.26	3.74	0.14
BottMid6	4.50	2.33	3.66	0.25
Beams				
CmpTop1	-11.26	-10.30	-10.91	0.12
CmpTop2	-11.25	-10.40	-10.92	0.12
CmpTop3	-11.20	-10.58	-10.92	0.08
CmpTop4	-11.25	-10.40	-10.92	0.12
CmpTop5	-11.26	-10.30	-10.91	0.12
CmpTop6	-11.21	-10.51	-10.90	0.09
CmpBott1	-14.72	-13.74	-14.24	0.14
CmpBott2	-14.73	-13.75	-14.27	0.15
CmpBott3	-14.77	-13.85	-14.28	0.12
CmpBott4	-14.73	-13.74	-14.27	0.15
CmpBott5	-14.72	-13.75	-14.24	0.14
CmpBott6	-14.70	-13.73	-14.23	0.11

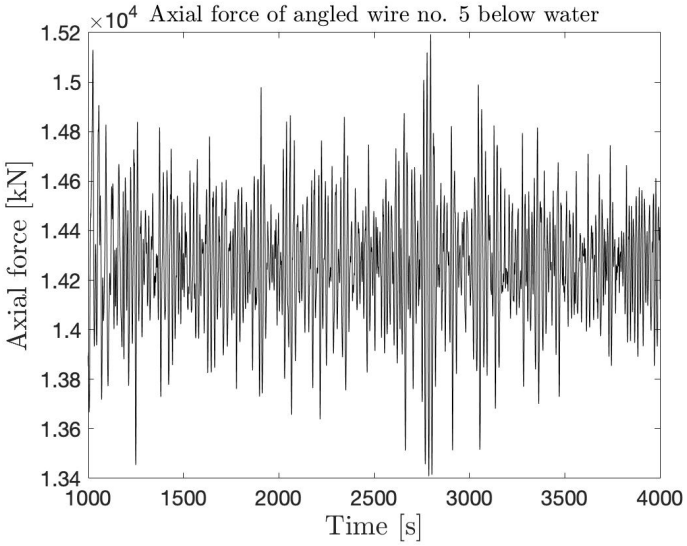

Figure 8.1: Axial force of angled wire number five below water (AngBott5)

It can be seen from the tabulated results in Table 8.1 that the forces in the angled guy wires become large compared to the horizontal guy wires, which is expected as these carry the weight of the centered column.

Table 8.2: Relative angles between the outer columns and shaft and standard deviation after running base load case 1

Column	**Max angle** [**degrees**]	**Min angle** [**degrees**]	**Mean angle** [**degrees**]	**Standard deviation** [**degrees**]
1	5.33	0.23	0.98	0.91
2	2.16	0.19	0.59	0.18
3	5.70	0.25	1.14	0.71
4	5.33	0.23	0.98	0.91
5	2.17	0.19	0.59	0.18
6	5.71	0.25	1.14	0.71

The relative angles between each of the outer columns and the shaft are tabulated in Table 8.2 for base load case 1. It can be seen that they are relatively small, with a maximum of 5.71° between outer column number 6 and the centered column. This is as expected considering a small sea state.

8.2 Results from Base Load Case 2

Table 8.3: Resulting forces and standard deviation for all the sections in the tensegrity system after running base load case 2

Section	**Max force [MN]**	**Min force [MN]**	**Mean [MN]**	**Standard deviation [MN]**
Guy wires				
AngTop1	10.94	7.39	8.92	0.51
AngTop2	9.90	7.79	9.00	0.30
AngTop3	10.74	6.57	9.09	0.48
AngTop4	10.92	7.19	9.10	0.48
AngTop5	10.26	7.80	9.01	0.30
AngTop6	11.51	7.43	8.93	0.51
AngBott1	15.36	12.92	14.25	0.33
AngBott2	15.21	13.38	14.21	0.25
AngBott3	15.56	13.03	14.16	0.34
AngBott4	15.41	12.92	14.16	0.34
AngBott5	15.34	12.56	14.24	0.34
AngBott6	15.20	13.40	14.20	0.25
TopMid1	4.22	2.15	3.33	0.26
TopMid2	3.71	3.11	3.29	0.051
TopMid3	4.67	2.32	3.24	0.27
TopMid4	4.47	2.21	3.23	0.27
TopMid5	3.48	2.88	3.28	0.05
TopMid6	4.29	1.73	3.32	0.27
BottMid1	5.00	2.54	3.68	0.33
BottMid2	4.29	3.04	3.73	0.17
BottMid3	4.77	2.18	3.79	0.31
BottMid4	4.82	2.51	3.79	0.31
BottMid5	4.51	3.06	3.74	0.17
BottMid6	5.28	2.63	3.69	0.33
Beams				
CmpTop1	-11.39	-10.09	-10.91	0.16
CmpTop2	-11.42	-10.19	-10.92	0.16
CmpTop3	-11.28	-10.43	-10.92	0.11
CmpTop4	-11.41	-10.19	-10.92	0.16
CmpTop5	-11.37	-10.10	-10.91	0.16
CmpTop6	-11.32	-10.41	-10.91	0.13
CmpBott1	-14.86	-13.66	-14.24	0.17
CmpBott2	-14.98	-13.58	-14.26	0.18
CmpBott3	-14.83	-13.67	-14.27	0.17
CmpBott4	-14.98	-13.64	-14.27	0.18
CmpBott5	-14.86	-13.62	-14.25	0.17
CmpBott6	-14.81	-13.74	-14.23	0.15

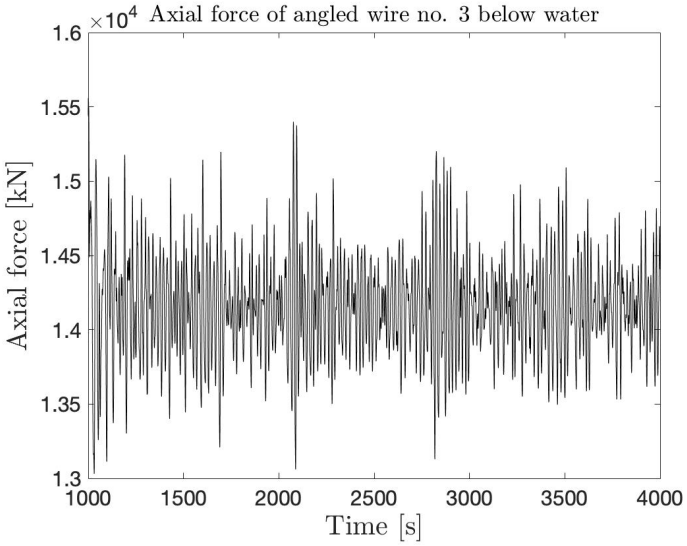

Figure 8.2: Axial force of angled wire number three below water (AngBott3)

The resulting axial forces after running base load case 2 have increased somewhat compared to base load case 1, which is as expected since the wind speed and significant wave height have increased.

Table 8.4: Relative angles between the outer columns and shaft and standard deviation after running base load case 2

Column	**Max angle** [**degrees**]	**Min angle** [**degrees**]	**Mean angle** [**degrees**]	**Standard deviation** [**degrees**]
1	18.15	0.01	3.33	5.12
2	5.86	0.01	0.88	0.80
3	18.61	0.03	3.63	5.23
4	18.17	0.03	3.33	5.12
5	5.88	0.04	0.88	0.80
6	18.57	0.02	3.62	5.22

The relative angles have also increased significantly compared to base load case 1, as both the wind speed and significant wave height have increased. Similarly to base load case 1, columns 2 and 5 have a significantly lower maximum relative angle compared to the other columns. This is due to the pitch moment which columns 2 and 5, laying on the axis of rotation, does not encounter.

8.3 Results from Base Load Case 3

Table 8.5: Resulting forces and standard deviation for all the sections in the tensegrity system after running base load case 3

Section	**Max force [MN]**	**Min force [MN]**	**Mean [MN]**	**Standard deviation [MN]**
Guy wires				
AngTop1	11.45	7.16	9.15	0.57
AngTop2	10.35	7.52	8.99	0.38
AngTop3	10.48	7.02	8.88	0.49
AngTop4	10.38	6.82	8.91	0.49
AngTop5	10.40	7.68	9.03	0.38
AngTop6	11.41	7.26	9.17	0.57
AngBott1	15.07	12.64	14.10	0.32
AngBott2	15.16	13.43	14.22	0.21
AngBott3	16.05	13.31	14.28	0.37
AngBott4	16.07	13.29	14.27	0.37
AngBott5	15.13	12.64	14.09	0.32
AngBott6	15.14	13.44	14.19	0.22
TopMid1	4.48	1.61	3.18	0.33
TopMid2	3.78	2.76	3.30	0.12
TopMid3	5.35	2.37	3.39	0.37
TopMid4	5.37	2.38	3.37	0.37
TopMid5	3.80	2.71	3.28	0.12
TopMid6	4.50	1.61	3.17	0.33
BottMid1	5.55	2.21	3.82	0.47
BottMid2	5.24	2.32	3.72	0.38
BottMid3	4.78	2.15	3.65	0.38
BottMid4	4.63	2.04	3.66	0.38
BottMid5	5.26	2.44	3.75	0.38
BottMid6	5.64	2.17	3.83	0.47
Beams				
CmpTop1	-11.86	-9.66	-10.92	0.27
CmpTop2	-11.89	-9.45	-10.92	0.28
CmpTop3	-11.49	-10.19	-10.93	0.13
CmpTop4	-11.90	-9.51	-10.92	0.27
CmpTop5	-11.88	-9.76	-10.92	0.26
CmpTop6	-11.58	-10.25	-10.91	0.14
CmpBott1	-15.87	-12.68	-14.26	0.41
CmpBott2	-15.88	-12.42	-14.23	0.44
CmpBott3	-14.91	-13.46	-14.23	0.20
CmpBott4	-15.88	-12.43	-14.24	0.44
CmpBott5	-15.89	-12.78	-14.26	0.41
CmpBott6	-14.89	-13.73	-14.27	0.16

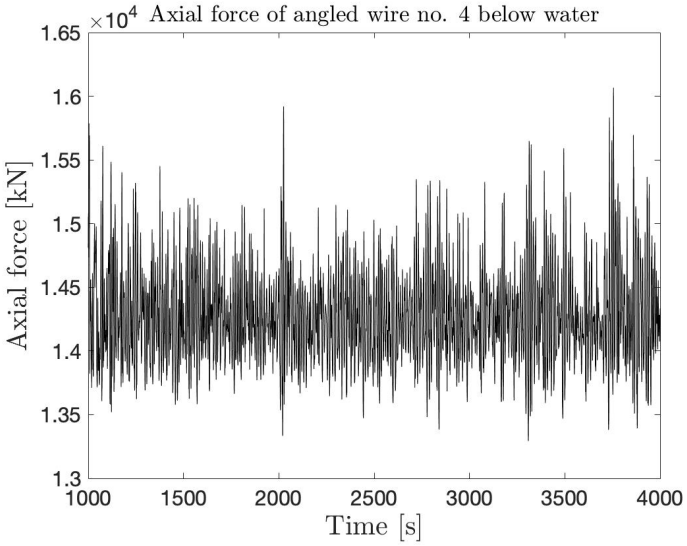

Figure 8.3: Axial force of angled wire number four below water (AngBott4)

The results in Table 8.5 show that the forces in the horizontal guy wires have increased compared to the two aforementioned load cases. For the angled guy wires however, there is no clear tendency; some of the forces have increased, others have decreased. The forces in the beams have all increased.

Table 8.6: Relative angles between the outer columns and shaft and standard deviation after running base load case 3

Column	**Max angle** [**degrees**]	**Min angle** [**degrees**]	**Mean angle** [**degrees**]	**Standard deviation** [**degrees**]
1	12.68	0.00	2.61	3.27
2	11.64	0.00	1.76	2.47
3	13.00	0.00	2.63	3.56
4	12.67	0.00	2.62	3.27
5	11.65	0.00	1.77	2.48
6	13.00	0.00	2.63	3.56

Despite an increased wind speed and a smaller wave peak period, the relative angles have decreased compared to base load case 2, except for columns 2 and 5. This may be due to the change in the wave peak period, as some wave periods which are a portion of the distance between the buoyancy elements could cause larger responses as discussed in Section 7.2.

8.4 Results from Base Load Case 4

Table 8.7: Resulting forces and standard deviation for all the sections in the tensegrity system after running base load case 4

Section	**Max force [MN]**	**Min force [MN]**	**Mean [MN]**	**Standard deviation [MN]**
Guy wires				
AngTop1	12.03	7.62	9.55	0.59
AngTop2	11.16	7.82	9.32	0.45
AngTop3	10.51	7.22	8.84	0.49
AngTop4	10.01	6.69	8.56	0.48
AngTop5	9.98	7.29	8.76	0.41
AngTop6	11.55	7.42	9.28	0.57
AngBott1	14.98	12.15	13.86	0.36
AngBott2	14.98	12.96	14.02	0.27
AngBott3	15.99	13.07	14.29	0.37
AngBott4	16.29	13.43	14.45	0.36
AngBott5	15.01	12.56	14.02	0.33
AngBott6	15.27	13.68	14.33	0.23
TopMid1	4.18	1.28	2.95	0.34
TopMid2	3.77	2.40	3.12	0.18
TopMid3	5.42	2.16	3.43	0.37
TopMid4	5.67	2.60	3.59	0.38
TopMid5	4.38	2.78	3.45	0.17
TopMid6	4.57	1.63	3.12	0.32
BottMid1	5.83	2.40	4.06	0.47
BottMid2	5.53	2.55	3.92	0.40
BottMid3	4.58	2.12	3.61	0.37
BottMid4	4.50	1.87	3.42	0.39
BottMid5	4.99	2.15	3.56	0.39
BottMid6	5.62	2.08	3.89	0.46
Beams				
CmpTop1	-11.79	-9.86	-10.96	0.24
CmpTop2	-11.97	-9.56	-10.95	0.27
CmpTop3	-11.47	-10.18	-10.93	0.12
CmpTop4	-11.97	-9.39	-10.92	0.30
CmpTop5	-11.90	-9.59	-10.94	0.28
CmpTop6	-11.64	-10.25	-10.95	0.15
CmpBott1	-15.87	-12.96	-14.32	0.38
CmpBott2	-15.89	-12.46	-14.25	0.44
CmpBott3	-14.85	-13.39	-14.17	0.20
CmpBott4	-15.82	-12.36	-14.16	0.45
CmpBott5	-15.86	-12.60	-14.23	0.42
CmpBott6	-14.87	-13.78	-14.30	0.16

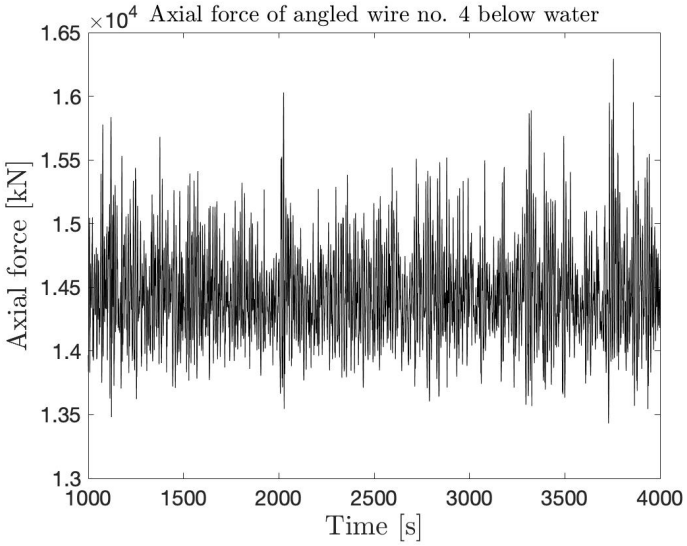

Figure 8.4: Axial force of angled wire number four below water (AngBott4)

The results after running base load case 4 show that the forces in the guy wires have both decreased and increased compared to the three aforementioned base load cases. The forces in the beams have increased compared to load cases 1 and 2, but compared to load case 3, some forces have also decreased. Even though the wind speed for load case 4 is much larger compared to the three previous, the turbine is now parked in order to minimize the loads on the turbine in extreme conditions, which may be one reason to which some sections have reduced forces. In addition, the wind shear has been decreased, which may be another contribution to the reduction, as well as possible wave cancellation effects due to the semi-submersible geometry; the wave forces acting on the submerged parts of the semi-submersible with different phases cancel each other out due to phase shifts (Patel 2013).

Table 8.8: Relative angles between the outer columns and shaft and standard deviation after running base load case 4

Column	**Max angle** [**degrees**]	**Min angle** [**degrees**]	**Mean angle** [**degrees**]	**Standard deviation** [**degrees**]
1	11.93	0.04	2.70	0.92
2	5.25	0.05	2.26	0.83
3	15.31	0.01	1.94	0.91
4	11.92	0.03	2.70	0.92
5	5.24	0.05	2.26	0.83
6	15.34	0.01	1.95	0.91

The relative angles after running base load case 4 presented in Table 8.8 have both increased and decreased compared to base load case 3, which both are load cases

having relatively large wind speeds, but where the turbine status' are different; one is operating and another is parked. Again, a lower maximum relative angle is seen in columns 2 and 5 compared to the other columns. Compared to load case 2, all of the maximum angles have decreased, whereas compared to base load case 1, all have increased.

8.5 Results from the Sensitivity Analyses

From Equation (7.2), the maximum allowable force in the guy wires was found to be 8.58 MN. According to the resulting axial forces tabulated in the previous sections after running the four base load cases (Tables 8.1, 8.3, 8.5, 8.7), it is the angled wires that exceed this limit, i.e. groups 1 and 2 as indicated in Table 7.2. In the sections below, the results from the different alterations made to these guy wires as explained in Section 7.4 will be presented in order to look at the effect of the different modifications. Base load case 4 is the one that will be run in the sensitivity studies, as it encountered the largest responses of the four base load cases.

The tabulated differences in the following sections are the fraction between the maximum force or maximum angle encountered in the sensitivity study and the maximum force or maximum angle from the base load case for the respective sections in the tensegrity system. For a number < 1, the value has decreased compared to the base load case.

8.5.1 Results from Changing the Cross-Sectional Areas

Base load case 4 gave the overall maximum force in one of the guy wires, with $S_{max} = 16.29$ MN in angled wire number four below water, belonging to group 1. The maximum force encountered during the four base load cases by group 2, was also during load case 4, with a maximum force of $S_{max} = 12.03$ MN. These will be the dimensioning wires used to find the cross-sectional areas for groups 1 and 2 according to Equation (7.3). In addition, by changing the stressfree lengths according to Equation (7.4), inserting the pretension tabulated in Table 6.5, one finds the influence of the geometric stiffness. The resulting modifications are summarized in Table 8.9, and the results after rerunning base load case number 4 are tabulated in Table 8.10.

Table 8.9: Changes made to groups 1 and 2 in sensitivity analysis 1

	A [m^2]	EA [N]	L_0 [m]
Group 1	0.0543	1.14E+10	39.629
Group 2	0.0401	8.42E+09	39.612

Table 8.10: Resulting forces, standard deviation and difference from base load case 4 for all the sections in the tensegrity system after running sensitivity analysis 1

Section	**Max force** [MN]	**Min force** [MN]	**Mean** [MN]	**Standard deviation** [MN]	**Difference** [-]
Guy wires					
AngTop1	9.66	4.42	6.94	0.69	0.80
AngTop2	8.81	4.98	6.69	0.51	0.79
AngTop3	8.04	4.19	6.15	0.56	0.76
AngTop4	7.45	3.53	5.84	0.57	0.74
AngTop5	7.54	4.43	6.06	0.47	0.76
AngTop6	9.23	4.27	6.63	0.68	0.80
AngBott1	12.60	9.75	11.36	0.35	0.84
AngBott2	12.44	10.40	11.51	0.26	0.83
AngBott3	13.82	10.40	11.73	0.43	0.86
AngBott4	14.18	10.11	11.85	0.44	0.87
AngBott5	12.64	10.21	11.49	0.31	0.84
AngBott6	12.71	11.04	11.75	0.22	0.83
TopMid1	4.50	1.47	3.27	0.40	1.08
TopMid2	4.13	2.46	3.46	0.22	1.10
TopMid3	5.83	2.39	3.82	0.39	1.08
TopMid4	6.02	2.96	4.01	0.39	1.06
TopMid5	4.61	3.23	3.85	0.19	1.05
TopMid6	5.02	1.83	3.47	0.38	1.10
BottMid1	6.03	2.99	4.37	0.41	1.03
BottMid2	5.64	3.07	4.24	0.34	1.02
BottMid3	4.81	2.85	3.97	0.32	1.05
BottMid4	4.70	2.58	3.80	0.32	1.04
BottMid5	5.09	2.75	3.92	0.32	1.02
BottMid6	5.81	2.69	4.22	0.40	1.03
Beams					
CmpTop1	-9.92	-8.16	-9.21	0.21	0.84
CmpTop2	-10.11	-7.91	-9.21	0.24	0.84
CmpTop3	-9.77	-8.52	-9.20	0.11	0.85
CmpTop4	-10.15	-7.67	-9.18	0.27	0.85
CmpTop5	-10.06	-7.92	-9.20	0.26	0.85
CmpTop6	-9.78	-8.54	-9.20	0.13	0.84
CmpBott1	-14.14	-11.36	-12.70	0.36	0.89
CmpBott2	-14.15	-10.89	-12.62	0.42	0.89
CmpBott3	-13.27	-11.73	-12.54	0.21	0.89
CmpBott4	-14.09	-10.77	-12.53	0.43	0.89
CmpBott5	-14.12	-11.04	-12.61	0.40	0.89
CmpBott6	-13.28	-12.16	-12.68	0.17	0.89

Table 8.10 shows that the maximum forces have decreased for all the sections in the tensegrity system compared to base load case 4, except for the horizontal guy wires. When the axial stiffness is increased in the angled guy wires, the response decreases since they act more statically. This can be seen from Figure 2.3; for a $\beta < 1$, the response decreases. In order to look at the effect on the eigenfrequency from increasing the axial stiffnesses, the local eigenfrequency from the current sensitivity study can be calculated and compared with the one from the base load case. The eigenfrequency was found from Equation (8.1), where K is the stiffness contribution from all the wires connected to one outer column, and m is the mass and added mass of one outer column tabulated in Tables 5.8 and 6.3, respectively.

$$\omega_0 = \sqrt{\frac{K}{m}} \tag{8.1}$$

The stiffness was found from $K = \frac{EA}{L_0}$, which for the base load case correspond to EA = 3.0E+09 N and stressfree lengths as indicated in Table 6.5. For the current sensitivity analysis, the axial stiffnesses and stressfree lengths for groups 1 and 2 are as tabulated in Table 8.9, whereas the horizontal guy wires have the same properties as the base load case.

To find the frequency ratio β, the load frequency ω was found from Equation (7.7), inserting the peak wave period $T_p = 11.7$ s used in base load case 4, resulting in $\omega = 0.537$ rad/s. β was then found from the following equation

$$\beta = \frac{\omega}{\omega_0}. \tag{8.2}$$

The resulting eigenfrequencies and frequency ratios are tabulated in Table 8.11. It is seen that by increasing the axial stiffnesses in groups 1 and 2, the frequency ratio decreases, and the wires will act more static. As seen from Figure 2.3, the response will then decrease compared to the base load case, which is in accordance with the results found in Table 8.10.

Table 8.11: Eigenfrequency and frequency ratio for the base case and sensitivity analysis 1

	Eigenfrequency ω_0 [rad/s]	**Frequency ratio β [-]**
Base case	31.9	0.0168
Sensitivity 1	43.6	0.0123

Table 8.12: Relative angles between the outer columns and shaft, standard deviation and difference from base load case 4 after running sensitivity analysis 1

Column	**Max angle** [**degrees**]	**Min angle** [**degrees**]	**Mean angle** [**degrees**]	**Standard deviation** [**degrees**]	**Difference** [-]
1	11.83	0.04	2.64	0.91	0.99
2	5.19	0.02	2.21	0.82	0.99
3	15.35	0.05	1.95	0.91	1.00
4	11.93	0.04	2.71	0.92	1.00
5	5.26	0.05	2.27	0.83	1.00
6	15.27	0.05	1.92	0.91	1.00

Compared to base load case 4, the maximum angles in Table 8.12 are approximately the same, indicating that a stiffer system does not affect the relative motions significantly.

Also, the most critical guy wire in the system is still angled wire number 4 below the MSL, as was the case for the base load case.

8.5.2 Results from Changing the Effective Young's Modulus and Adding Rayleigh Damping

Another measure in order to prevent the large axial forces resulting in the guy wires in groups 1 and 2, is to add polyurethane clumps. The polyurethane clump area, A_p, was found from Equation (7.6), and can be inserted into Equation (7.5) in order to find the effective axial stiffness $(EA)_{eff}$. Similar as before, the stressfree lengths L_0 must be modified according to Equation (7.4) in order to maintain a constant pretension. The resulting modifications are tabulated in Table 8.13.

Table 8.13: Changes made to groups 1 and 2 in sensitivity analysis 2

	S_{max} [MN]	A_p [m^2]	$(EA)_{eff}$ [N]	L_0 [m]
Group 1	16.29	1.629	1.98E+09	39.410
Group 2	12.03	1.203	1.73E+09	39.373

In order to find the correct Rayleigh damping to apply, the period T was found from the time plot of the axial force in Figure 8.4 as explained in Section 7.4.2, and inserted into Equation (7.7), yielding a frequency of 0.641 s^{-1}. The stiffness-proportional damping α_2 was then found from Equation (3.15) (α_1 was set to zero), yielding a value of 0.156 s. Even though this damping was found using the period from Figure 8.4, which is the plot of one of the angled guy wires below the MSL, the

same value was used for the angled wires above the MSL as the difference in period will be minimal.

Base load case 4 was rerun with the modifications tabulated in Table 8.13 as well as an applied Rayleigh damping. The results are presented in Table 8.14.

Table 8.14: Resulting forces, standard deviation and difference from base load case 4 for all the sections in the tensegrity system after running sensitivity analysis 2

Section	**Max force** [MN]	**Min force** [MN]	**Mean** [MN]	**Standard deviation** [MN]	**Difference** [-]
Guy wires					
AngTop1	12.53	8.70	10.32	0.52	1.04
AngTop2	11.73	8.77	10.11	0.40	1.05
AngTop3	11.18	8.22	9.67	0.44	1.06
AngTop4	10.70	7.82	9.42	0.43	1.07
AngTop5	10.64	8.30	9.60	0.36	1.07
AngTop6	12.08	8.47	10.07	0.50	1.05
AngBott1	15.81	12.68	14.57	0.41	1.06
AngBott2	15.81	13.54	14.75	0.31	1.06
AngBott3	16.67	13.76	15.07	0.38	1.04
AngBott4	16.97	14.19	15.25	0.37	1.04
AngBott5	15.86	13.11	14.75	0.37	1.06
AngBott6	16.16	14.37	15.11	0.26	1.06
TopMid1	4.07	1.35	2.89	0.30	0.97
TopMid2	3.65	2.36	3.04	0.16	0.97
TopMid3	5.21	2.16	3.30	0.35	0.96
TopMid4	5.55	2.25	3.43	0.36	0.98
TopMid5	4.29	2.65	3.32	0.16	0.98
TopMid6	4.36	1.66	3.03	0.28	0.95
BottMid1	5.86	2.20	3.99	0.51	1.01
BottMid2	5.57	2.36	3.84	0.44	1.01
BottMid3	4.54	1.86	3.50	0.41	0.99
BottMid4	4.46	1.57	3.30	0.42	0.99
BottMid5	4.99	1.94	3.45	0.42	1.00
BottMid6	5.63	1.86	3.80	0.50	1.00
Beams					
CmpTop1	-12.34	-10.41	-11.51	0.24	1.05
CmpTop2	-12.50	-10.09	-11.49	0.27	1.04
CmpTop3	-12.02	-10.74	-11.47	0.12	1.05
CmpTop4	-12.51	-9.93	-11.45	0.30	1.05
CmpTop5	-12.46	-10.12	-11.48	0.28	1.05
CmpTop6	-12.19	-10.80	-11.50	0.15	1.05
CmpBott1	-16.37	-13.43	-14.80	0.38	1.03
CmpBott2	-16.39	-12.95	-14.73	0.44	1.03
CmpBott3	-15.33	-13.90	-14.65	0.19	1.03
CmpBott4	-16.34	-12.84	-14.64	0.46	1.03
CmpBott5	-16.37	-13.09	-14.72	0.42	1.03
CmpBott6	-15.33	-14.26	-14.78	0.15	1.03

It can be seen from the results in Table 8.14 that the effect of geometric stiffness and applying stiffness proportional Rayleigh damping is minimal. Only the horizontal guy wires has had a decrease in maximum force. The reason for the small changes in response is probably due to the static behaviour of the guy wires, i.e. for $\beta \ll 1$, as discussed in Section 2.6.4. In order for the damper to have any effect, the frequency of the system must be close to the resonance frequency ($\beta = 1$). This can occur if for example slamming due to large wave forces becomes a fact. Then large local eigenfrequencies in the guy wires may arise, in which damping can be effective. Also, if the guy wires are relatively flexible, they may approach the resonance frequency. This will be studied in the next section.

In order to look at the effect on the eigenfrequency from adding polyurethane clumps and Rayleigh damping, the same procedure as explained in Section 8.5.1 can be conducted. The stiffness was found using the stressfree lengths and axial stiffnesses tabulated in Table 8.13 for groups 1 and 2, whereas the horizontal guy wires was not modified from the base load case. This resulted in an eigenfrequency of 29.6 rad/s and a frequency ratio of $\beta = 0.0181$ [-]. This is a small increase in frequency ratio compared to the base case, meaning that by applying damping, β becomes larger, but it is still far from the resonance frequency as seen in Figure 2.3. Hence, guy wire damping has limited effect on this structure.

In addition, the most critical section in the tensegrity system is still angled wire number 4 below the MSL, which is similar to base load case 4.

Table 8.15: Relative angles between the outer columns and shaft, standard deviation and difference from base load case 4 after running sensitivity analysis 2

Column	**Max angle** [**degrees**]	**Min angle** [**degrees**]	**Mean angle** [**degrees**]	**Standard deviation** [**degrees**]	**Difference** [-]
1	12.04	0.04	2.76	0.93	1.01
2	5.21	0.02	2.29	0.84	0.99
3	15.34	0.03	1.93	0.92	1.00
4	11.93	0.04	2.69	0.93	1.00
5	5.11	0.01	2.24	0.83	0.98
6	15.47	0.03	1.97	0.93	1.01

The angles tabulated in Table 8.15 are not much different from the ones found during the base load case in Table 8.8, indicating that decreasing the effective axial stiffness and adding Rayleigh damping does not influence the relative angles significantly.

8.5.3 Results from Decreasing the Axial Stiffness

Decreasing the axial stiffnesses of groups 1 and 2 with a factor 100 as was agreed with the supervisors, yielded a value of EA = 3E+07 N. Inserting this value into Equation (7.4) along with the length and pretension tabulated in Table 6.5, yielded a stressfree length for both groups of 27.495 m. Rerunning base load case 4 with modified axial stiffness and stressfree lengths, yielded the following results:

Table 8.16: Resulting forces, standard deviation and difference from base load case 4 for all the sections in the tensegrity system after running sensitivity analysis 3

Section	**Max force** [MN]	**Min force** [MN]	**Mean** [MN]	**Standard deviation** [MN]	**Difference** [-]
Guy wires					
AngTop1	13.81	11.68	12.48	0.27	1.15
AngTop2	13.16	11.51	12.31	0.22	1.18
AngTop3	12.99	10.91	11.97	0.24	1.24
AngTop4	12.96	10.29	11.78	0.30	1.29
AngTop5	12.93	10.83	11.93	0.26	1.30
AngTop6	13.34	11.39	12.29	0.24	1.15
AngBott1	14.90	12.78	14.13	0.26	0.99
AngBott2	15.05	13.46	14.29	0.22	1.00
AngBott3	15.62	13.56	14.61	0.24	0.98
AngBott4	16.16	13.61	14.79	0.29	0.99
AngBott5	15.15	13.26	14.31	0.23	1.01
AngBott6	15.69	13.65	14.65	0.25	1.03
TopMid1	9.77	3.87	7.17	0.65	2.34
TopMid2	9.38	4.00	6.98	0.55	2.49
TopMid3	8.91	2.68	6.53	0.65	1.64
TopMid4	9.03	2.59	6.23	0.72	1.59
TopMid5	9.06	3.42	6.44	0.61	2.07
TopMid6	9.78	3.36	6.93	0.66	2.14
BottMid1	10.07	4.97	7.40	0.57	1.73
BottMid2	9.59	5.74	7.55	0.44	1.73
BottMid3	10.48	3.80	7.74	0.75	2.29
BottMid4	11.00	3.76	7.83	0.86	2.44
BottMid5	10.52	5.11	7.76	0.52	2.11
BottMid6	10.13	5.30	7.54	0.55	1.80
Beams					
CmpTop1	-19.52	-15.06	-17.47	0.54	1.66
CmpTop2	-19.23	-15.12	-17.06	0.52	1.61
CmpTop3	-18.82	-13.86	-16.61	0.61	1.64
CmpTop4	-18.83	-14.15	-16.56	0.56	1.57
CmpTop5	-19.33	-14.33	-17.00	0.56	1.62
CmpTop6	-20.17	-14.31	-17.44	0.63	1.73
CmpBott1	-20.25	-15.56	-17.80	0.51	1.28
CmpBott2	-20.73	-16.14	-18.09	0.52	1.30
CmpBott3	-21.00	-15.62	-18.37	0.60	1.41
CmpBott4	-21.01	-16.36	-18.38	0.60	1.33
CmpBott5	-20.93	-15.56	-18.12	0.55	1.32
CmpBott6	-19.64	-15.67	-17.81	0.48	1.32

It can be seen from the results in Table 8.16 that applying more elastic guy wires is not a good solution for this concept. The forces in all the sections in the tensegrity system increases compared to the base load case, except from the angled wires below water, which maintain approximately the same maximum force as the base load case. As seen from Figure 2.3, when the system becomes more flexible and acts more dynamic, i.e. $\beta \rightarrow 1$, the response will increase if the damping is low.

Table 8.17: Relative angles between the outer columns and shaft, standard deviation and difference from base load case 4 after running sensitivity analysis 3

Column	**Max angle** [**degrees**]	**Min angle** [**degrees**]	**Mean angle** [**degrees**]	**Standard deviation** [**degrees**]	**Difference** [-]
1	15.68	0.53	5.73	1.27	1.31
2	8.54	0.01	4.69	1.10	1.63
3	15.68	0.03	2.15	1.02	1.02
4	11.86	0.01	1.95	0.91	0.99
5	7.32	0.03	1.86	0.63	1.40
6	19.03	0.10	3.86	1.16	1.24

Table 8.17 shows that the relative angles between the shaft and the columns have mostly increased compared to the earlier analyses. More elastic guy wires will be less resistant to changes in shape when being acted on by a physical force. The motions will hence increase, and, as seen from the results, also the relative motions, which again will reduce the fatigue resistance at the connection points.

8.5.4 Results from Decreasing the Axial Stiffness and Adding Rayleigh Damping

The same reduction in axial stiffness and corresponding stressfree length as was applied in sensitivity study 3, as well as the same stiffness-proportional Rayleigh damping as was applied in sensitivity study 2, was applied in this analysis. That is, EA = 3E+07 N, L_0 = 27.495 m, and α_2 = 0.156 s, was applied to groups 1 and 2. The results are summarized in Table 8.18.

Table 8.18: Resulting forces, standard deviation and difference from base load case 4 for all the sections in the tensegrity system after running sensitivity analysis 4

Section	**Max force** [MN]	**Min force** [MN]	**Mean** [MN]	**Standard deviation** [MN]	**Difference** [-]
Guy wires					
AngTop1	13.76	11.69	12.48	0.25	1.14
AngTop2	13.09	11.62	12.32	0.20	1.17
AngTop3	12.77	11.11	11.98	0.22	1.22
AngTop4	12.78	10.44	11.78	0.26	1.28
AngTop5	12.78	10.98	11.93	0.21	1.28
AngTop6	13.22	11.47	12.29	0.23	1.14
AngBott1	14.89	12.82	14.13	0.25	0.99
AngBott2	14.95	13.53	14.29	0.19	1.00
AngBott3	15.44	13.79	14.61	0.21	0.97
AngBott4	16.04	13.78	14.80	0.25	0.98
AngBott5	15.08	13.39	14.31	0.22	1.00
AngBott6	15.55	13.80	14.66	0.20	1.02
TopMid1	9.60	4.24	7.19	0.58	2.30
TopMid2	9.00	4.75	7.00	0.47	2.39
TopMid3	8.95	2.74	6.55	0.63	1.65
TopMid4	8.97	2.51	6.24	0.67	1.58
TopMid5	8.85	3.85	6.45	0.50	2.02
TopMid6	9.17	3.76	6.95	0.61	2.01
BottMid1	9.96	5.17	7.42	0.55	1.71
BottMid2	9.23	6.17	7.56	0.38	1.67
BottMid3	10.28	4.34	7.76	0.69	2.24
BottMid4	10.84	4.11	7.85	0.79	2.41
BottMid5	10.04	5.80	7.78	0.44	2.01
BottMid6	10.02	5.43	7.55	0.52	1.78
Beams					
CmpTop1	-19.39	-15.61	-17.49	0.47	1.64
CmpTop2	-19.04	-15.43	-17.08	0.48	1.59
CmpTop3	-18.78	-14.33	-16.62	0.56	1.64
CmpTop4	-18.54	-14.19	-16.57	0.50	1.55
CmpTop5	-19.08	-14.66	-17.01	0.49	1.60
CmpTop6	-20.06	-14.69	-17.46	0.58	1.72
CmpBott1	-19.99	-15.93	-17.82	0.46	1.26
CmpBott2	-20.38	-16.46	-18.10	0.47	1.28
CmpBott3	-20.49	-16.10	-18.38	0.50	1.38
CmpBott4	-20.74	-16.47	-18.41	0.55	1.31
CmpBott5	-20.66	-15.97	-18.14	0.51	1.30
CmpBott6	-19.52	-15.94	-17.83	0.43	1.31

From Table 8.18, it is shown that compared to base load case 4, the forces in all the sections in the tensegrity system has increased, except for some of the angled guy wires below the MSL. This is the same as was found for sensitivity study 3, although the maximum forces have either decreased or stayed the same compared to this study. However, the differences between the two sensitivity studies are not significant, indicating that even with more flexible guy wires, the damper does not have a significant effect on the forces in this foundation concept. This is though probably because the guy wires are still far from the resonance frequency, with a frequency ratio of 0.0212 [-] found in a similar way as in Section 8.5.1, where damping will be little effective. In the case of snap loads however, dampers will be effective. However, such loads are not desired, and will not occur in this foundation concept since it has been assured that the guy wires remain in tension at all times. From an economic perspective, this is a better solution as dampers are expensive.

Table 8.19: Relative angles between the outer columns and shaft, standard deviation and difference from base load case 4 after running sensitivity analysis 4

Column	**Max angle** [**degrees**]	**Min angle** [**degrees**]	**Mean angle** [**degrees**]	**Standard deviation** [**degrees**]	**Difference** [**-**]
1	15.59	0.67	5.77	1.26	1.31
2	8.45	0.22	4.74	1.08	1.61
3	15.08	0.10	2.17	1.01	0.98
4	11.68	0.02	1.97	0.91	0.98
5	7.12	0.03	1.86	0.61	1.36
6	18.96	0.15	3.86	1.15	1.24

Most of the relative angles have increased compared to base load case 4 as seen in Table 8.19, indicating that decreasing the axial stiffness and adding Rayleigh damping does not have a positive effect on the relative motions.

Compared to sensitivity analysis 3, however, the angles have decreased. This indicates that adding damping has a diminishing effect on the relative motions. However, the differences are small, which is probably due to the fact that the effect of damping is apparent when the resonance frequency appear locally on the wire, and does not affect the forces which occur on a global level. From the guy wires perspective, it is a static load.

9 Conclusion and Recommendations

9.1 Conclusion

An initial design of a tensegrity-type semi-submersible platform supporting the 10 MW DTU reference wind turbine has been successfully performed including a catenary mooring system. The goal was to arrive at a cost-effective design while satisfying strength and safety requirements. A spreadsheet-based design process has resulted in a possible mass reduction of 65.7% with the modified foundation concept compared to the reference semi-submersible foundation developed by Dr.techn. Olav Olsen. This can potentially reduce the cost and environmental footprint of the foundation significantly. Finally, a model was developed in the software SIMO-RIFLEX-AeroDyn, and coupled hydro-aero-servo-elasto dynamic analysis was performed.

A summary of the properties of the tensegrity-based semi-submersible platform is provided in Table 9.1.

Table 9.1: Properties of the tensegrity-type semi-submersible floating wind turbine

Parameter	**Value**
Rated power [MW]	10
Hub height [m]	119
Outer column diameter [m]	7
Outer column height [m]	25
Centered column bottom diameter [m]	11.385
Operation draft [m]	40
Angled wire length [m]	39.675
Horizontal wire length [m]	30.808
Beam length [m]	40
C/c distance outer and center column [m]	40
Foundation mass [t]	7443
Displacement [m^3]	7905
Ballast mass [t]	2690

The reference foundation concept by Dr.techn. Olav Olsen has been modified by adding three additional buoyancy elements and replacing the pontoons with a tensegrity system, connecting the shaft to the buoyancy elements. A ballast mass of

2690 t was placed in the lower end of the shaft in order to achieve a stable structure. The concept has been studied in 130 m water depth.

It was found that the use of a heave plate would be necessary in order to move the structure's natural period in heave away from the wave spectrum. The heave plate was mounted on the bottom of the centered column, 40 m below the MSL, with a cross-sectional area of 1500 m^2 and a thickness of 0.05 m.

The structure was subjected to four different environmental conditions, varying the wind speed, the significant wave height, the peak period and the shear parameter. The results show that the extreme sea state during parked condition, with a wind speed of 44 m/s and a wave height of 10.9 m, was the most critical load case causing the largest responses in the tensegrity system.

Based on the results found in this thesis, the use of a tensegrity-based semi-submersible foundation concept in order to support a FOWT, is feasible. The four sensitivity analyses conducted showed that the best solution in order to reduce the large forces in the angled guy wires was to increase their cross-sectional areas, although this did not reduce the relative displacements between the buoyancy elements and the shaft. Even though increasing the cross-sectional areas will increase the weight of the structure, the mass of the angled guy wires is only a fraction of the total mass of the foundation, and will not make a significant difference. However, it will make the foundation more expensive to construct. Another measure in order to decrease the forces in the angled guy wires is to add several outer columns and guy wires, distributing the forces. However, this was not studied in this work.

9.2 Recommendations for Further Work

Due to limited time, several aspects have not been fully discussed or studied during this work. In addition, several assumptions have been made. Therefore, some recommendations for further work are suggested:

- Assess the effect of changing the thickness and placement of the heave plate, as the placement of the heave plate at the bottom of the centered column is not realistic in a physical concept, having such a large circumferential area and no reinforcement. In such case, the attachment of the mooring system to the hull must also be reassessed, as they now are attached to the heave plate.
- Evaluate different mooring systems.
- Perform a detailed cost analysis of both concepts in order to evaluate the potential cost reduction in more detail.
- Perform FLS analyses of the modified concept.
- Viscous effects on the heave plate should be analysed. The viscous effects on the added mass coefficients are not included in this thesis, nor corrections to the drag coefficients.
- The tower used in this design is initially designed for a land-based WT. A different hub height and tower properties should be used for a FWT.
- Apply another controller in SIMO-RIFLEX-AeroDyn which is more suited for the present concept, as the one used in this work is developed for a bottom-fixed WT.
- Several load cases should be investigated to fully understand the behaviour of the WT. The wind shear, wind-wave misalignment and fault conditions are properties that could be varied.
- Physical model tests or code-to-code comparison is recommended to verify the results.
- Find the optimal number of buoyancy elements in order to distribute the forces in the guy wires while keeping the foundation mass low.
- Other aspects such as fabrication, transportation and installation could be studied.

Bibliography

4C Offshore (2022). *WindFloat 1 Prototype (WF1) Floating Wind Farm*. URL: https://www.4coffshore.com/windfarms/portugal/windfloat-1-prototype-(wf1)-portugal-pt01.html (visited on 15th Apr. 2022).

Abriox (2019). URL: https://www.abriox.com/just-what-is-cathodic-protection/ (visited on 4th Dec. 2021).

Adhikari, Sondipon (2001). 'Damping models for structural vibration'. PhD thesis. Citeseer.

Alkhoury, Philip et al. (2021). 'A full three-dimensional model for the estimation of the natural frequencies of an offshore wind turbine in sand'. eng. In: *Wind energy (Chichester, England)* 24.7, pp. 699–719. ISSN: 1095-4244.

Amdahl, Jørgen (n.d.). *Lecture notes in TMR4195 Design of Ocean Structures - Ultimate Limit States*.

AMPP (2022). *Corrosion Fatigue*. URL: https://www.ampp.org/resources/impact/corrosion-basics/group-3/corrosion-fatigue (visited on 23rd Feb. 2022).

Anzai, H. and T. Endo (1979). 'On-site indication of fatigue damage under complex loading'. In: *International Journal of Fatigue* 1.1, pp. 49–57.

Athanasia, Arapogianni and Anne Benedicte Genachte (2013). 'Deep Offshore and New Foundation Concepts'. In: *Energy Procedia* 35. DeepWind'2013 – Selected papers from 10th Deep Sea Offshore Wind R&D Conference, Trondheim, Norway, 24 – 25 January 2013, pp. 198–209. ISSN: 1876-6102. DOI: https://doi.org/10.1016/j.egypro.2013.07.173. URL: https://www.sciencedirect.com/science/article/pii/S1876610213012599.

Auburn University (2021). *Airmass Stability & Atmospheric Dispersion*. URL: http://www.auburn.edu/academic/forestry_wildlife/fire/airmass_stability.htm (visited on 6th Dec. 2021).

Bachynski and Eliassen (2018). 'The effects of coherent structures on the global response of floating offshore wind turbines.' In: *Wind Energy*. DOI: https://doi.org/10.1002/we.2280.

Bachynski, Erin (2014). 'Design and Dynamic Analysis of Tension Leg Platform Wind Turbines'. PhD thesis. Trondheim: Norwegian University of Science and Technology.

— (2021). *Lecture note: assessing the results from decay tests*.

Bachynski-Polić, Erin (n.d.). *Basic Concepts in Wind Turbine Control*.

Bak, C. (2013). *Description of the DTU 10 MW reference wind turbine*.

Bak, C. et al. (2013). 'Design and performance of a 10 MW wind turbine.' In: *J. Wind Energy*.

Bauer, Josh (n.d.). NREL.

Berge, Stig and Sigmund Kyrre Ås (2017). 'Fatigue an Fracture Design of Marine Structures'. In.

Burton, Tony et al. (2011). *Wind Energy Handbook*. eng. 2. Aufl. Hoboken: Wiley. ISBN: 0470699752.

Chatzigeorgiou, George et al. (2017). '2 - Continuum Mechanics and Constitutive Laws'. In: *Thermomechanical Behavior of Dissipative Composite Materials*. Ed. by George Chatzigeorgiou et al. Elsevier, pp. 37–87. ISBN: 978-1-78548-279-3. DOI: https://doi.org/10.1016/B978-1-78548-279-3.50002-6. URL: https://www.sciencedirect.com/science/article/pii/B9781785482793500026.

Collins, Danielle (2019). URL: https://www.motioncontroltips.com/vibration-damping-whats-the-difference-between-passive-and-active-methods/ (visited on 22nd May 2019).

Comsol (2018). *Eigenfrequency Analysis*. URL: https://www.comsol.com/multiphysics/eigenfrequency-analysis (visited on 18th Jan. 2022).

Cook, R.D. et al. (2002). *Concepts and applications of finite element analysis*. eng. New York.

Cruz, Joao and Mairead Atcheson (2016). *Floating Offshore Wind Energy: The Next Generation of Wind Energy*. eng. Green Energy and Technology. Cham: Springer International Publishing AG. ISBN: 9783319293967.

Damiani, Rick and Max Franchi (2021). 'An innovative second-order design method for the structural optimization of the SpiderFLOAT offshore wind Platform'. In: *Ocean Engineering* 228, p. 108792. ISSN: 0029-8018. DOI: https://doi.org/10.1016/j.oceaneng.2021.108792. URL: https://www.sciencedirect.com/science/article/pii/S0029801821002274.

de Vaal, J.B., M.O.L. Hansen and T. Moan (2014). 'Effect of wind turbine surge motion on rotor thrust and induced velocity'. eng. In: 17.1, pp. 105–121. ISSN: 1095-4244.

Det Norske Veritas (2013). 'DNV-OS-J103. Design of Floating Wind Turbine Structures'. In.

Dinius, James D et al. (2022). 'Control Actuation Options for the SpiderFLOAT Floating Offshore Wind Substructure'. In: *AIAA SCITECH 2022 Forum*, p. 2295.

DNV (2013). *DNV-RP-C202 Buckling Strength of Shells*.

— (2015). *DNVGL-RP-C104 Self-elevating units*.

DNV GL (2015). *SESAM release note, SIMA*.

— (2017). 'Recommended practice DNVGL-RP-C205 environmental conditions and environmental loads'. In: *Høvik: DNV GL AS*.

DNV GL AS (2016). 'Loads and site conditions for wind turbines.' In: *DNVGL-ST-0437*.

Dr.techn. Olav Olsen AS (2021). URL: http://www.olavolsen.no/ (visited on 20th Sept. 2021).

Ekberg, A. (2009). '7 - Fatigue of railway wheels'. In: *Wheel–Rail Interface Handbook*. Ed. by R. Lewis and U. Olofsson. Woodhead Publishing, pp. 211–244. ISBN: 978-1-84569-412-8. DOI: https://doi.org/10.1533/9781845696788.1.211. URL: https://www.sciencedirect.com/science/article/pii/B9781845694128500070.

Energy, U.S. Department of (2022). *How Do Wind Turbines Survive Severe Storms?* URL: https://www.energy.gov/eere/articles/how-do-wind-turbines-survive-severe-storms (visited on 24th Feb. 2022).

Equinor (2022a). *Hywind Demo*. URL: https://www.equinor.com/no/what-we-do/floating-wind/hywind-demo.html (visited on 15th Apr. 2022).

— (2022b). *Industrialiserer flytende havvind*. URL: https://www.equinor.com/no/what-we-do/floating-wind.html (visited on 15th Apr. 2022).

Faltinsen, O. (1990). *Sea Loads on Ships and Offshore Structures*. Cambridge University Press.

Finegan, Ioana C. and Ronald F. Gibson (1999). 'Recent research on enhancement of damping in polymer composites'. In: *Composite structures* 44.2-3, pp. 89–98. ISSN: 0263-8223.

Gaertner, Evan et al. (2020). *Definition of the IEA 15-Megawatt Offshore Reference Wind*. URL: https://www.nrel.gov/docs/fy20osti/75698.pdf (visited on 2nd Feb. 2022).

Gallagher (2022). URL: https://gallaghercorp.com/polyurethane-vibration-damping-isolation/ (visited on 22nd Feb. 2022).

Gao, Zhen (16th Feb. 2022). Email to Maiten Kase Corona.

Germanischer Lloyd (2012). *Guideline for the Certification of Offshore Wind Turbines*.

Glaskin, Max (2015). *The science behind spokes*. URL: https://www.cyclist.co.uk/in-depth/85/the-science-behind-spokes (visited on 7th Feb. 2022).

Godvik, Marte (2016). 'Influence of wind coherence on the response of a floating wind turbine.' In: *Science Meets Industry; 2016; Stavanger, Norway:1–12.* URL: http://www.norcowe.no/doc//konferanser/2016/SMI%20Stavanger%20presentasjoner/Godvik.

Goudreau, Gerald Lee and Robert L Taylor (1973). 'Evaluation of numerical integration methods in elastodynamics'. In: *Computer Methods in Applied Mechanics and Engineering* 1.1, pp. 69–97.

Hansen, Martin (2015). *Aerodynamics of wind turbines*. Routledge.

Hansen, Martin Otto Laver et al. (2006). 'State of the art in wind turbine aerodynamics and aeroelasticity'. In: *Progress in aerospace sciences* 42.4, pp. 285–330.

He, Jimin (2001). *Modal analysis*. eng. Oxford.

Hobbs, Roger E. and Mohammed Raoof (1996). 'Behaviour of cables under dynamic or repeated loading'. In: *Journal of Constructional Steel Research* 39.1, pp. 31–50.

Hsu, Weiting et al. (June 2014). 'Snap Loads on Mooring Lines of a Floating Offshore Wind Turbine Structure'. In: *Proceedings of the International Conference on Offshore Mechanics and Arctic Engineering - OMAE* 9. DOI: 10.1115/OMAE2014-23587.

Huera-Huarte, Francisco (Oct. 2013). 'Deep Water: The next step for offshore wind energy. A report by the European Wind Energy Association'. In.

IEA (2019). *Offshore Wind Outlook 2019*. Paris. URL: https://www.iea.org/reports/offshore-wind-outlook-2019.

International Electrotechnical Commission, (IEC) (2005). 'Wind Turbines: Part 1: Design Requirements.' In: *IEC, Geneva, Switzerland: IEC61400-1:2005*.

— (2009). 'Wind Turbines: Part 3: Design Requirements for offshore wind turbines.' In: *IEC61400-3*.

International Energy Agency (2006). *World Energy Outlook 2006*.

Jansen, Jeffrey (2015). *Understanding Creep Failure of Plastics: Continuous stress over long periods leads to creep rupture*. Wisconsin, USA. URL: plasticsengineering.org.

Jingyoung (2021). *What is a guy wire and how to use it? – The Ultimate Guide (2021)*. URL: https://www.hbjinyong.com/guy-wire-definition/. (accessed: 16.11.2021).

Johnson, Erik A., Richard E. Christenson and Billie F. Spencer Jr. (2003). 'Semiactive Damping of Cables with Sag'. eng. In: *Computer-aided civil and infrastructure engineering* 18.2, pp. 132–146. ISSN: 1093-9687.

Jonkman, B.J. (2016). 'TurbSim User's Guide v2.00.00'. In: *National Renewable Energy Laboratory*.

Joseph, Ajo, Arunraj K.S. and Savin Viswanathan (2014). 'Second Order Wave Force Effects on a Semi-Submersible Platform'. In: *Journal Impact Factor* 5.3, pp. 08–22.

Kelley, ND (2011). 'Turbulence-turbine interaction: The basis for the development of the TurbSim stochastic simulator'. In: *Contract* 303, pp. 275–300.

Krieger, A et al. (2015). *Deliverable D7. 2 design basis: LIFES50+*.

Kvittem, Marit Irene (2014). *Modelling and response analysis for fatigue design of a semi-submersible wind turbine*. eng. Trondheim.

Laino, David and A Craig Hansen (2004). 'Current efforts toward improved aerodynamic modeling using the aerodyn subroutines'. In: *42nd AIAA Aerospace Sciences Meeting and Exhibit*, p. 826.

Langen, Ivar (1974). *Numerisk tidsintegrasjon i dynamisk responsberegning*. nob. Trondheim.

Langen, Ivar and Ragnar Sigbjörnsson (1979). *Dynamisk analyse av konstruksjoner: Dynamic analysis of structures*. Tapir.

Larsen, Carl M. et al. (2019). *TMR 4182 Marine dynamics*.

Lawson, Vernon R. (1988). 'Problems and detection of line anchor and substation ground grid corrosion'. In: *IEEE transactions on industry applications* 24.1, pp. 25–32.

Li, Liang et al. (2019). 'Dynamic and structural performances of offshore floating wind turbines in turbulent wind flow'. eng. In: *Ocean engineering* 179, pp. 92–103. ISSN: 0029-8018.

Lopez-Pavon, Carlos and Antonio Souto-Iglesias (2015). 'Hydrodynamic coefficients and pressure loads on heave plates for semi-submersible floating offshore wind turbines: A comparative analysis using large scale models'. In: *Renewable Energy* 81, pp. 864–881.

Macquart, Terence, Alireza Maheri and Krishna Busawon (2012). 'Improvement of the accuracy of the blade element momentum theory method in wind turbine aerodynamics analysis'. In: *2012 2nd International Symposium On Environment Friendly Energies And Applications*. IEEE, pp. 402–405.

Manwell, James F., Jon G. McGowan and Anthony L. Rogers (2010). *Wind Energy Explained: Theory, Design and Application*. eng. 2. Aufl. New York: Wiley. ISBN: 9780470015001.

MARINTEK (2012). *SIMO User Manual Version 4.0 rev 0.* Trondheim, Norway.

— (2013). *RIFLEX User Manual Version 4.0 rev. 3*. Norwegian Marine Tachnology Research Institute, Trondheim, Norway.

midas Civil (2015). *Eigenvalue Analysis Control*. URL: http://manual.midasuser.com/EN_Common/Civil/895/Start/06_Analysis/Eigenvalue_Analysis_Control.htm. (accessed: 23.01.2022).

Mínguez, J M and J Vogwell (2008). 'An analytical model to study the radial stiffness and spoke load distribution in a modern racing bicycle wheel'. In: *Proceedings of the Institution of Mechanical Engineers.* 222.4, pp. 563–576. ISSN: 0954-4062.

Moan, Torgeir (2004). *Design of Offshore Structures*.

Moriarty, P.J. and A.C. Hansen (2005). *AeroDyn theory manual. Tech. Rep. NREL/TP-500-36881*.

Müller, Kolja, Frank Lemmer and Wei Yu (2017). 'Qualification of innovative floating substructures for 10MW wind turbines and water depths greater than 50m'. In: URL: https://lifes50plus.eu/wp-content/uploads/2018/04/GA_640741_LIFES50_D4.2.pdf.

Naess, Arvid and Torgeir Moan (2013). *Stochastic dynamics of marine structures*. Cambridge University Press.

Natarajan, Anand, Morten Hartvig Hansen and Shaofeng Wang (2016). 'Design Load Basis for Offshore Wind Turbines: DTU Wind Energy Report No. E-0133'. In.

NREL (2019). *Deep-Water Wind System Gains Further Momentum with ARPA-E ATLANTIS Funding*. URL: https://www.nrel.gov/news/program/2019/spiderfloat-innovation.html (visited on 2nd Feb. 2022).

Nybø, Astrid et al. (2020). 'Evaluation of different wind fields for the investigation of the dynamic response of offshore wind turbines'. eng. In: *Wind energy (Chichester, England)* 23.9, pp. 1810–1830. ISSN: 1095-4244.

OrcaFlex (2021). *Rayleigh damping: Guidance*. URL: https://www.orcina.com/webhelp/OrcaFlex/Content/html/Rayleighdamping,Guidance.htm (visited on 10th Dec. 2021).

Orecca (2022). URL: https://orecca.rse-web.it/map.phtml (visited on 15th Apr. 2022).

Park, Jin Tack and Nak-Sam Choi (2004). 'Flexural vibration analysis of a sandwich beam specimen with a partially inserted viscoelastic layer'. In: *KSME international journal* 18.3, pp. 347–356.

Patel, Minoo H. (2013). *Dynamics of offshore structures*. eng. London.

Pegalajar-Jurado, Antonio et al. (2018). *State-of-the-art model for the LIFES50 OO-Star Wind Floater Semi 10MW floating wind turbine*. DOI: 10.1088/1742-6596/1104/1/012024. URL: https://doi.org/10.1088/1742-6596/1104/1/012024.

Pellegrino, Sergio and Christopher Reuben Calladine (1986). 'Matrix analysis of statically and kinematically indeterminate frameworks'. In: *International Journal of Solids and Structures* 22.4, pp. 409–428.

Puthanpurayil, Arun M., Rajesh P. Dhakal and Athol J. Carr (2011). 'Modelling of In-Structure Damping: A Review of the State-of-the-art'. In: *Proc. Ninth Pacific Conf. Earthquake Engineering,[Online]. Paper*. 091.

Ramachandran, GKV et al. (2017). 'Design basis for the feasibility evaluation of four different floater designs'. In: *Energy Procedia* 137, pp. 186–195.

Reis Tagliari, Mariana dos et al. (2019). 'Tensile armor wires submitted to slow strain rate tests in a corrosive environment and cathodic protection: A comparison between two different microstructures'. eng ; por. In: *Materials research (São Carlos, São Paulo, Brazil)* 22.3, p. 1. ISSN: 1516-1439.

Renewables Consulting Group (2021). *Global Offshore Wind Snapshot 2020*.

Roddier, D. et al. (2011). *A generic 5 MW WindFloat for numerical tool validation & comparison against a generic spar*. Rotterdam, The Netherlands.

Roddier, Dominique (2011). 'A generic 5 MW WindFloat for numerical tool validation & comparison against a generic spar'. In: *OMAE2011-50278*.

Schepers, J.G. (2007). *IEA Annex XX: Dynamic Inflow effects at fast pitching steps on a wind turbine placed in the NASA-Ames wind tunnel*. Petten: ECN.

Silva de Souza, Carlos Eduardo et al. (2021). 'Definition of the INO WINDMOOR 12 MW base case floating wind turbine'. In.

SINTEF Ocean (2021). *RIFLEX Theory Manual*.

Skelton, Robert E. and Mauricio C. de Oliveira (2009). *Tensegrity Systems*. University of California, San Diego 9500 Gilman Drive La Jolla, CA 92093-0411 USA.

Snel, H. and J. G. Schepers (Apr. 1995). *Joint investigation of dynamic inflow effects and implementation of an engineering method*.

Stephens, Ralph I et al. (2000). *Metal fatigue in engineering*. John Wiley & Sons.

Stockhouse, David et al. (2021). 'Control of a Floating Wind Turbine on a Novel Actuated Platform'. eng. In.

Suh, Jeong-In and Sung Pil Chang (2000). 'Experimental study on fatigue behaviour of wire ropes'. In: *International Journal of Fatigue* 22.4, pp. 339–347.

Tao, L et al. (2007). 'Spacing effects on hydrodynamics of heave plates on offshore structures'. eng. In: *Journal of fluids and structures* 23.8, pp. 1119–1136. ISSN: 0889-9746.

Tao, Longbin and Shunqing Cai (2004). 'Heave motion suppression of a Spar with a heave plate'. eng. In: *Ocean engineering* 31.5, pp. 669–692. ISSN: 0029-8018.

Tao, Longbin and Krish Thiagarajan (2003). 'Low KC flow regimes of oscillating sharp edges I. Vortex shedding observation'. eng. In: *Applied ocean research* 25.1, pp. 21–35.

Technology, Bergen Cable (2021). URL: https://www.frasersdirectory.com/redwire/avoid-wire-rope-bending-fatigue-1441723996734// (visited on 3rd Oct. 2021).

Tetteh, Edem Y et al. (2022). 'Active Ballasting Actuation for the SpiderFLOAT Offshore Wind Turbine Platform'. In: *AIAA SCITECH 2022 Forum*, p. 2161.

University of Massachusetts Amherst (2022). *Early Offshore Wind Research*. URL: http://www.umass.edu/windenergy/about.history.earlyresearch.php (visited on 15th Apr. 2022).

University of Rochester (2022). *Real Eigenvalue Analysis*. URL: http://www2.me.rochester.edu/courses/ME443/NASTRAN/Chpt3RealEigenvalueAnalysis.pdf (visited on 8th Feb. 2022).

Whittier, William Brooks (2002). 'Kinematic analysis of tensegrity structures'. PhD thesis. Virginia Tech.

Xue, Wenfei (2016). 'Design, numerical modelling and analysis of a spar floater supporting the DTU 10MW wind turbine'. MA thesis. NTNU.

Yamaguchi, H. and Y. Fujino (1998). 'Stayed cable dynamics and its vibration control'. In: *Bridge Aerodynamics*.

Yu, W., K. Müller and F. Lemmer (2018). *Deliverable D4.2 Public Definition of the Two LIFES50+ 10MW Floater Concepts, in Qualification of innovative floating substructures for 10MW wind turbines and water depths greater than 50m*.

Appendix

A Tower Properties

Table A1: LIFES50+ OO-Star 10 MW distributed tower properties (elevations given w.r.t. 11 m above MSL) (Müller et al. 2017)

Section	**Lower elevation** [m]	**Upper elevation** [m]	**Outer diameter**[1] [m]	**Thickness** [m]	**Mass** [t]
1	0.000	3.946	11.385	0.075	86.67
2	3.946	7.892	11.154	0.074	83.78
3	7.892	11.838	10.923	0.072	79.83
4	11.838	15.785	10.692	0.070	75.98
5	15.785	19.731	10.462	0.068	7.222
6	19.731	23.677	10.231	0.066	68.55
7	23.677	27.623	10.000	0.065	65.99
8	27.623	31.569	9.769	0.063	62.48
9	31.569	35.515	9.538	0.061	59.08
10	35.515	39.462	9.308	0.059	55.76
11	39.462	43.408	9.077	0.057	52.54
12	43.408	47.354	8.846	0.056	50.30
13	47.354	51.300	8.615	0.054	47.24
14	51.300	55.246	8.385	0.052	44.28
15	55.246	59.192	8.154	0.050	41.40
16	59.192	63.138	7.923	0.048	38.63
17	63.138	67.085	7.692	0.047	36.72
18	67.085	71.031	7.462	0.045	34.10
19	71.031	74.977	7.231	0.043	31.58
20	74.977	78.923	7.000	0.041	29.16
21	78.923	82.869	6.769	0.039	26.82
22	82.869	86.815	6.538	0.038	25.24
23	86.815	90.762	6.308	0.036	23.07
24	90.762	94.708	6.077	0.034	20.99
25	94.708	98.654	5.846	0.032	19.01
26	98.654	102.600	5.615	0.030	17.12
27	102.600	104.630	5.165	0.028	8.104

[1]Values provided at section centre

Table A2: LIFES50+ OO-Star 10 MW geometric tower parameters (Müller et al. 2017)

Parameter	**Value**
Tower base elevation above MSL [m]	11.0
Tower-top elevation above MSL [m]	115.63
Total mass [kg]	1.256E+06
Inertia about x, y-axis w.r.t. tower centre of mass [kg·m^2]	9.6225E+08
Density [kg/m^3]	8242.5
Young's modulus [N/m^2]	2.1E+11
Shear modulus of elasticity [N/m^2]	8.08E+10

B RNA Properties

Table B1: RNA mass properties of the DTU 10 MW reference wind turbine (Yu et al. 2018)

Parameter	**Value**
Rotor mass [kg]	230 183
Rotor centre of mass [m, m, m]	[-7.07, 0, 119]
Nacelle mass [kg]	444 536
Nacelle centre of mass [m, m, m]	[2.69, 0, 118.08]
Nacelle, rotor and hub vertical centre of mass [m]	118.39
Combined tower top masses [kg]	674 719
Roll moment of inertia of tower top masses[2] around tower top [kg·m^2]	1.659E+08
Pitch moment of inertia of tower top masses around tower top [kg·m^2]	1.062E+08
Yaw moment of inertia of tower top masses around tower top [kg·m^2]	1.014E+08

[2]Combined nacelle, rotor and hub masses

C Example TurbSim Input File

```
---------TurbSim v2.00.* Input File------------------------
for user-defined time series input
---------Runtime Options-----------------------------------
False         Echo            - Echo input data to <RootName>.ech (flag)
100           RandSeed1       - First random seed  (-2147483648 to
2147483647)
1100          RandSeed2       - Second random seed (-2147483648 to
2147483647) for intrinsic pRNG, or an alternative pRNG: "RanLux" or
"RNSNLW"
False         WrBHHTP         - Output hub-height turbulence parameters in
binary form?  (Generates RootName.bin)
False         WrFHHTP         - Output hub-height turbulence parameters in
formatted form?  (Generates RootName.dat)
False         WrADHH          - Output hub-height time-series data in
AeroDyn form?  (Generates RootName.hh)
False         WrADFF          - Output full-field time-series data in
TurbSim/AeroDyn form? (Generates Rootname.bts)
True          WrBLFF          - Output full-field time-series data in
BLADED/AeroDyn form?  (Generates RootName.wnd)
False         WrADTWR         - Output tower time-series data? (Generates
RootName.twr)
False         WrFMTFF         - Output full-field time-series data in
formatted (readable) form?  (Generates RootName.u, RootName.v, RootName.w)
False         WrACT           - Output coherent turbulence time steps in
AeroDyn form? (Generates RootName.cts)
True          Clockwise       - Clockwise rotation looking downwind? (used
only for full-field binary files - not necessary for AeroDyn)
 0            ScaleIEC        - Scale IEC turbulence models to exact
target standard deviation? [0=no additional scaling; 1=use hub scale
uniformly; 2=use individual scales]

--------Turbine/Model Specifications-----------------------
32             NumGrid_Z       - Vertical grid-point matrix dimension
32             NumGrid_Y       - Horizontal grid-point matrix dimension
0.05           TimeStep        - Time step [seconds]
4000           AnalysisTime    - Length of analysis time series [seconds]
(program will add time if necessary: AnalysisTime = MAX(AnalysisTime,
UsableTime+GridWidth/MeanHHWS) )
4000           UsableTime      - Usable length of output time series
[seconds] (program will add GridWidth/MeanHHWS seconds unless UsableTime
is "ALL")
119            HubHt           - Hub height [m] (should be >
0.5*GridHeight)
228            GridHeight      - Grid height [m]
228            GridWidth       - Grid width [m] (should be >=
2*(RotorRadius+ShaftLength))
0              VFlowAng        - Vertical mean flow (uptilt) angle
[degrees]
0              HFlowAng        - Horizontal mean flow (skew) angle
[degrees]

--------Meteorological Boundary Conditions-------------------
"IECKAI"      TurbModel       - Turbulence model
("IECKAI","IECVKM","GP_LLJ","NWTCUP","SMOOTH","WF_UPW","WF_07D","WF_14D","
TIDAL","API","USRINP","TIMESR", or "NONE")
"unused"      UserFile        - Name of the file that contains inputs for
user-defined spectra or time series inputs (used only for "USRINP" and
"TIMESR" models)
"3"           IECstandard     - Number of IEC 61400-x standard (x=1,2, or
3 with optional 61400-1 edition number (i.e. "1-Ed2") )
"B"           IECturbc        - IEC turbulence characteristic ("A", "B",
"C" or the turbulence intensity in percent) ("KHTEST" option with NWTCUP
model, not used for other models).
"NTM"         IEC_WindType    - IEC turbulence type ("NTM"=normal,
```

```
"xETM"=extreme turbulence, "xEWM1"=extreme 1-year wind, "xEWM50"=extreme
50-year wind, where x=wind turbine class 1, 2, or 3)
"default"     ETMc            - IEC Extreme Turbulence Model "c" parameter
[m/s]. Only used when IEC_WindType=xETM.
"PL"          WindProfileType - Velocity profile type ("LOG";"PL"=power
law;"JET";"H2L"=Log law for TIDAL model;"API";"USR";"TS";"IEC"=PL on rotor
disk, LOG elsewhere; or "default")
"unused"      ProfileFile     - Name of the file that contains input
profiles for WindProfileType="USR" and/or TurbModel="USRVKM" [-]
119.00        RefHt           - Height of the reference velocity (URef)
[m]
"11.4"        URef            - Mean (total) velocity at the reference
height [m/s] (or "default" for JET velocity profile) [must be 1-hr mean
for API model; otherwise is the mean over AnalysisTime seconds]
"350"         ZJetMax         - Jet height [m] (used only for JET velocity
profile, valid 70-490 m)
0.14          PLExp           - Power law exponent [-] (or "default"). 0
if no shear.
0.0003        Z0              - Surface roughness length [m] (or
"default")

--------Non-IEC Meteorological Boundary Conditions------------
"default"     Latitude        - Site latitude [degrees] (or "default")
  0.05        RICH_NO         - Gradient Richardson number [-]
"default"     UStar           - Friction or shear velocity [m/s] (or
"default")
"default"     ZI              - Mixing layer depth [m] (or "default")
"default"     PC_UW           - Hub mean u'w' Reynolds stress [m^2/s^2]
(or "default" or "none")
"default"     PC_UV           - Hub mean u'v' Reynolds stress [m^2/s^2]
(or "default" or "none")
"default"     PC_VW           - Hub mean v'w' Reynolds stress [m^2/s^2]
(or "default" or "none")

--------Spatial Coherence Parameters----------------------------
"IEC"         SCMod1          - u-component coherence model
("GENERAL","IEC","API","NONE", or "default")
"IEC"         SCMod2          - v-component coherence model
("GENERAL","IEC","NONE", or "default")
"IEC"         SCMod3          - w-component coherence model
("GENERAL","IEC","NONE", or "default")
"default"     InCDec1         - u-component coherence parameters for
general or IEC models [-, m^-1] (e.g. "10.0  0.3e-3" in quotes) (or
"default")
"default"     InCDec2         - v-component coherence parameters for
general or IEC models [-, m^-1] (e.g. "10.0  0.3e-3" in quotes) (or
"default")
"default"     InCDec3         - w-component coherence parameters for
general or IEC models [-, m^-1] (e.g. "10.0  0.3e-3" in quotes) (or
"default")
"default"     CohExp          - Coherence exponent for general model [-]
(or "default")

--------Coherent Turbulence Scaling Parameters------------------
".\EventData" CTEventPath     - Name of the path where event data files
are located
"random"      CTEventFile     - Type of event files ("LES", "DNS", or
"RANDOM")
true          Randomize       - Randomize the disturbance scale and
locations? (true/false)
1             DistScl         - Disturbance scale [-] (ratio of event
dataset height to rotor disk). (Ignored when Randomize = true.)
0.5           CTLy            - Fractional location of tower centerline
from right [-] (looking downwind) to left side of the dataset. (Ignored
```

```
when Randomize = true.)
0.5           CTLz            - Fractional location of hub height from the
bottom of the dataset. [-] (Ignored when Randomize = true.)
30.0          CTStartTime     - Minimum start time for coherent structures
in RootName.cts [seconds]

======================================================
! NOTE: Do not add or remove any lines in this file!
======================================================
```

D ULS Load Cases from the LIFES50+ Project

Table D1: Site conditions (Ramachandran et al. 2017)

Extreme Sea States (ESS)	50-year significant wave height, $H_{s50,3h}$ [m]	10.9
	50-year peak period range, $T_{p50,3hmin}$-$T_{p50,3hmax}$ [s]	9.0-16.0
Severe Sea States (SSS)	Significant wave height up to the rated wind speed [m]	7.7
	Significant wave height beyond the rated wind speed [m]	10.9
	Peak period range [s]	11.7-20

Table D2: Ultimate limit state DLCs (Ramachandran et al. 2017)

Name	**PSF**	**Description**	**U [m/s]**	**Yaw [deg]**	**Turb.**	**Seeds**	**Shear**	**Gust**	**SS**	**WWD**	**T [s]**
DLC16	1.35	Power prod. in SSS	4:2:26	-10/0/+10	NTM	2	0.14	None	SSS	UNI	3600
DLC61	1.35	Parked in extreme wind	v_{50yrs}	-10/+10	NTM	2	0.11	None	ESS	UNI	3600

E Schematic Representation of the Tensegrity System

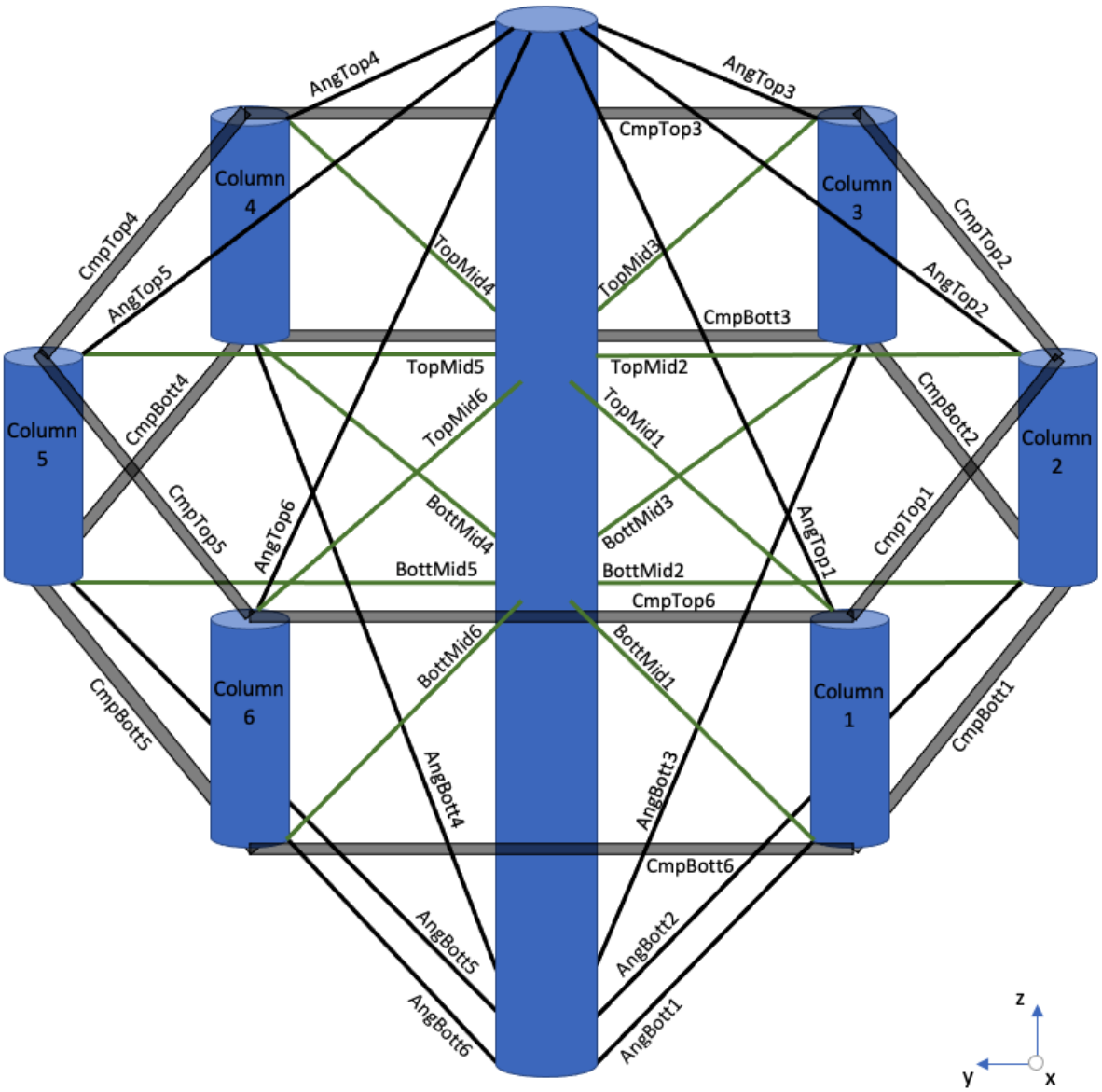

Figure E1: Schematic representation of the sections in the tensegrity system (dimensions are not to scale)

F Node Scheme of the Tensegrity System

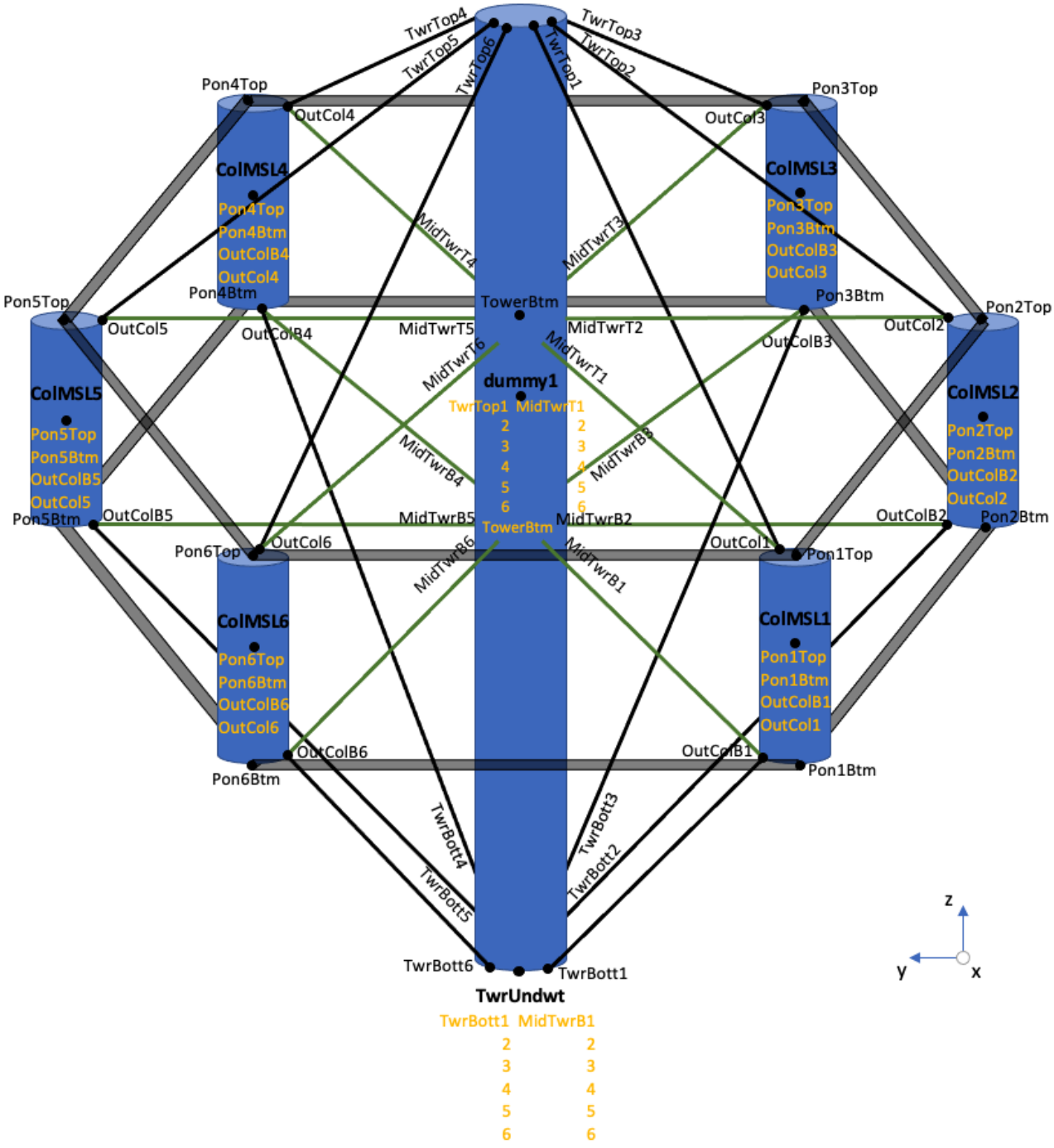

Figure F1: Schematic representation of the nodes in the tensegrity system (dimensions are not to scale). The node names in bold text are the master nodes, and the node names colored yellow are their slave nodes.

Master's thesis 2022

Maiten Kase Corona

NTNU
Kunnskap for en bedre verden